



Università  
degli Studi di  
Messina

DIPARTIMENTO DI SCIENZE BIOMEDICHE,  
ODONTOIATRICHE E DELLE IMMAGINI  
MORFOLOGICHE E FUNZIONALI

# UNIVERSITÀ DEGLI STUDI DI MESSINA

DIPARTIMENTO DI BIOMORF

DOTTORATO DI RICERCA IN BIOINGEGNERIA APPLICATA ALLE SCIENZE  
MEDICHE

CICLO XXXV

## **Smart Design of customized hip prostheses in additive manufacturing using numerical and experimental methodologies combined with the use of a markerless motion capture algorithm and a parametric multibody system of a human subject**

**Dario Milone**

*Supervisore:*

**Ch.mo Prof. Ing. Giacomo Risitano ING-IND 14**

**Ch.mo Prof. Ing. Francesco Longo ING -INF 05**

*Coordinatore del corso:*

**Ch.mo Prof. Michele Gaeta**

---

# INDEX

Summary.....	i
PART I Theoretical Background.....	iv
1. Biomechanics Overview.....	1
1.1. Application of Biomechanics.....	1
1.1. Computational Modeling.....	2
1.2. Rigid Body Models.....	4
1.2.1. coordinates description in spatial multibody system.....	10
1.2.2. Position, velocities, and accelerations.....	16
1.2.3. Equation of Motion for constrained systems.....	17
1.3. Finite Element Method.....	19
1.3.1. Static Analysis.....	25
1.3.2. Dynamic Analysis.....	26
1.3.3. Implicit and explicit method.....	27
1.3.4. Discretization method, Meshing.....	28
2. Additive manufacturing.....	30
2.1. A review of the additive manufacturing.....	30
2.2. SLM/SLS and their key process variables.....	32
2.3. Comparison between Additive Manufacturing and traditional method in prosthetics field	35
2.4. SLM lattice structures: overview.....	36

## Summary

3.	Human Anatomy Terminology and Pose Detection Method .....	40
3.1.	Terminology and Human standards .....	40
3.2.	Anthropometry .....	44
3.3.	Human joint.....	47
3.4.	Gait analysis .....	48
3.5.	Human pose estimation .....	51
3.6.	Body segment models .....	55
PART II Experimental activities .....		59
4.	Workflow.....	60
4.1.	First step – Motion Capture.....	62
4.2.	Second step – Gait analysis and angle extrapolation .....	65
4.3.	Third step – Human multi-body system.....	68
4.3.1.	Mannequins dialog boxes .....	69
4.3.2.	Type and orientation of Joint .....	72
4.3.3.	Body dimension selection.....	74
4.3.4.	Inertial parameters .....	81
4.3.5.	Multibody simulation output.....	83
4.4.	Fourth step – Fem Analysis .....	86
4.4.1.	Pre-processing – Loads and Constraints .....	86
4.4.2.	Pre-processing – Material selection.....	88
4.5.	Fifth step - Optimization Process.....	91

*Summary*

5. CONCLUDING REMARKS .....98

References .....100

List of publications .....127

---

## **SUMMARY**

The present PhD thesis is the collection of three years of research activity in the biomechanical field. The thesis aimed to achieve a Smart Design method that allows the customization of hip prostheses by the knowledge of human dynamics.

This procedure is a closed loop algorithm where the main activity evaluated human handling by the motion capture Markerless. After the dynamic acquisition, the algorithm optimizes the shape of the prosthesis based on the loads acting on the hip.

Motion Capture was applied to define the humans kinematic. A real-time multi-person human pose detection library that detects the human body was used to acquire the human pose.

Multibody analysis was carried out to define what were the load acting on the hip during the motion. A parametric model of the human subject was created to evaluate the different load conditions

Finite element simulations were carried out to apply the shape optimization and then the Lattice optimization as approach to customize the prosthesis.

Several research perspectives have been opened by this thesis, that the author would pursue in the future. The thesis is divided into two parts. Technical notions in the biomechanical field characterize the first part. Topics underlying multibody and fem systems are covered, as well as 3d printing technologies and their applications in the medical field. Finally, the medical terminology used for defining the joints of the human body, the references taken into consideration and the current systems for capturing the pose of a subject are described. On the contrary, the second part of the document presents the activity carried out in the three years of the doctorate, focusing on the steps followed for creating the smart algorithm for optimizing the hip prosthesis. At the end of the thesis a list of publication by the author is presented.

The chapter structure is as follow:

## ***Part One – Theoretical background***

Chapter 1- Biomechanics Overview: this chapter describes the field of biomechanics, giving an overview of the sector. Computational modelling is then briefly described. The final part of the chapter is characterized by the definition of the rules governing multi-body modelling and the fem.

Chapter 2- Additive Manufacturing: in this chapter, the field of additive manufacturing is described. First, we overview the sector and then focus on SLM / SLS techniques. A comparison is then made between traditional and additive manufacturing in the field of prostheses then to define the field of latex structures with SLM techniques.

Chapter 3- Human Anatomy Terminology and Pose Detection Method: This chapter describes the basic terminology governing the field of biomechanics, focusing on the nomenclature of the principal biomechanical planes and the reference systems. This chapter also deals with the field of Anthropometry. The ways to model a human body are then described, thus defining how to schematize the joints and joints that connect them. Finally, the history of multi-segment modelling of the human body is defined.

## ***Part Two– Experimental activities***

The second part of the document describes the scientific activity conducted during the three years. The whole procedure is contained in chapter 4. This chapter initially describes the procedure adopted, giving space to the definition of the steps to follow to complete it. Once the workflow is defined, all the steps are described in detail. The first step described is motion capture. This paragraph defines the neural network model used, the procedure is schematized, and finally, the outputs of this system are defined. The second part of the procedure that is described is the extraction of the joint angles. In this paragraph, the equations are defined to create the time histories representing each joint's angular variation perceived by the motion capture system. In the next paragraph, the realized multibody model and the parameters governing it are first described. The end of this paragraph reports the outputs from the multibody model; an analysis is also made on the walk, ultimately defining the amount of energy consumed during the walk. The definition of the FEM model characterizes the last two paragraphs, the loads and constraints acting on the system, the material chosen for the prosthesis, and finally, the optimization techniques used to optimize the hip prosthesis are defined. In the first phase, the shape optimization performed is described, giving importance to

the parameters that describe the geometry in question, the optimization algorithm, and the results obtained from the following analysis. The second part describes the topological optimizer based on latex structures.

**PART I**  
**THEORETICAL BACKGROUND**

# 1. BIOMECHANICS OVERVIEW

## 1.1. Application of Biomechanics

*“Biomechanics is the study of the mechanical aspects of the structure and function of biological systems”*[1]

The biomechanics field aims to solve biomedical or biological problems by using mechanical engineering methods, techniques and theories [1–2]. Engineering methods range from experimental to numerical approaches. The first one [3] observes changes in biological tissues (e.g. bone, muscle, cartilage and ligament) or structures (e.g. knee) under normal and abnormal conditions. Experimental studies could be performed *in vivo*, *ex vivo* or *in vitro* conditions. *In vivo* experimentation relates to studying whole living subjects in a natural environment. *Ex vivo* or *in vitro* experimentations deal with the testing of tissues isolated outside the biological surroundings of the living organism. Such experimentations are commonly performed in a culture environment. It is important to note that the characteristics and behaviors of a biological tissue/structure *in vivo* condition are entirely different from those of the same tissue/structure *in vitro* or *ex vivo* conditions. Moreover, *in silico* numerical studies [4–6] aim to model and simulate living systems to provide unobservable information of the tissue or structure under investigation, such as bone stress under body loading or muscle force during motion. Numerical studies test the impact of a clinical treatment procedure (surgery or functional rehabilitation) or an implanted device (e.g., prosthesis or orthotic) on the living tissues or structures. Finally, a biomechanics study is performed in response to a fundamental

research question or to depict its potential application for a specific case (e.g., clinical case and industrial case), as illustrated in Figure 1. Moreover, a biomechanics study relates to a single-scale object of study (i.e. cell and molecule, tissue and organ, system, or individual or population) or multi-scale object of study[7].

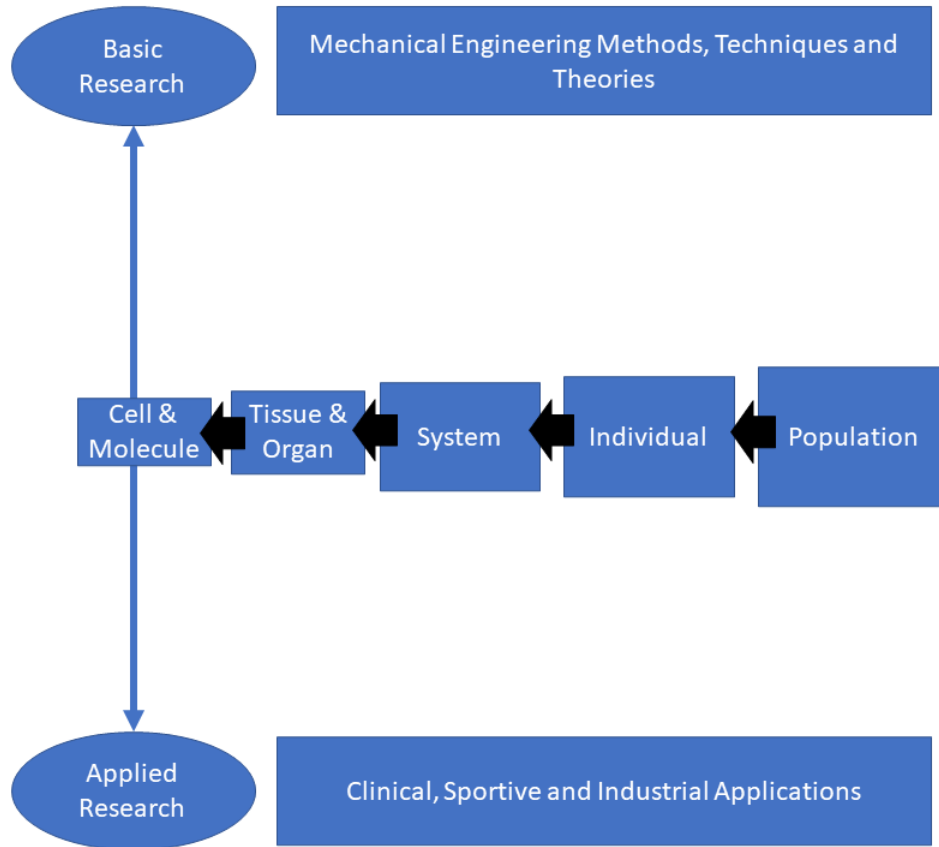


Figure 1: Overview of biomechanics field of study [7].

## 1.1. Computational Modeling

*“Computational modeling is the use of computers to simulate and study complex systems using mathematics, physics, and computer science. A computational model contains numerous variables that characterize the system being studied. Simulation is done by adjusting the variables alone or in combination and observing the outcomes. Computer modeling allows scientists to conduct thousands of simulated experiments by computer. The thousands of computer experiments identify the handful of laboratory experiments that are most likely to solve the problem being studied.”*[8]

Computational modelling represents mathematical modelling based on a computer simulation. It requires computational resources to study the mechanism underlying a complex system. The experimenter usually performs computational modelling in conjunction with experimental studies, which are used to provide the input conditions and validate the output measurements. The combined approach is beneficial and powerful for complex investigation of biological problem.

Computational modelling applied to the musculoskeletal system mainly includes [9–10]:

- 1) Multibody dynamics analysis of motion
- 2) Loading at the skeleton scale,
- 3) Solid mechanics analysis of stresses and strains at the tissue level using the finite element method.
- 4) Computational fluid dynamics (CFD) to investigate the fluid ingress in the joint space.

Experimentation in the laboratory requires a waste of time and high costs. For this reason, it has been preferred to use computational modelling alongside experimental tests to reduce time and costs in recent years. This approach allows for parametric screening analysis, optimization, and design indications for further experimentation. It is essential to ensure that the numerical method is accurate, which generally requires verification and validation. Interpreting the results is also fundamental for fully understanding the physical problem. Verification represents the implementation of a model that conceptually defines the solution of the mathematical model. At the same time, the predictions are compared by the validation process with the experimental specifications [11]:

- 1) Verification: "solving the equations correctly"
- 2) Validation: "solving the correct equations"

In [12], there are procedures suggestion directory to be followed during simulation testing, which includes lists of models used and their modifications, all the simulation procedures to be applied and in what order, the processing of the raw numerical results and the description of the final output.[13] outlined the general considerations for reporting finite element modelling studies in biomechanics, including parameters for model identification, model structure,

simulation structure, verifications, validation and availability. A recent update on knee joint modelling was provided by [14].

From the simulation point of view, two methods exist for developing biomedical problems. The first approach refers to the rigid multi-body dynamics to describe the cinematic and dynamic behaviour of the human subject. The second approach concerns deformable modelling using the properties of fabrics and finite element methods for the study the interaction of the structure also considering the fluids, under normal and abnormal load conditions (Figure 2)

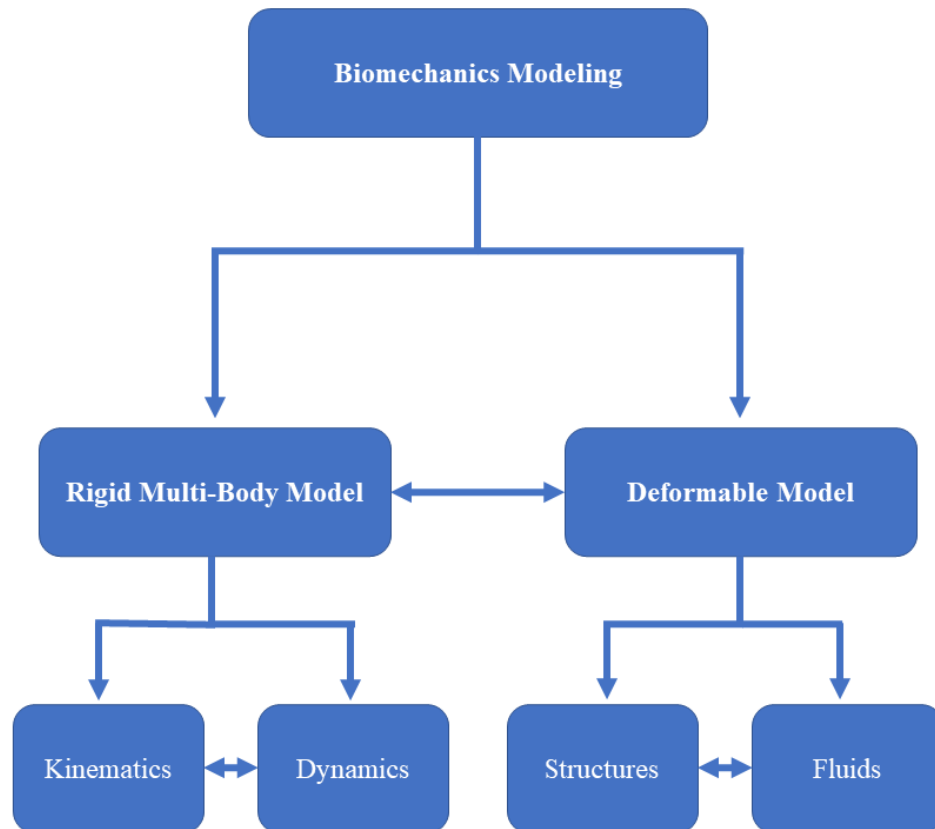


Figure 2: Biomechanical models and their interactions.

## 1.2. Rigid Body Models

*“Rigid-body dynamics studies the movement of systems of interconnected bodies under the action of external forces. The assumption that the bodies are rigid, i.e. they do not deform*

under the action of applied forces, simplifies the analysis by reducing the parameters that describe the system's configuration to the translation and rotation of reference frames attached to each body.”[15–16]

It is possible to distinguish Multibody systems (MBS) based on two main characteristics:

- 1) Mechanical components describing large dimensions translational and rotational displacements.
- 2) Kinematic joints that impose them constraints or restrictions on the relative motion of bodies.

The multibody system includes a set of rigid and/or flexible bodies interconnected by kinematic joints and some force elements [17]. Figure 3 shows an abstract representation of a multibody system[18].

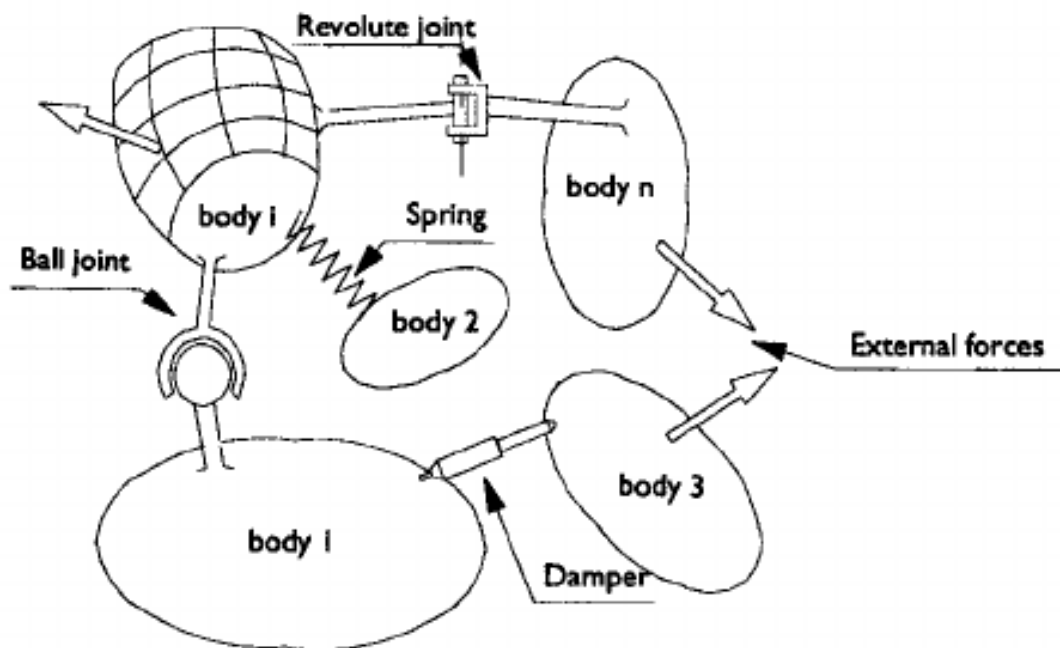


Figure 3: Schematic representation of a multibody system [19].

Within a multi-body system, they stand out as Rigid or flexible bodies. A body is said to be rigid when its deformations are small in such a way as not to form the global movement produced by the body, it can translate and rotate, but it cannot change. On the contrary, a flexible body has an elastic structure; all the points belonging to it are not linked to a mutual distance between them. In spatial space, the motion of a free rigid body can completely utilize the six generalized coordinates associated with the six degrees of freedom. When a body

includes some flexibility, it has six rigid degrees of freedom plus the number of generalized coordinates needed to describe the deformations [20]. The term flexible multibody system refers to a system that contains deformable bodies with internal dynamics. The representation of a rigid body is only an approximate convention since there are no infinitely rigid bodies. However, in many typical applications, the bodies are remarkably rigid; hence, their flexibility can be neglected, and the bodies can be considered perfectly rigid. Forces applied to multibody system components can result from springs, shock absorbers, actuators, or external forces. Externally applied forces of different natures can act on a multibody system to simulate the interactions between the components of the system and between them and the surrounding environment.[21–22]. Multibody systems are widely used in engineering and research activities, such as robotics[23], automotive vehicles[24], biomechanics [25], mechanisms [26], railway vehicles [27].

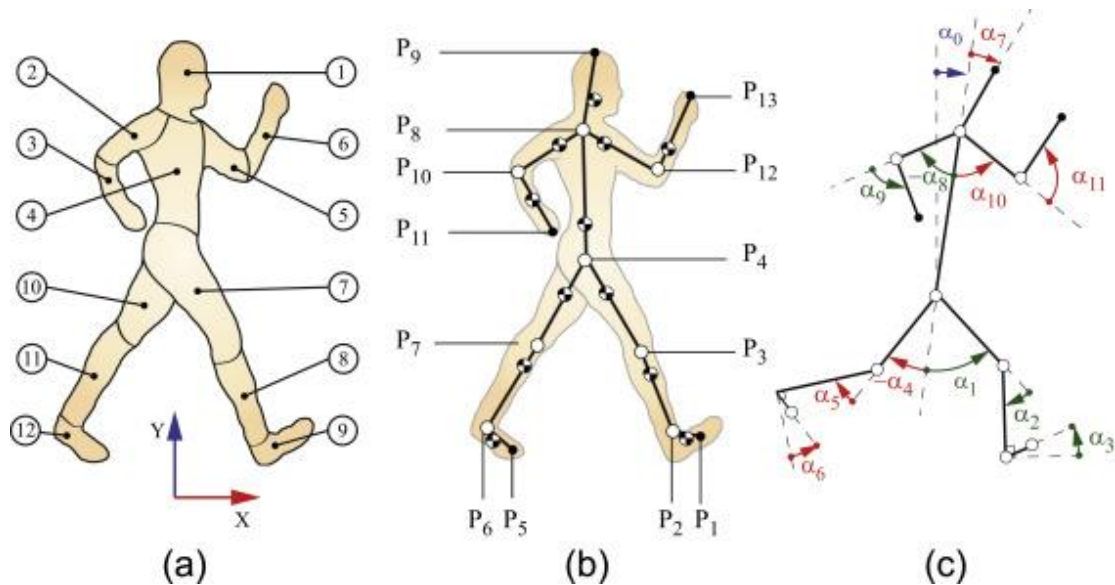


Figure 4: Examples of application of multibody systems human biomechanical model [28]

The variables that describe (generalized coordinates) the dynamics of multibody systems must characterize, at any instant of time:

- 1) the system's configuration is the position of all the material points that make up the bodies.
- 2) must uniquely define the location of system components in an instant while analysing the multibody system.

Linear and angular coordinates are included in the generalized coordinate expression [29]. The mobility of a system, i.e., the minimum number of variables needed to describe the configuration fully of a system is called the system's degrees of freedom (DoF) [30]. The number of degrees of freedom can be defined as the number of independent generalized coordinates needed to describe the unique configuration of a system. In the spatial case, each body has six degrees of freedom. By introducing a joint into the system, the total number of DoFs is reduced by the number of constraints imposed by the joint. The number of degrees of freedom can be evaluated as the difference between the system coordinates and the number of independent constraints [31]. The mathematical expression that summarizes this idea in the plane is known as Grüebler's formula:

$$n = 3(m - 1) - 2c_1 - c_2 \tag{1}$$

This criterion can be extended to kinematic chains in space with the use of the Kutzbach's formula:

$$n = 6(m - 1) - 5c_1 - 4c_2 - 3c_3 - 2c_4 - c_5 \quad (2)$$

where  $c_x$  represents the class of the kinematic pair, where x is the degrees of freedom left free by the pair. finally, it can be noted that:

- 1)  $n < 0$  iperstatic system.
- 2)  $n = 0$  isostatic system.
- 3)  $n > 0$  labile system.

Generalized coordinates are divided into two groups (Figure 5) [32]:

- 1) Independent coordinates: vary arbitrarily.
- 2) Dependent coordinates: necessary to satisfy the dependent equations

Another distinction must be made when the dependent coordinates are described:

- 1) Absolute coordinates [33].
- 2) Relative coordinates [34].
- 3) Natural coordinates [35].

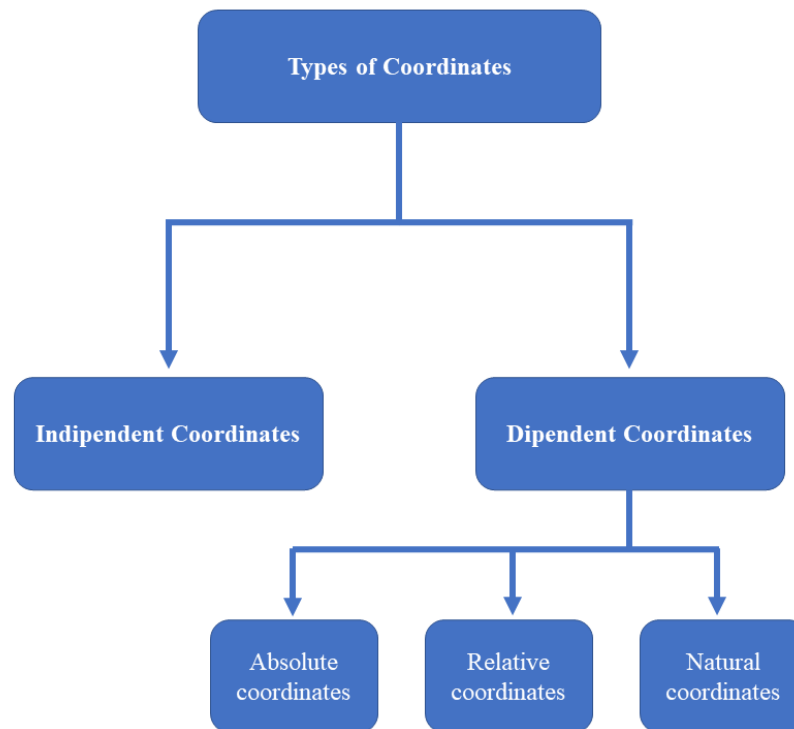


Figure 5: Types of coordinates used for multibody systems formulation.

The methodologies of multibody systems include the two main phases:

- 1) Development of mathematical models of multibody systems.
- 2) Implementing computational procedures to perform the simulation, analysis and optimization of the global motion produced.

Modelling or formulation is the process of generating and assembling the equations of motion necessary for solving the behaviour of a multibody system. Two modelling approaches can be considered [17]:

- 1) The formulation of the coordinates of the point: point-like coordinates represent joints and constraints represent bodies.
- 2) The formulation of the coordinates of the body: the coordinates represent the bodies and the constraint the joints.

Mechanical systems analysis can be performed statically or dynamically. In the first case, stationary systems are studied, invariant over time. In the second case, the systems are in motion and time dependent. Furthermore, the branch of dynamics can be divided into two main disciplines, namely, kinematics and kinetics. In kinematic analysis, the geometric aspects of

motion are considered independently of the forces that produce the motion. More precisely, kinematics deals with the study of displacement, velocity, and acceleration. In turn, kinetics studies movement characteristics and the relationship with moving forces. Unlike the case of static and kinematic analysis, where only algebraic equations are used, in kinetic analysis, the motion of a mechanical system is described by differential equations.

It is widespread to refer to kinetic analysis as dynamic analysis because kinetic analysis must also be based on knowledge of the kinematic analysis of a system. Two different types of analysis can be performed in the study of the dynamics of a mechanical system, direct dynamics, and inverse dynamics. In direct dynamic analysis, the external forces acting on the bodies of a system are known, and the resulting motion is obtained by solving the equations of motion. On the other hand, in inverse dynamic analysis, a specific movement is sought for a multibody system, and the goal is to determine the forces required to produce that movement[22].

### **1.2.1. coordinates description in spatial multibody system**

Multibody systems' configuration and motion properties are characterized by quantities such as displacements, velocities and accelerations[36]. A proper system of coordinates must be adopted, including the global and local coordinates systems. The global coordinate system is represented by three orthogonal axes that are rigidly connected at a point called the origin(xyz) of the system and represent the global inertial frame. The local coordinate system is related to the center of gravity of the bodies and is indicated with  $\xi\eta\zeta$ , it moves and rotates mutually with the body. The particle “i” moving in three-dimensional space can be located by a position vector “r” contains three scalar values (3).

$$r_i = \{x_i \ y_i \ z_i\}^T \quad (3)$$

Thanks to its definition, even a rigid body can be described through an arbitrary point belonging to it[35]. Any reference system can be used to describe the position and orientation of a body. For this reason, the coordinates describing a multibody system can be expressed or concerning each other or to a municipality reference framework.

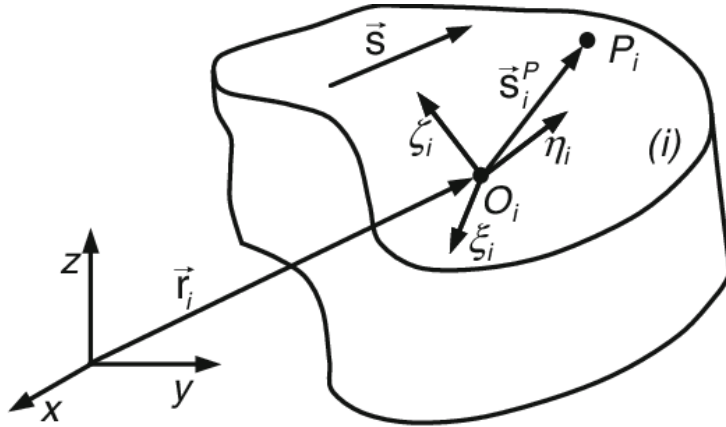


Figure 6: Location of an unconstrained body “i” in the three-dimensional space [37]

The body-fixed coordinate system is referred to as  $\xi_i\eta_i\zeta_i$ . The vector  $r$ , expressed in Eq. (3), defines the location of the originate the local coordinate system. This vector represents the translational coordinates of the body. Another set of coordinates is needed to express the orientation of the body with respect to the global coordinate system. The point  $P_i$  located on the body “i” in Figure 6 can be defined from the origin of the local reference frame by the vector  $s_i^P$ , so that its direct location concerning the global system can be expressed as [38]:

$$r_i^p = r_i + s_i^p \quad (4)$$

The same point can be described with respect to the local coordinates system by  $s_i'^p$ , that contains the local components of vector  $s_i^p$ . there is a relationship between  $s_i^p$  and  $s_i'^p$ :

$$s_i^p = A_i s_i'^p \quad (5)$$

The matrix  $A_i$  is a  $3 \times 3$  rotation matrix that can be used to describe the orientation of local coordinate system referring to the global frame. As in Eq. (6)  $P_i$  can be written in local and global coordinates.

$$s_i^p = \begin{Bmatrix} x_i^p \\ y_i^p \\ z_i^p \end{Bmatrix} \text{ and } s_i'^p = \begin{Bmatrix} \xi_i^p \\ \eta_i^p \\ \zeta_i^p \end{Bmatrix} \quad (6)$$

Matrix  $A_i$  can be expressed in terms of cosines as

$$A_i = \begin{bmatrix} a_{11} & a_{12} & a_{13} \\ a_{21} & a_{22} & a_{23} \\ a_{31} & a_{32} & a_{33} \end{bmatrix} \quad (7)$$

Where the columns contain three-unit vector  $u_{\xi i}, u_{\eta i}, u_{\zeta i}$  projected into xyz.

$$u_{\xi i} = \begin{Bmatrix} a_{11} \\ a_{21} \\ a_{31} \end{Bmatrix} \quad u_{\eta i} = \begin{Bmatrix} a_{12} \\ a_{22} \\ a_{32} \end{Bmatrix} \quad u_{\zeta i} = \begin{Bmatrix} a_{13} \\ a_{23} \\ a_{33} \end{Bmatrix} \quad (8)$$

It should be noted that

$$u'_{\xi i} = \begin{Bmatrix} 1 \\ 0 \\ 0 \end{Bmatrix} \quad u'_{\eta i} = \begin{Bmatrix} 0 \\ 1 \\ 0 \end{Bmatrix} \quad u'_{\zeta i} = \begin{Bmatrix} 0 \\ 0 \\ 1 \end{Bmatrix} \quad (9)$$

A rigid body "i" in three-dimensional space can be defined by three translation coordinates and three rotation coordinates that describe it in position and orientation to a fixed triad  $\xi_i, \eta_i, \zeta_i$  attached to the body concerning the global frame XYZ, as shown in Figure 7.

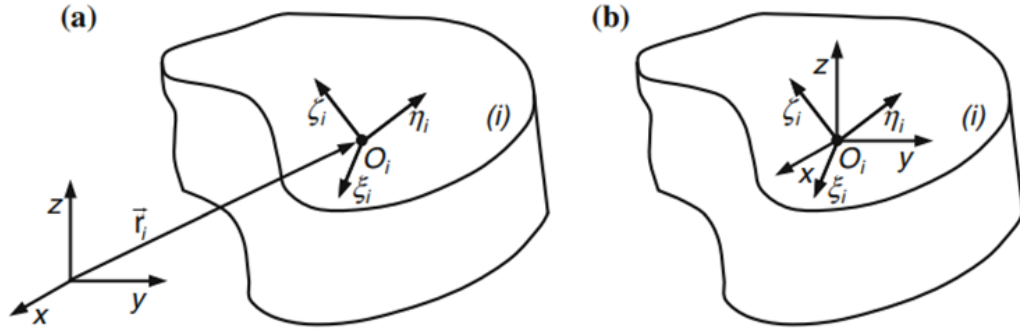


Figure 7: translation coordinates and rotation coordinates[37].

With the use of transformation matrices, it is possible to express the orientation and position of this body since the elements that make up this matrix are expressed in terms of appropriate sets of coordinates, such as Euler angles, Bryant angles or Euler parameters. Since the body's movement is continuous, the transformation matrix must be a continuous function of time. The cosines of nine directions present in the rotational transformation matrix  $A_i$  expressed in Eq. (7) define the orientation of the axes  $\xi_i\eta_i\zeta_i$ . Only three direction cosines are independent, six constraints must be considered to determine matrix  $A_i$ . Euler angles represent three composed rotations that move a reference frame to a given referred frame. For this reason, any orientation can be obtained by composing three rotations around a single axis so that any rotation can be decomposed as the product of three elementary rotation matrices. Thus, the angular orientation of a given fixed coordinate system on the body can be imagined as the result of three successive rotations. The angles  $\psi$ ,  $\theta$  and  $\sigma$ , which are the Euler angles, completely specify the orientation of the  $\xi\eta\zeta$  coordinate system relative to the  $xyz$  frame and can, therefore, act as a set of three independent coordinates[39–40]. By using Euler angles, the matrix  $A$  can be obtained as a product of the matrices that defines the planar rotations[41].

$$B = \begin{bmatrix} c\psi & -s\psi & 0 \\ s\psi & c\psi & 0 \\ 0 & 0 & 1 \end{bmatrix}, C = \begin{bmatrix} 1 & 0 & 0 \\ 0 & c\vartheta & -s\vartheta \\ 0 & s\vartheta & c\vartheta \end{bmatrix}, D = \begin{bmatrix} c\sigma & -s\sigma & 0 \\ s\sigma & c\sigma & 0 \\ 0 & 0 & 1 \end{bmatrix} \quad (10)$$

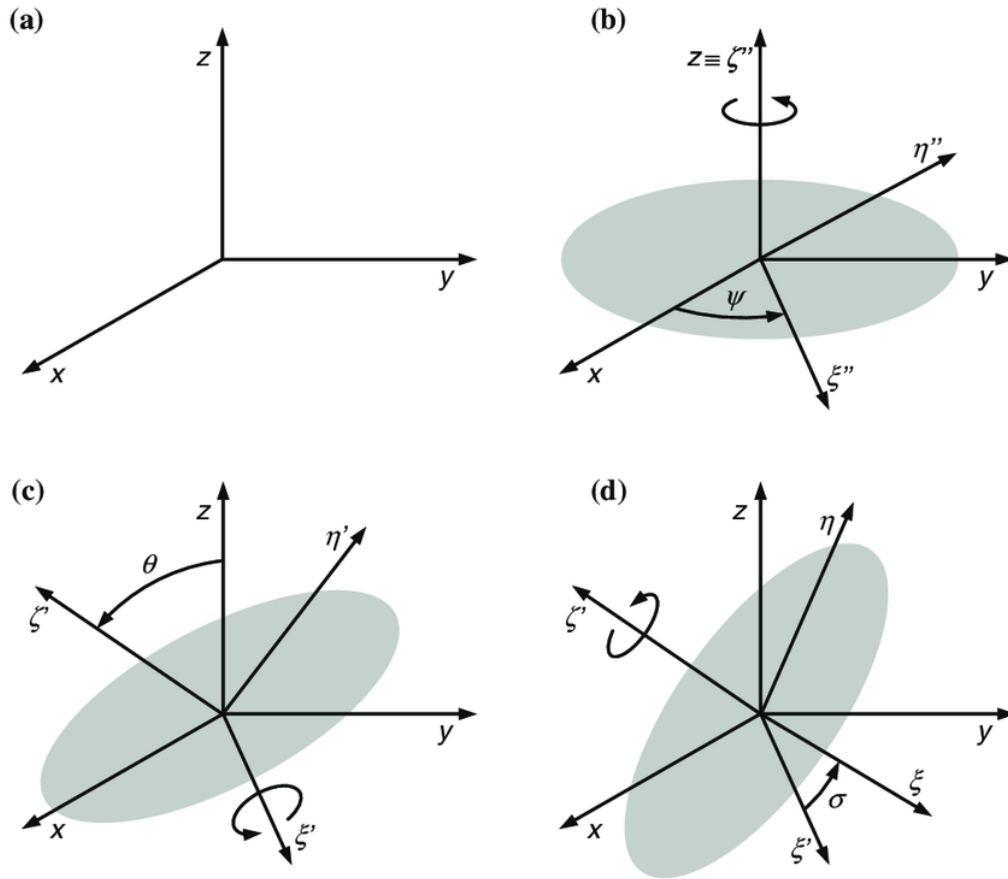


Figure 8: *ifferent stages of rotation for Euler angles. a Initial global system coordinate; b First rotation; c Second rotation; d Third rotation*[42].

It can be written that  $A=BCD$

$$A = \begin{bmatrix} c\psi c\sigma - s\psi c\theta s\sigma & -c\psi s\theta - s\psi c\theta c\sigma & s\psi s\theta \\ s\psi c\sigma + c\psi c\theta s\sigma & -s\psi s\theta - c\psi c\theta c\sigma & -c\psi s\theta \\ s\theta s\sigma & s\theta c\sigma & c\theta \end{bmatrix} \quad (11)$$

The resulting matrix is nonlinear. when  $\sin \theta = 0$ , the axes of the first and third rotations coincide, so that  $\psi$  and  $\sigma$  cannot be distinguished. According to Euler's theorem on finite rotation, a rotation in three-dimensional space can always be described by a rotation along a specific axis on a certain angle. Euler's theorem states that the general displacement of a body with a fixed point is a rotation around an axis. The theorem indicates that it is possible to obtain the orientation of the axes fixed to the body at any time by an imaginary rotation of these axes from an orientation coincident with the global axes. So, according to Euler's

theorem, there is a single axis that if frame XYZ is rotated around it by an angle  $\phi$  becomes parallel to frame  $\xi\eta\zeta$  or vice versa. This imaginary axis is denoted by  $\vec{u}$  and is called the orientated axis of rotation, as shown in Figure 9.

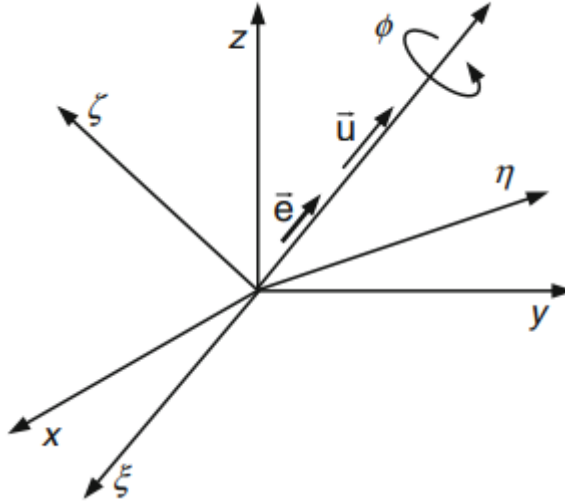


Figure 9: Representation of the Euler parameter[43]

Hence, a set of rotation coordinates can be defined as (12). The four quantities  $e_0$ ,  $e_1$ ,  $e_2$  and  $e_3$  are the so-called Euler parameters, and it can be observed that these angles are not independent.

$$e_0 = \cos \frac{\phi}{2} \tag{12}$$

$$e = \{e_1 \quad e_2 \quad e_3\}^T = \text{u sin} \frac{\phi}{2} \tag{13}$$

$$e_0^2 + e^t e = e_0^2 + e_1^2 + e_2^2 + e_3^2 = 1 \tag{14}$$

$$p = \begin{Bmatrix} e_0 \\ e \end{Bmatrix} = \begin{Bmatrix} e_0 \\ e_1 \\ e_2 \\ e_3 \end{Bmatrix} \quad p^T p = 1 \tag{15}$$

The transformation matrix can be expressed in term of Euler parameters.

$$A = \begin{bmatrix} e_0^2 + e_1^2 - \frac{1}{2} & e_1e_2 - e_0e_3 & e_1e_3 + e_0e_2 \\ e_1e_2 + e_0e_3 & e_0^2 + e_2^2 - \frac{1}{2} & e_1e_2 - e_0e_3 \\ e_1e_3 - e_0e_2 & e_1e_2 - e_0e_3 & e_0^2 + e_3^2 - \frac{1}{2} \end{bmatrix} \quad (16)$$

### 1.2.2. Position, velocities, and accelerations

Six coordinates uniquely define the configuration of a body free in the space, whereas three coordinates are needed to specify the body's position and the other three coordinates are required to describe its angular orientation [21]. The position of a body “i” can be defined as

$$q_0 = \begin{Bmatrix} r_i \\ p_i \end{Bmatrix} \quad (17)$$

$$r = \begin{Bmatrix} x_i \\ y_i \\ z_i \end{Bmatrix} \quad (18)$$

$$p_i = \begin{Bmatrix} e_0 \\ e_1 \\ e_2 \\ e_3 \end{Bmatrix} \quad (19)$$

Velocity vector specifying the translational and rotational velocity of a body i are defined as[44]

$$v_i = \begin{Bmatrix} \dot{r}_i \\ \dot{\omega}_i \end{Bmatrix} \quad (20)$$

$$\bar{\omega}_i = \begin{Bmatrix} \bar{\omega}_x \\ \bar{\omega}_y \\ \bar{\omega}_z \end{Bmatrix} \quad (21)$$

acceleration vector specifying the translational and rotational accelerations of a body  $i$  is defined as

$$\dot{v}_i = \begin{Bmatrix} \ddot{r}_i \\ \ddot{\bar{\omega}}_i \end{Bmatrix} \quad (22)$$

### 1.2.3. Equation of Motion for constrained systems

The translational equations of motion for an unconstrained rigid body can be expressed [45] as

$$m\ddot{r} = f \quad (23)$$

$m$  represents the mass of the body,  $\ddot{r}$  denotes the acceleration of the center of mass and  $f$  represents the sum of all forces acting on the body [46]. Nikravesh in [22] demonstrated that the rotational equations of motion for a rigid body can be written in the form.

$$J\dot{\omega} + \tilde{\omega}J\omega = n \quad (24)$$

where  $J$  is the global inertia tensor,  $\omega$  denotes the global angular accelerations,  $x$  is global angular velocities and  $n$  represents the sum of all moments acting on the body.

$$\begin{bmatrix} mI & 0 \\ 0 & J \end{bmatrix} \begin{Bmatrix} \ddot{r} \\ \dot{\omega} \end{Bmatrix} + \begin{Bmatrix} 0 \\ \dot{\omega} \end{Bmatrix} = \begin{Bmatrix} f \\ n - \tilde{\omega}J\omega \end{Bmatrix} \quad (25)$$

The Newton-Euler equations of motion of a multibody system composed by  $nb$  unconstrained bodies are written as

$$M\dot{v} = g \quad (26)$$

Where:

$$M = \begin{bmatrix} M_1 & & \\ & \ddots & \\ & & M_{n_b} \end{bmatrix}, \dot{v} = \begin{Bmatrix} \dot{v}_1 \\ \dot{v}_2 \\ \vdots \\ \dot{v}_{n_b} \end{Bmatrix}, g = \begin{Bmatrix} g_1 \\ g_2 \\ \vdots \\ g_{n_b} \end{Bmatrix} \quad (27)$$

for a multibody system of constrained bodies, the Newton-Euler equations of motion are written as

$$M\dot{v} = g + g^{(c)} \quad (28)$$

$$g^{(c)} = D^T \lambda \quad (29)$$

where  $g^{(c)}$  denotes the vector of reaction forces that can be expressed in terms of the Jacobian matrix and Lagrange multipliers as in [22],[44]. Finally, the dynamic equations of motion for a constrained multibody system can be written in its general form as

$$M\dot{v} - D^T \lambda = g \quad (30)$$

the second time derivative of the constraint equations are considered here and written as

$$D\ddot{v} = \gamma \quad (31)$$

This system of equations is solved for accelerations vector,  $\ddot{v}$ , and Lagrange multipliers,  $\lambda$ . Then, in each integration time step, the accelerations vector,  $\ddot{v}$ , together with velocities vector,  $\dot{v}$ , is integrated to obtain the system velocities and positions for the next time step. A set of initial conditions, positions and velocities, is required to start the dynamic simulation. All the equations can be written in matrix form as [47]

$$\begin{bmatrix} M & D^T \\ D & 0 \end{bmatrix} \begin{Bmatrix} \ddot{v} \\ \lambda \end{Bmatrix} = \begin{Bmatrix} g \\ \gamma \end{Bmatrix} \quad (32)$$

The procedure can be summarized as

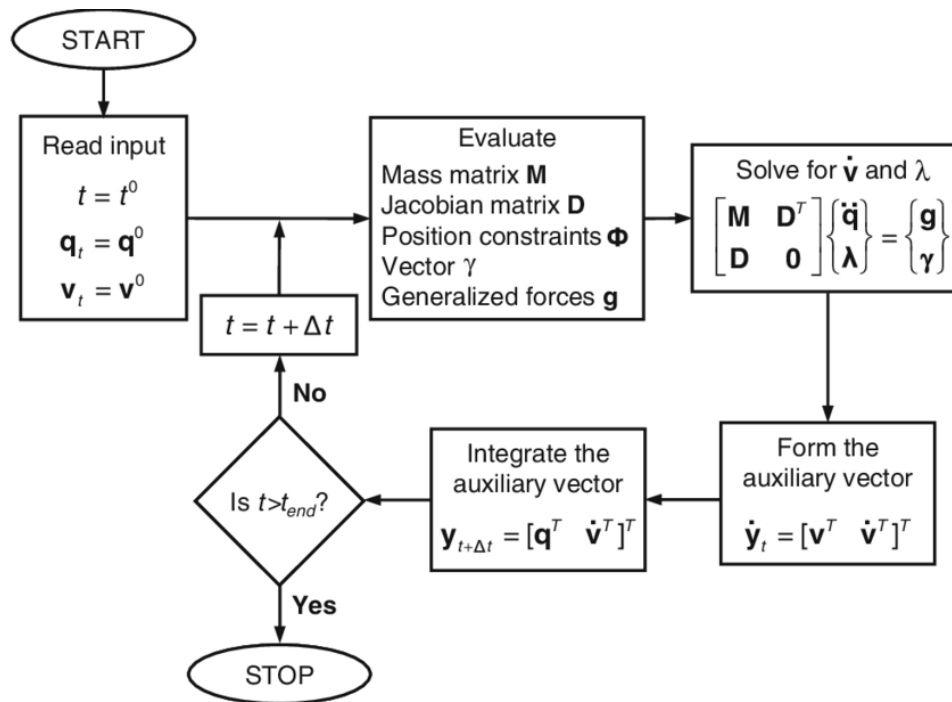


Figure 10: Flowchart of computational procedure for dynamic analysis of multibody systems based on the standard Lagrange multipliers method [48]

### 1.3. Finite Element Method

*“FEM is a numerical method to solve partial differential equations in two or three spatial variables. This approach divides an extensive system into smaller and simpler parts called finite elements; this is achieved by discretizing the space by building a mesh of the object. Finally, the formulation of the finite element method of a boundary problem results in a system of algebraic equations. The method approximates an unknown function of the domain”*[49]

The finite element method arises from the need to solve complex elasticity and structural analysis problems in civil and aeronautical engineering. Its development dates to the work of A. Hrennikoff [50] and R. Courant [51]. Various pioneers have formulated this method in different ways [51–55], all united by the discretization of the mesh of a continuous domain into a set of discrete subdomains, usually called elements. A rigorous mathematical basis for the finite element method was provided in 1973 with the publication of Strang and Fix. [54]The method has since been generalized for numerical modelling of physical systems in various engineering disciplines, such as electromagnetism, heat transfer, and fluid dynamics. [56]

The discretization of a system has several advantages, such as:

- 1) Accurate representation of complex geometries.
- 2) Inclusion of dissimilar material properties.
- 3) Representation of the total solution.
- 4) The capture of local effects.

dividing the problem domain into a collection of subdomains, with each subdomain represented by a set of equations of elements to the original problem systematically recombining all the sets of equations of the elements into a global system of equations for the final calculation. The global system of equations has known solution techniques and can be calculated from the initial values of the original problem to obtain a numerical answer. In the first step above, the element equations are simple equations that locally approximate the original complex equations to be studied, whereas the original equations are often partial differential equations. The finite element method is commonly introduced as a particular case of the Galerkin method[57]. The process, in mathematical language, consists in constructing an integral of the internal product of the residual and the weight functions and zeroing the integral; this is a procedure that minimizes the approximation error by adapting the proof functions in the PDE. The residual is the error caused by the test functions, and the weight functions are polynomial approximation functions that project the residual. The process removes all spatial derivatives from the PDE, thus approximating the PDE locally with:

- 1) a set of algebraic equations for steady-state problems.
- 2) a set of ordinary differential equations for transient problems.

The sets of algebraic equations that arise in steady-state problems are solved using numerical methods of linear algebra, while the sets of ordinary differential equations that arise in transient problems are solved by numerical integration using standard techniques such as Euler's method or the method of Runge-Kutta[58]. A global system of equations is generated from the equations of the elements through a coordinates transformation from the local nodes of the subdomains to the domain's global nodes. This spatial transformation includes appropriate orientation adjustments applied concerning the reference coordinate system. The process is often performed by the FEM software using the coordinate data generated by the subdomains.

The practical application of FEM is known as finite element analysis (FEA). FEA applied in engineering is a computational tool for performing engineering analyzes. It includes the use of mesh generation techniques to divide a complex problem into small elements, as well as the use of software coded with a FEM algorithm. In the application of FEA, the complex problem is usually a physical system with underlying physics such as the Euler-Bernoulli beam equation, the heat equation or the Navier-Stokes equations expressed in PDE or integral equations. In contrast, the small, divided elements of complex problems represent different areas of the physical system. FEA can analyze problems in complicated domains, when the domain changes, when the desired precision varies across the entire domain, or when the solution lacks softness.[59] Under the hypothesis of material with linear elastic behaviour, homogeneous and isotropic, and subjected to infinitesimal deformations, the system of 15 equations in 15 unknowns admits one and only one solution.[60], [61]

$$\begin{cases} \frac{\partial \sigma_x}{\partial x} + \frac{\partial \tau_{xy}}{\partial y} + \frac{\partial \tau_{xz}}{\partial z} + F_x = 0 \\ \frac{\partial \sigma_y}{\partial y} + \frac{\partial \tau_{yx}}{\partial x} + \frac{\partial \tau_{yz}}{\partial z} + F_y = 0 \\ \frac{\partial \sigma_z}{\partial z} + \frac{\partial \tau_{zy}}{\partial y} + \frac{\partial \tau_{zx}}{\partial x} + F_z = 0 \end{cases} \quad (33)$$

$$\begin{cases} \varepsilon = \frac{\partial u_x}{\partial x} \\ \varepsilon = \frac{\partial u_y}{\partial y} \\ \varepsilon = \frac{\partial u_z}{\partial z} \\ \gamma_{xy} = \frac{\partial u_x}{\partial y} + \frac{\partial u_y}{\partial x} \\ \gamma_{xz} = \frac{\partial u_x}{\partial z} + \frac{\partial u_z}{\partial x} \\ \gamma_{yz} = \frac{\partial u_y}{\partial z} + \frac{\partial u_z}{\partial y} \end{cases} \quad (34)$$

$$\left\{ \begin{array}{l} \varepsilon_x = \frac{1}{E} [\sigma_x - \nu(\sigma_y + \sigma_z)] \\ \varepsilon_y = \frac{1}{E} [\sigma_y - \nu(\sigma_x + \sigma_z)] \\ \varepsilon_z = \frac{1}{E} [\sigma_z - \nu(\sigma_x + \sigma_y)] \\ \gamma_{xy} = \frac{\tau_{xy}}{G} \\ \gamma_{yx} = \frac{\tau_{xy}}{G} \\ \gamma_{xy} = \frac{\tau_{xy}}{G} \end{array} \right. \quad (35)$$

However, always remember that this is an engineering process; the problem is simplified to find a solution, which involves the inevitable addition of an error. It is not always possible to simplify the problem and then apply the FEM, as it is, in any case, a numerical technique designed to seek approximate solutions to problems described by partial differential equations by reducing the latter to a system of algebraic equations.

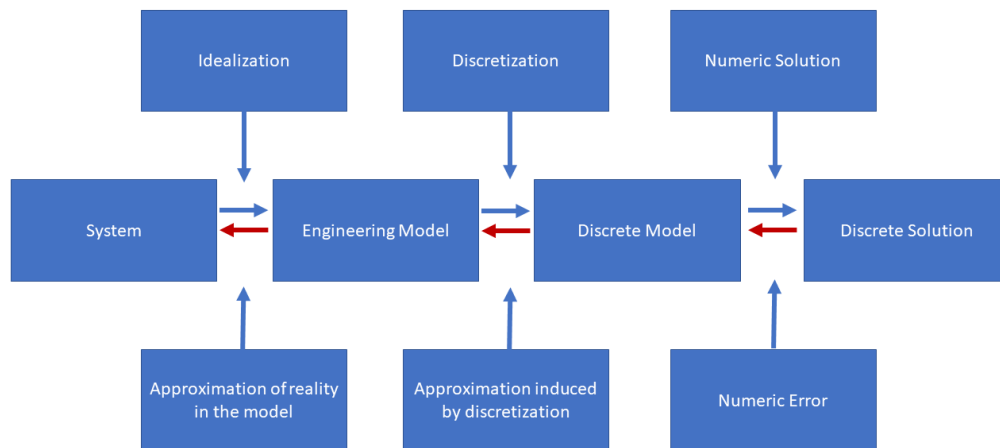


Figure 11: Error propagation during the process.

Among the most common analyzes in the mechanical field are the static and dynamic ones[62]. The static analysis studies static problems in the strict sense and almost static (the excitation frequency of the load applied to the structure is less than one-third of a minor natural frequency of the system). The effects of inertia are, however, neglected. Dynamic analysis

studies the time dependence of the problem and considers the presence of the system's inertia and damping forces. The problems are also very different from each other and can encompass Linear and nonlinear problems. In linear problems, the body is in the range of elasticity and subjected to small deformations. Generally, a system is linear if there is a law of proportionality between input and output. In nonlinear problems, this law of proportionality is not valid[63]. A linear problem (sometimes even a nonlinear one) can be solved using linear systems. In linear systems, a deformable solid body has a linear behaviour. The mathematical model describes a linear relationship between the imposed stress and the associated response. They enjoy the following properties:

$$F(aQ_1 + bQ_2) = aF(Q_1) + bF(Q_2) \quad (36)$$

$$\forall(a, b) \in \mathbb{R} \times \mathbb{R}; \forall(Q_1; Q_2) \quad (37)$$

The principle of superposition of effects states that the effect of applied stresses on any system is equal to the sum of each effect[64]. In particular:

$$a = b = 1 \text{ e } Q_1 = -Q_2 = Q \quad (38)$$

$$F = (Q_1 - Q_2) = 0 = F(Q_1) + F(-Q_2) \quad (39)$$

$$(Q_1) = -F(-Q_2) \quad (40)$$

The response of a linear system is entirely reversible but can only be applied if all the relationships between cause and effect are linear. In a nonlinear system (plasticity, large deformations), the superposition principle of the effects is not valid, and the system has irreversible behavior. The nonlinearity of the response of a deformable solid depends on the following factors.

- 1) Non-linearity of the mechanical behavior of the material (constitutive non-linearity)
- 2) Geometric non-linearity due to:
  - Transformations: the deformed configuration of the system differs significantly from the initial one.

- Non-linearity of the imposed load conditions.
- Non-linearity of kinematic constraints.

A nonlinear problem is generally linearized. It is divided into steps assuming the behaviors of each of these linear. The analysis restarts from the configuration reached in the previous step[65]. For the definition of a FEM analysis, a series of steps must be followed. The first is Assigning to the element a function of the form (a), a polynomial type of function that links the displacements of a generic point of the element \underline{f}^i with its nodal displacements f.

$$\underline{f}^i = \underline{\alpha} f \quad (41)$$

$\alpha$  indicates the vector of the coefficients of the polynomial, and with  $\phi$  the matrix of the coordinates, the shape function is obtained from the following steps:

$$\underline{\alpha} = \underline{\phi}^{-1}(x, y) f \quad (42)$$

The compatibility equations that link the deformations of a generic element point with the nodal displacements are then defined. They are defined continuously throughout the structure.

$$\underline{\varepsilon}^i = \underline{b} f^i = \underline{b} \underline{\alpha} f = \underline{B} f^i \quad (43)$$

$$\underline{\varepsilon}^i = \underline{b} f^i \quad (44)$$

Where  $b$  is a matrix in which some differential operators link the deformations of a generic point with its displacements. At this point, the constitutive equations for the element are defined:

$$\underline{\sigma}^i = \underline{D} \underline{\varepsilon}^i \quad (45)$$

The stiffness matrix of the element is constructed using the Principle of Virtual Works, in which the work caused by internal forces is equaled with the work caused by external forces

$$(\delta W = \delta U) \tag{46}$$

$$\underline{F}^t \underline{\delta f} \tag{47}$$

$$\int_V \underline{\underline{\sigma}}^T \underline{\underline{\delta \varepsilon}} dV \tag{48}$$

$$F \delta f = \int_V \underline{\underline{\sigma}}^T \underline{\underline{\delta \varepsilon}} dV = \int_V \underline{\underline{B}}^T \underline{\underline{DB}} dV \underline{f} \underline{\delta f} \tag{49}$$

$$\underline{\underline{K}} = \int_V \underline{\underline{B}}^T \underline{\underline{DB}} dV \underline{f} \underline{\delta f} \tag{50}$$

$$\underline{F}_j = \underline{\underline{K}}_j \underline{f}_j \xrightarrow{T} \underline{\overline{F}}^i = \underline{\underline{K}}^i \underline{f}^i \rightarrow \underline{F} = \underline{\underline{K}} \underline{f} \tag{51}$$

The stiffness matrix of the structure K is obtained from the single elements by summing the homologous terms that link the displacements of the common nodes with the forces acting on the nodes themselves. Moreover, the matrix K is symmetric and singular.[66]

$$\underline{f} = \underline{\underline{K}}^{-1} \underline{F} \rightarrow \underline{f}^i = \underline{a} \underline{f} \rightarrow \underline{\varepsilon}^i = \underline{b} \underline{f}^i \rightarrow \underline{\sigma}^i = \underline{\underline{D}} \underline{\varepsilon}^i \tag{52}$$

### 1.3.1. Static Analysis

Static analysis is divided into linear and non-linear. In the linear one, the solution is stable and independent of the choice of the time step. Therefore, it is independent of time. It can easily find inputs and outputs from the coefficient matrix that binds them.

$$\underline{F} = \underline{\underline{K}} \underline{f} \tag{53}$$

$$\underline{f} = \underline{F} \underline{\underline{K}}^{-1} \tag{54}$$

Non-linear analysis involving equations of a higher order than the first must consider many small-time intervals to achieve convergence and minimize errors. It is used to solve geometric problems (for example, buckling or buckling loads and problems due to contact) but also to problems depending on the material (plastic or elastoplastic). It is solved through knowledge of self-values of the matrix that links inputs and outputs, which returns a series of compatible solutions, or through the iterative method of Newton-Raphson[67].

$$(\underline{K} - \lambda \underline{K}_G) \underline{f} = 0 \quad (55)$$

### 1.3.2. Dynamic Analysis

Dynamic analysis involves systems in which there is a strong dependence on time and the presence of the system's inertia and damping forces. It is divided into the linear and non-linear dynamic analysis (crash). Linear dynamic analysis, in turn, can include:

- 1) Free vibrations, whose solution is found through the eigenvalue problem[67]

$$\underline{M} \ddot{\underline{f}} + \underline{K} \underline{f} = 0 \rightarrow [-\omega^2 \underline{M} + \underline{K}] \underline{f} = 0 \quad (56)$$

- 2) Forced vibrations, which can be solved through (57) [68]

$$\underline{M} \ddot{\underline{f}} + \underline{K} \underline{f} = 0 \rightarrow [-\omega^2 \underline{M} + \underline{K}] \underline{f} = 0 \quad (57)$$

- 3) Modal analysis in which one is the matrix of the eigenvectors in which each column represents a way of vibrating the system[68]

$$\ddot{\underline{f}} + \underline{U}^T \underline{C} \underline{U} \dot{\underline{f}} + \underline{\Delta} \underline{y} = \underline{U}^T \underline{F}(t) \quad (58)$$

$$\underline{U}^T \underline{C} \underline{U} \text{ diagonal matrix} \quad (59)$$

- 4) Frequency response conducted through experimental tests
- 5) Direct calculation methods, distinguishable in explicit and implicit methods.

### 1.3.3. Implicit and explicit method

The explicit method defines the time increase at the analysis's beginning and remains constant during the calculation. The explicit method is conditionally stable, so the integration step must be less than a critical step, calculated as the time required for a shock wave to cross the smallest element of the model.[69]

$$\Delta t \leq \Delta t^{crit} = \frac{2}{\omega_{max}} \quad (60)$$

Therefore, the total analysis time depends to a greater extent on the smallest size of the smallest finite element present in the model rather than on the number of degrees of freedom of the model itself. In crash problems, small integration steps are generally not a problem since the characteristic times of the affected phenomenon are minimal. In the implicit method, the time increase varies at each calculation step to satisfy an appropriate convergence criterion. The implicit method is conditionally unstable.

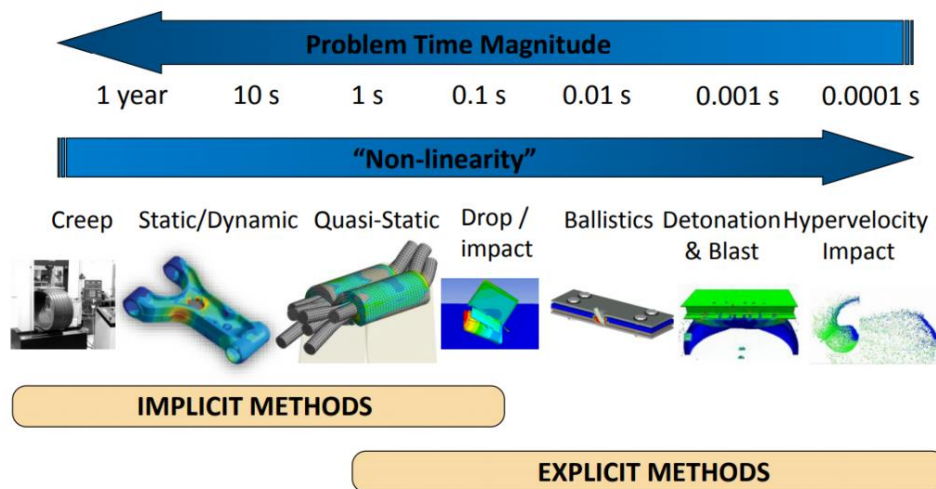


Figure 12: Comparison between the implicit and explicit method.

### **1.3.4. Discretization method, Meshing**

Mesh generation is the practice of creating a mesh, a subdivision of a continuous geometric space into discrete geometric and topological cells. Often these cells form a simplicial complex. Usually, the cells partition the geometric input domain. Mesh cells are used as discrete local approximations of the larger domain. As the concept of the FEM is based on the decomposition of a continuum into a finite number of discrete elements, the solution obtained, in general, will be only an approximation to the exact solution. The error of the approximation depends on the nature of the problem, the accuracy of individual elements, the number of elements used and the position of the sampling nodes, etc. Before analyzing the response of a structure subjected to loading, an FE model must be created. Based on these data, the software forms the element stiffness matrices  $[k]$ , assembles them into the structure stiffness matrix  $[K]$ , applies the boundary and loading conditions, and then uses the Gauss elimination or an equivalent method to find the nodal displacements. The user must discretize the structure, numerically idealize each member, prescribe boundary conditions, and apply loading conditions. In FE terminology, the word mesh is defined as the collection of nodes which contain information related to geometric locations and elements which prescribe the order of connectivity between nodes. Nodes are known as grid point. In a global coordinate system, the location of a point is defined in a rectangular or spherical space. Commonly used coordinate systems include the Cartesian coordinate system, polar coordinate system, and spherical coordinate system. At each node, any constrained DOFs can be prescribed, and the responding DOFs due to applied forces and moments can be calculated. In theory, all nodes possess six DOFs, three translations along the x-, y-, and z-axes and three rotations about the x-, y-, and z-axes. There are different types of finite elements. These are mainly classified based on geometrical dimensions, it can further add types based on element order, other or miscellaneous types.

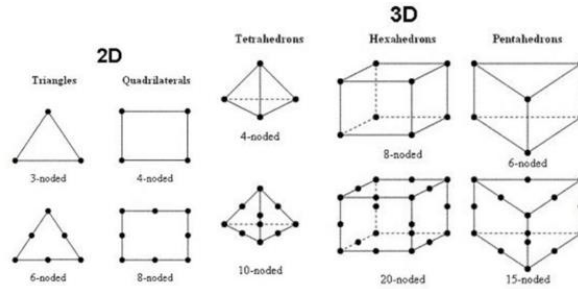


Figure 13: Types of element used in volumetric finite element modeling of solid structures.

[70]

In case of 1D elements one of the dimensions is very large compared to other two dimensions. In case of 2D, two dimensions are very large comparison with third one. Finally, in case of 3D, all dimensions are comparable for example solids. For all of elements exists two types of elements linear and quadratic. The only difference between linear and quadratic is midsize nodes. In case of quadratic element, additional midsize node in is defined in middle of each side.

## 2. ADDITIVE MANUFACTURING

### 2.1. A review of the additive manufacturing

*“Additive manufacturing (AM) is a process of joining materials to make objects from 3D model data, usually layer upon layer, as opposed to subtractive manufacturing technologies”*[71]

Additive Manufacturing, also known as 3D Printing [72], is a technology that allows you to produce three-dimensional parts, layer by layer, starting from powder, thanks to a laser source that melts the material. Alternatively, this is the technology to build metal objects with complex geometries, which is impossible to make with other traditional technologies. This process was initially identified as, the idea of fabricating product prototypes directly from computer-aided design (CAD) data [73], [74]. Since then, this technology has significantly improved speed, part accuracy and material properties and expanded the range of its application areas. The main applications of this technology included the manufacture of various types of models and prototypes, which were used for visual inspection, concept evaluation and presentation and functional testing in the various phases of the product development process [75]. All this has made AM a fundamental tool for shortening product design and development time cycles. In addition to prototyping, it showed its potential in other industries such as rapid manufacturing (RM) to produce parts for end users in small batches, rapid equipment (RT) for the manufacture of production tools or molds [76] and medicine [77].

AM technology is divided into two main phases [78]:

- Virtual: The 3D CAD model is created using 3D modelling software.
- Physical: a suitable AM process uses CAD to develop physical models.

The virtual part in detail is characterized by 3D geometric modelling, the piece is dimensioned, and the required geometry is created. The geometry is then converted to standard triangular language and pre-processed for printing. The last step of this phase is characterized by selecting the printing parameters and the orientation/positioning of the printed part on the printing plate. The physical part is characterized by being manufactured using one of the AM systems currently. The final step is post-processing. This includes removing the physical part from the platform, detaching the supports and sometimes the part requires small cleaning and surface treatment to improve its appearance and strength [79].

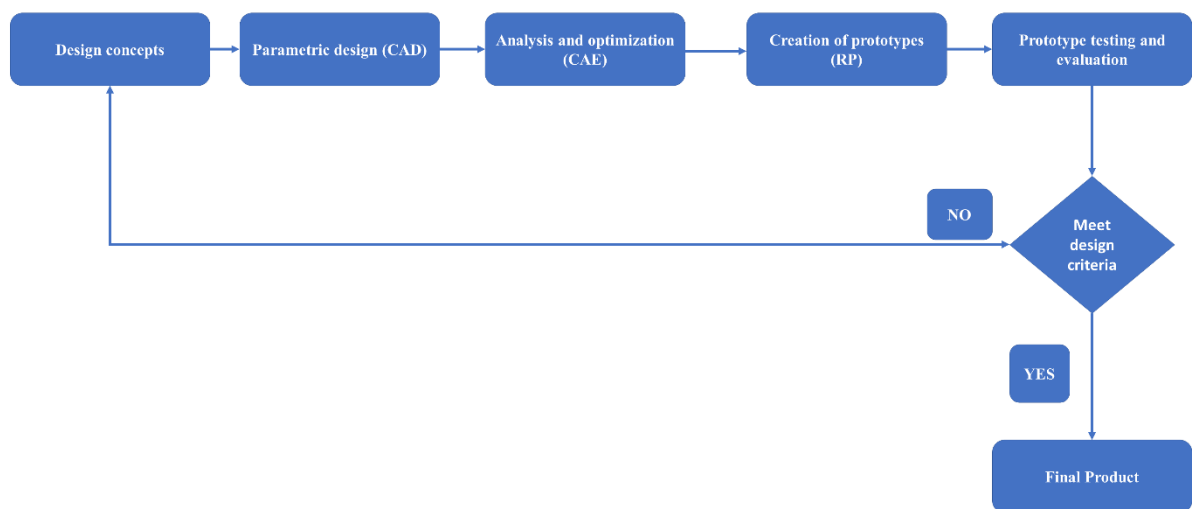


Figure 14: Product development cycle.

Some of the standard AM processes used in the manufacturing process are:

- Stereolithography (SL),
- Selective laser sintering (SLS),
- Fused deposition modelling (FDM),
- 3D printing (3DP),

- Laminated object manufacturing (LOM),
- Polyjet printing (PP),
- Electron beam melting (EBM),
- Laser engineered net shaping (LENS).

All these processes have a common feature [80], the model is manufactured by adding layer-by-layer raw materials rather than by removing or deforming materials as in conventional manufacturing processes. Furthermore, the only one a feature that makes this technology more special than conventional production is its ability to manufacture physical parts directly, i.e. it does not require any change of tools, equipment and other related activities for manufacturing purposes[81].

## 2.2. SLM/SLS and their key process variables

The doctoral thesis focuses on systems in which a focused energy beam is used to fuse dust particles in layers. The energy beam can be an electron beam or laser. Different names refer to these powder bed laser melting processes, the most common of which are selective laser sintering (SLS) and selective laser melting (SLM), depending on the nature of the powder melting process.

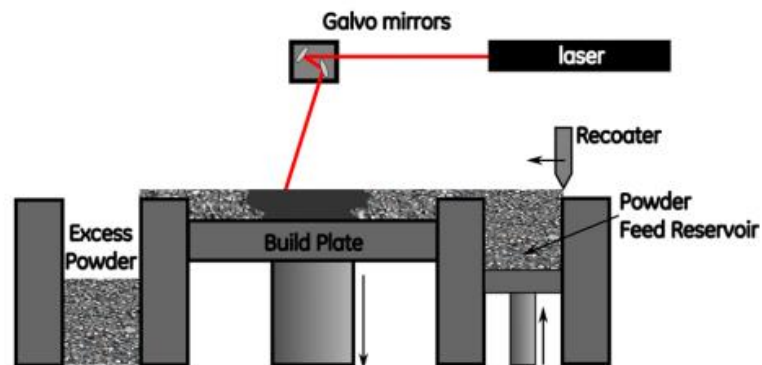


Figure 15: Illustration of a typical SLM or SLS process [82]

A typical SLS or SLM process is illustrated in Figure 15. The powder feed is contained in a hopper or distributor bed. In the embodiment illustrated in Figure 15, an elevator in the powder hopper raises a prescribed dose of powder above the build plate level, which is then spread in a thin and uniform layer on the construction surface by a covering mechanism. The overcoating mechanism can consist of a stiff scraper, a soft squeegee, or a roller [83]. The powder can also be supplied from a hopper above the build surface. The dust thickness of the layer is generally

between 10 and 100  $\mu\text{m}$ . Selective portions of the powder layer corresponding to a slice of the piece to be produced are then sintered or fused by a laser scan focused on the entire surface. Lasers in the metal powder bed are typically fibre lasers with wavelengths between 1.06 and 1.08  $\mu\text{m}$  and powers of the order of magnitude of 100 s Watt. The process is repeated to build a finished part in a layer-by-layer fashion. For metals, the process is typically carried out, in a nitrogen or argon atmosphere with very low oxygen content to prevent oxidation of the metal during the fusion process. 50 Parameters affect the final quality of the finished part in SLM / SLS processes[84], [85]. Four categories can enclose them [86]:

- Scanning and laser parameters,
- Powder material properties,
- Properties of the powder bed and coating parameters,
- Building environment parameters.

These categories are divided into:

- controllable parameters that can be manipulated during the build process
- default parameters are determined at the start of a build and remain fixed throughout the process.

SLM / SLS is essentially a heat transfer process in which energy from a laser is transferred to a powder bed, heating and then melting the powder, after which the melt is allowed to cool until it becomes solid. The laser is the source of energy in the heat transfer process. The power delivered by the laser is a function of:

- output power ( $P_L$ )
- laser mode (continuous or pulsed)
- area where the beam energy is applied (spot size)
- amount of time that energy is applied to given area of the dust bed.

The power is adjustable on different levels. It is possible to use different laser powers on the contours of the parts to control the surface finish than those used in the internal region. Continuous lasers are the standard in industrial machines; However, in [87], [88] the advantages of pulsed laser are shown in the prevention of cracking or material microstructure [89], [90]. If the laser is used in a pulsed mode, the peak power, pulse width, and pulse frequency may be added to the list of variables that affect the output of an SLM or SLS

process. Wavelength and polarization can have a significant impact on absorption [91]. The laser scan speed ( $v$ ) is a critical process parameter, as it represents how long the laser power is applied to a particular point [92]. Typical laser scanning speeds are on the order of 10-100 s of millimeters per second. The geometry of the part and the model or scanning strategy also affect the heat transfer environment in the vicinity of the melt pool. The powder has different thermal transport properties than the molten material. Therefore, if a large solid part is being scanned, the part itself it becomes a heat sink through which energy is conducted away from the fusion pool. When scanning on a small solid mass instead, the conductive dissipation of thermal energy away from the melt pool will be slower. The laser scanning strategy influences the finished piece's resulting properties [93], [94]. Common scan patterns include arrays of parallel strips, spirals or outlines from the outside edge of a part in the center and/or zigzag traces [93], [94]. The implementation of these scanning strategies requires the specification of multiple process variables, such as the width of the strip, the overlap of the strip and the direction. A parameter common to all scan strategies is the scan spacing ( $S_s$ ) or distance between neighboring passages of the laser. Some degree of overlap between the nearby areas of the melting tank are required to ensure that the material is completely dense and reaches full strength. Ensuring the laser is focused on the desired position and moving at the specified speed is critical to controlling component variability in SLM and SLS processes. the shape of the dust particles, the surface roughness and dimensional distributions can be important as they affect light absorption [95], [96], the flowability of the powder during the enrobing process, packaging of the powder in the bed and the uniformity of the layers deposited in the coating process. If the powders are reused, these properties are subject to change[97]. Powder bed temperature affects thermal gradients in the heat transfer process illustrated, which ultimately affects internal stresses in finished parts[84]. The high temperatures required to melt or sinter metals require that SLM and SLS constructions be performed in a controlled low oxygen atmosphere to prevent oxidation, decarburization and other problems that can adversely affect the mechanical properties of the finished part [84]. This thing is achieved by using a combination of positive pressure from an inert process gas, usually argon or nitrogen, and a vacuum pump to remove air from the construction space [84]. In SLM, a plasma plume is typically seen above the weld pool. This plasma consists of ionized gas from the construction atmosphere and vaporized and/or ionized metal from the powder bed [98]. This plasma plume can be absorbed and/or refract the laser radiation, thus affecting the absorption of energy by the melt bath/powder bed [98], [99]. Small changes in oxygen composition (0.1 to 1.0 vol%) lead to significant weld pool changes when small amounts of oxide form on the surface of the melt,

modifying the surface tension [100]–[102]. Any change in the size of the weld pool would impact the heat transfer process. Changes in surface tension can also lead to Rayleigh instability in the weld bead during an SLM process [103].

### **2.3. Comparison between Additive Manufacturing and traditional method in prosthetics field**

Prosthetics and orthoses are common aids that help people with disabilities meet their biomechanical needs. Prostheses are used to replace missing body parts of the lower limb or upper limb [104]. The prosthetic socket is a cup-like structure it fits around the amputees' residual limb and transfers mechanically load from the body to the prosthesis. Orthoses are classified into upper limb orthoses, spinal orthoses, and lower limb orthoses. The traditional is the most widely adopted manufacturing method for customized orthoses and typically involves plaster cast and is highly patient-centric personalized process. In contrast to traditional subtractive production, AM has significantly reduced material waste, shortened the manufacturing period and eliminated the need for most skill-based manual operations [105]. In the traditional manufacturing process, a patient performs anthropometric measurements. Later a cast mould is obtained by wrapping plaster bandages around the affected body area. A positive mould is then made by pouring plaster into the negative mould. Next, the prosthesis or orthosis is made by heating and thermoforming sheets of thermoplastic material on the positive patch moulds, which are left to cool and then trimmed inside the correct form. Further adjustments are required in most cases to ensure the comfort and functionality of the product. This procedure involves the waste of materials and has high labour times and costs. The products' quality hugely depends on the prosthetist's or orthopedist's skill and experience [106]; therefore, it is not practical to produce repeatable results. With AM, complex structures can be created, saving time and labour costs. AM has a flexibility that allows customization for particular applications or consideration of individual characteristics [107]. AM allows for precise replicas of existing products [108] and makes it possible to increase functional performance with less weight. Furthermore, integrating functions in AM can reduce the need for assembly procedures [109]. Finite element analysis was used in AM processes to predict and optimize mechanical characteristics and functional performance. Optimization of material distribution while maintaining the rigidity of the design can be done through a topological approach, which is impossible in traditional procedures [110]. The primary constraint of this technology is the combination of dissimilar materials, due to differences in thermal expansion/contraction and mismatch in heat release, which it would not be a problem in

traditional manufacturing [111]. Studies [112], [113] have outlined new methods of manufacturing prostheses and orthoses using body scanning, CAD and AM technologies. SLS and FDM techniques were used production of ankle-foot orthoses. Both methods required scanning the foot and using a simulation of the ankle-foot orthosis model [114]. Various types of customized orthotic insoles have been made using AM technologies and have been compared with traditional ones products manufactured through observation of gait and subjective assessment of fit and comfort [115]–[117]. An evaluation of orthoses made with SLS for patients with rheumatoid arthritis showed similar results in walking with traditional orthoses, and the patients did not feel any difference in terms of comfort and fit [118]. Orthotics with adjustable elements to relieve plantar pressure and an adjustable stiffness ankle-foot orthosis were designed and manufactured using AM technology and tested with a healthcare participant [119]. The results proved that both AM-fabricated orthoses could meet the functional requirement. This study indicated AM's availability to manufacture new customized orthotic devices.

#### **2.4. SLM lattice structures: overview**

Additive manufacturing (AM), particularly Selective Laser Melting (SLM), has enabled the development of lattice structures with unique properties. By controlling various parameters, lattice structures can produce unique mechanical, electrical, thermal, and acoustic properties and have received much research attention. Despite the increasing volume of published data on the mechanical response of specific SLM lattice structures, no overarching analysis exists. The lattice structures can be 2.5D [120] or 3D and can be fabricated by a variety of means, including investment casting [121], a combination of extrusion and EDM machining [122], or various methods of manufacturing composites, including weaving fabrics [123], interlaced, interlocking, hot pressed [124] or filament winding [125]. Lattice structures can generally be classified according to their mechanical response as dominated by bending or dominated by elongation. The cellular topology of a lattice structure defines if will be bent or dominated by elongation. The most common strut-based cell topologies that have been studied are the body-centred cube (BCC) and the face-centred cube (FCC), or variations of these, such as the inclusion of z-struts (BCCZ and FCCZ) (Figure 16) [126], which are named after analogues crystalline structures.

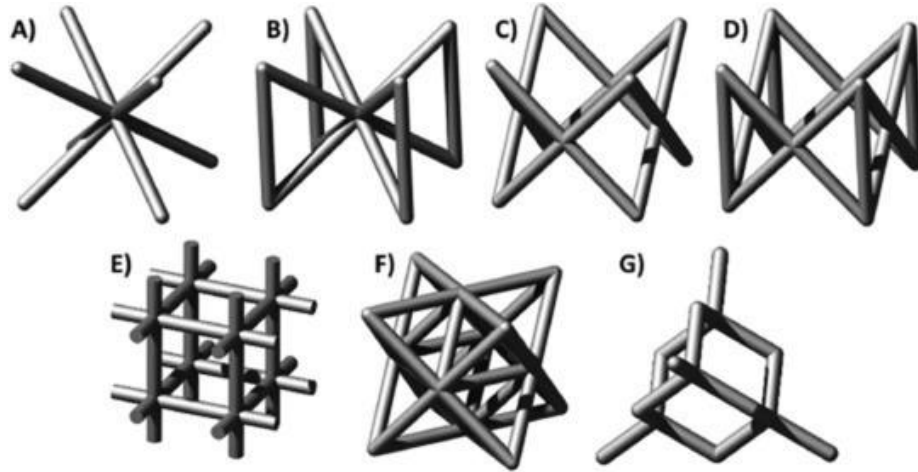


Figure 16: Strut-based lattice structures: BCC (A), BCCZ (B), FCC (C), FCCZ (D), cubic (E), Octet-truss (G), and diamond (H).[127]

There are other strut-based topologies, such as the cube, the octet-truss and the diamond. These strut-based topologies are often chosen for their simplicity of design. Strut-based topologies can be characterized by their Maxwell number,  $M$ , which depends on the number of rafters,  $s$  and nodes,  $n$

$$M = s - 3n + 6 \quad (61)$$

If  $M < 0$ , there are too few struts to balance the external forces without balancing moments induced at the nodes, causing bending stresses to develop in the struts and leading to dominated bending behavior[127]. While if  $M \geq 0$ , the external loads are balanced by axial tension and compression in the struts, which means no flexing occurs in knots, making these structures dominated by elongation [128]. Because of these phenomena, structures dominated by elongation are rigid and robust, especially considering their mass, while structures dominated by flexion conform and deform more consistently [129]. Various parameters, such as periodicity and relative density, can be modified to optimize their mechanical performance [130]. The periodicities are defined by the  $k$  values ( $k_x, k_y, k_z$ ) which are calculated using

$$k_i = 2\pi \frac{n_i}{L_i} \quad (62)$$

where  $n_i$  is the number of cell repetitions in the  $x, y$  or  $z$  directions, and  $L_i$  is the absolute size of the structure in that direction. The variable  $t$  can be used to change the relative density.

Rapid progress has led to an interest in AM for a wide range of applications including personal protective equipment [131] and sports equipment. Two sectors that have been particularly interested in the AM network facilities are the biomedical and aerospace industries [132]. The ability to produce high-quality metal components that conform to complex, patient-specific surfaces make SLM perfect for manufacturing medical products. The ability to produce metal components with stiffness closer to bone makes AM reticular structures perfect for biomedical applications [133]. These structures can be designed to produce optimal osseointegration and have been shown to support excellent bone growth and achieve high performance in implant fixation [134]. Various terms such as mechanical properties, elastic modulus and yield strength are applied to lattice structures, although they have a slightly different meaning than when applied to continuo bulk materials. When referring to reticular structures, these properties are the "apparent macroscopic properties of structures which converge to specific values when it is the number of unit cells big enough "[135]. Due to the geometric freedom offered by AM, lattice structures can obtain functional or mechanical properties which cannot be obtained with bulk materials [136] such as auxetic structures with negative Poisson's ratio [137], negative stiffness [138], negative compressibility, negative thermal expansion coefficient [90] or very high stiffness with low mass [139]. The mechanical properties of lattice structures are usually expressed as a fraction of the mechanical properties of their starting material [135] and depend on the relative density of the reticular structure ( $\rho^*/\rho_s$ ), which is the ratio of the apparent density of the cell structure  $\rho^*$  to the density of the cellular structure material ( $\rho_s$ ). Regardless of the topology, the mechanical properties of lattice structures are known to decrease with reduced relative density [140]. The orientation of the cells concerning the load direction also significantly affects the mechanical response of the anisotropic reticular structures [135]. The tensile behavior of the lattice structures remains a required area further research. The fatigue performance of SLM lattice structures is critical for many high-value technical applications. For example, biomedical and aerospace components are subject to stringent requirements and limits associated with cyclic load [141]. The fatigue behavior of lattice structures subject to dynamics the load can be divided into three phases:

- phase 1 the deformation increases quickly.
- phase 2 the cumulative deformation remains approximately constant for about  $10^4$ - $10^6$  cycles;
- phase 3, cumulative strain increases exponentially, resulting in the rapid failure of the exemplary [141].

The factors that most significantly affect the fatigue properties of the reticular structures are:

- the mechanical properties of the bulk material.
- the relative density of the lattice.
- cell topology;
- geometry of the uprights of the cell, which is defined by the distribution of the material within the structure [141].

The fatigue behavior of SLM lattice structures with some topologies and relative densities are compared in Figure 17.

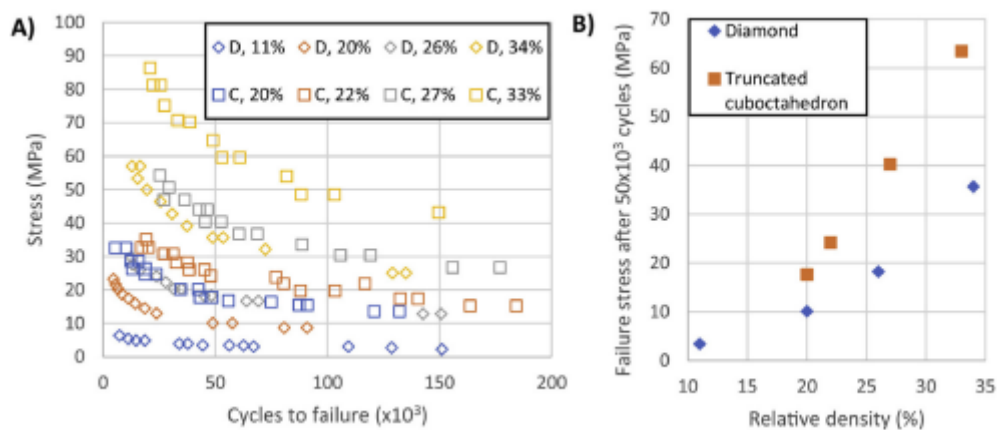


Figure 17: A: Comparison of fatigue behaviour of SLM lattice structures with diamond (D) and truncated cuboctahedron (C) topologies and varying relative densities (%). B: Failure stress after  $50 \times 10^3$  cycles for different topologies and relative densities [127].

Lattice structures with higher relative density could support more loads for a more significant number of cycles than those with a lower relative density (Figure 17 A). However, truncated cuboctahedron reticular structures could withstand higher loads for similar periods than the diamond grating structures with similar relative densities (Figure 17 B). Tensile loads cause bending stresses in the posts in bending-dominated structures. These stresses can give rise to cracks inside the struts propagating up to the final fracture. As more struts fail, the load-carrying capacity and stiffness of the fatigue load of the structure diminishes until complete catastrophic failure [141].

### 3. HUMAN ANATOMY TERMINOLOGY AND POSE DETECTION METHOD

#### 3.1. Terminology and Human standards

The human body can be divided into 14 main segments[142] (Figure 18)

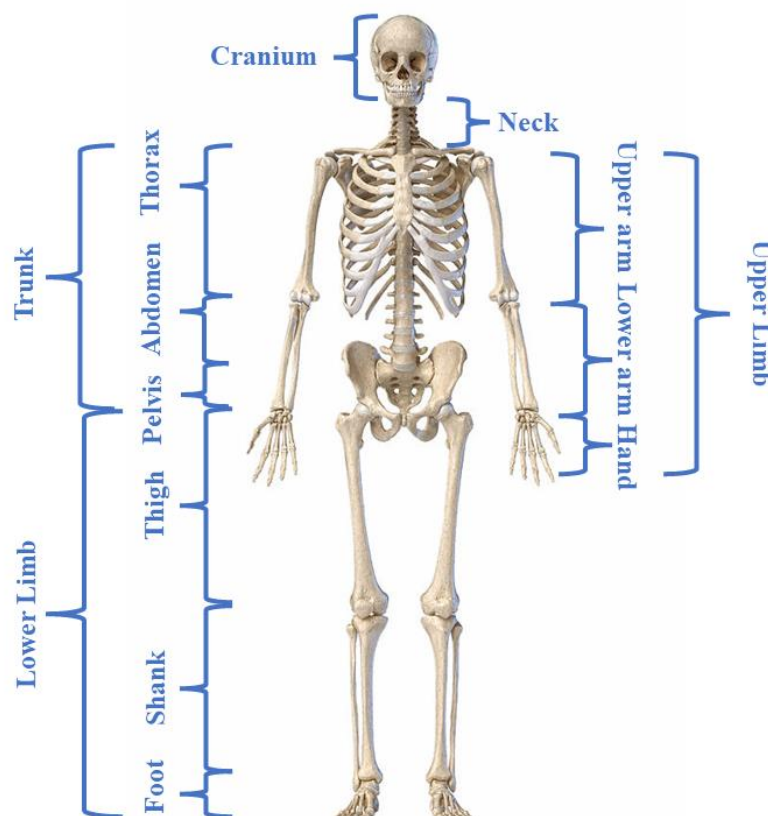


Figure 18: Principal members of the human body

When experimenting in the field of biomechanics, the conventions relating to this field must first be defined. The ISB sets the standards for the biomedical sector. A global coordinate system must be defined to describe human kinematics independently of the type of experimentation conducted. As in [143], a right-handed orthogonal triad fixed in the ground with the + Y axis upward and parallel with the field of gravity, X and Z axes in a plane perpendicular to the Y axis must be defined.

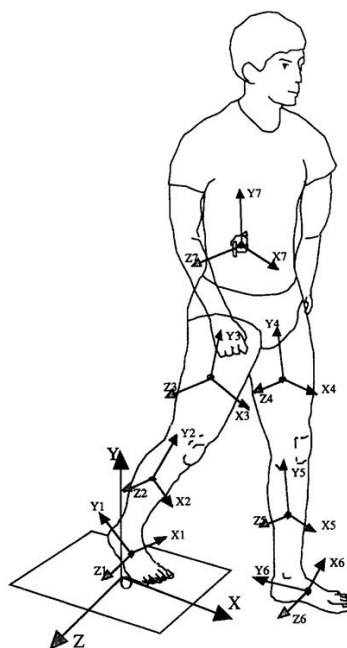


Figure 19: Conventions for global reference frame and segmental local center of mass reference frame [143].

Another defining thing is that the + X axis is defined as the direction of travel or work (defined by the investigator). In the case of locomotion on inclined planes, the Y axis will remain vertical, and the X and Z axes will be in the same horizontal plane[143]. The nomenclature refers to an anatomical position of the reference, to describe a movement. The position is supine and extended with the arms along the trunk and the palm facing upwards. In this position, three planes are described: sagittal, frontal, and median. Their intersection defines the center of gravity of the human body (Figure 20).

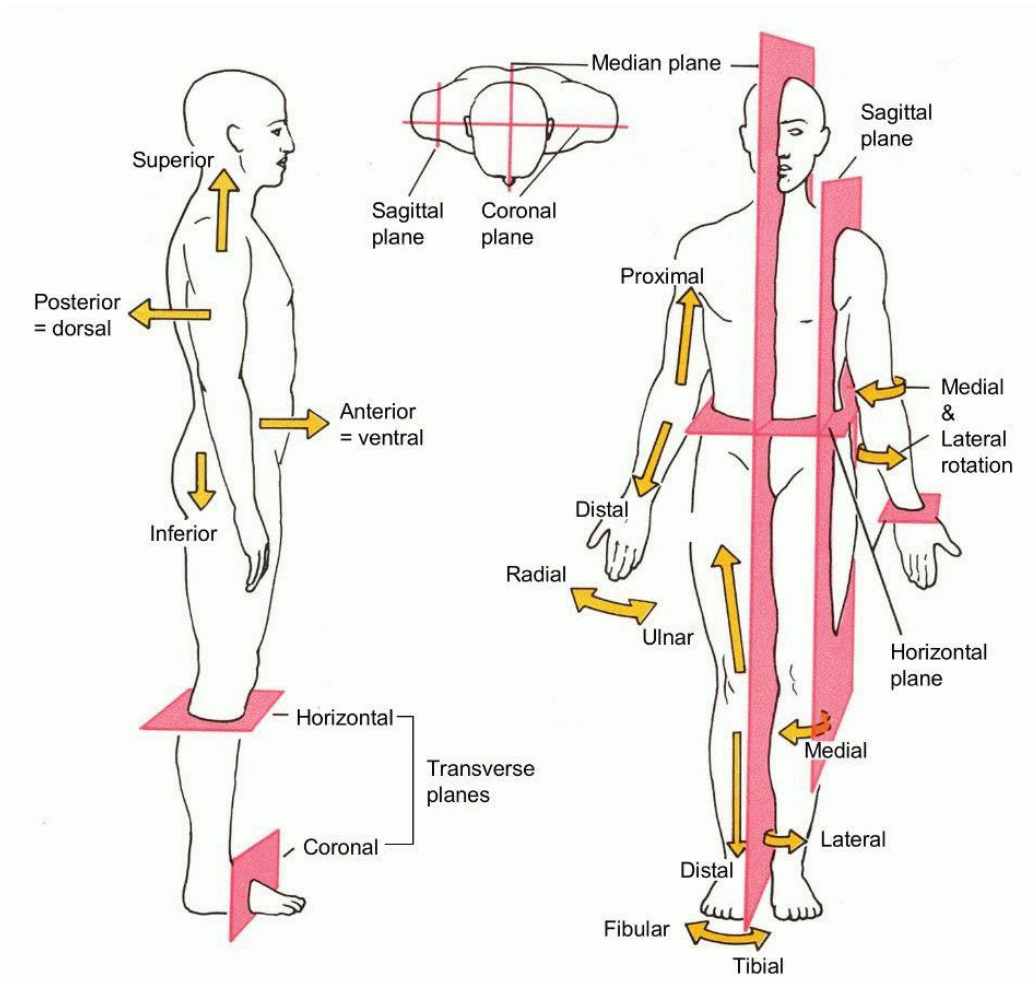


Figure 20: Directions, orientations, and planes used to describe the body in anatomy.

Along the sagittal plane, assuming to choose a direction of travel "r", two nomenclatures can be defined. In the vertical direction, a proximal position can be defined for all values that tend to make the module of this vector negative. The distal position is defined for all values where "r" increases. In other words, everything far from the sternum assumes a distal position. In contrast, everything close to the sternum assumes a proximal position. In the case in which it is hypothesized that this line is horizontal, it can be defined that everything close to the sagittal plane is in a medial position, and everything far from the sagittal plane is in a lateral position (Figure 21).

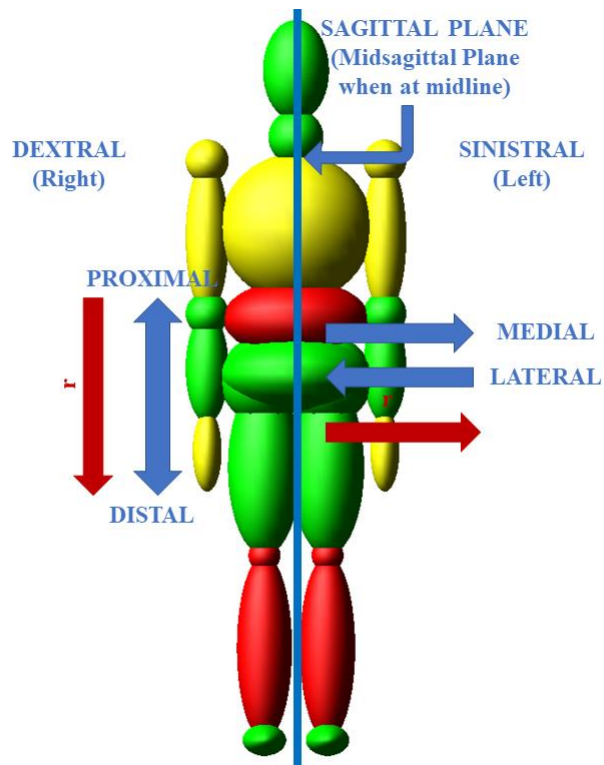


Figure 21: Anatomical plane: Sagittal plane, proximal/distal and medial/lateral definition.

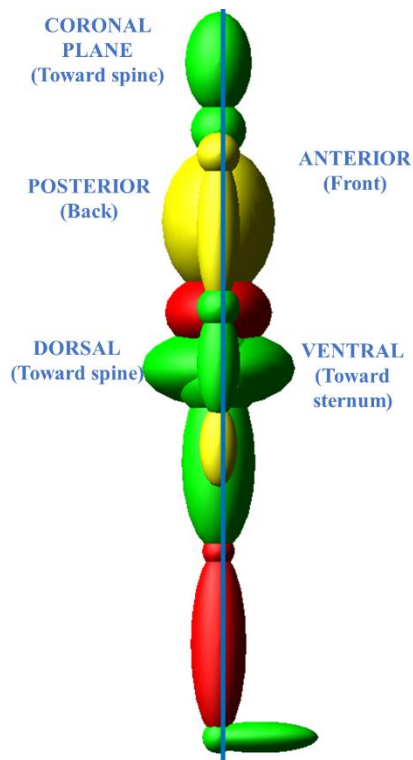
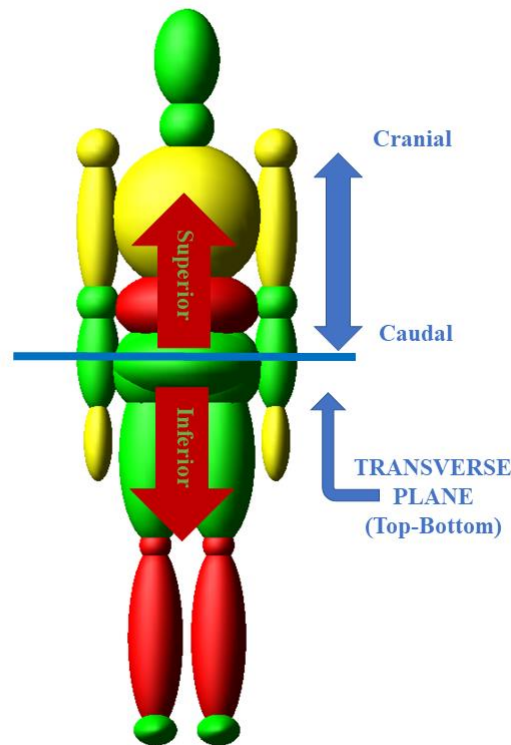


Figure 22: Anatomical plane: Coronal plane, Anterior/Posterir and Dorsal/Ventral definition.

Two areas can be identified, considering the coronal plane, the front (anterior) and the posterior. The first is located in front of the coronal plane, and the second is behind. As for the position, everything that is anterior to the coronal plane is defined in the ventral position and vice versa. It is identified in the dorsal position.



*Figure 23: Anatomical plane: Transverse plane, cranial caudal definition.*

Finally, the transverse plane divides the body into upper and lower portions. Everything far from the transverse plane is in the cranial position; on the contrary, the rest is in the caudal position. The floors considered are the main floors, but secondary ones can be defined parallel to these.

### **3.2. Anthropometry**

Anthropometric studies date back over two millennia. This material was necessary due to the continuous evolution of technology, especially in the relationship between man and machine, or with the taking of issues related to ergonomics or comfort. Industrial requests are aimed at obtaining surveys of overall dimensions or volumes, but in some cases, kinematic or dynamic models are developed, in which a more accurate analysis is needed. To undertake an anthropometric study, a large amount of data collected by analyzing live subjects or corpses is required and must be processed with appropriate statistical or deterministic tools. The

evaluation of measures such as height can be calculated directly on living subjects. As for limb mass measurements, inertia or centres of mass analysis must be carried out on cadavers or using techniques such as X-rays, CT or NMR [144]. The relationships obtained from the analysis of the following data have an empirical nature and fully reflect the characteristics of the sample in question. To avoid estimation errors and since these measures are inherited from specific characteristics of the population and the scenario, classifications must be made upstream of the analysis, based on parameters such as the sex of the subject, race, and age. In the field of anthropometers, numerous indices are used for the classification of subjects, the most common being the BMI (Body Mass Index). The BMI is a biometric data that relates the mass and height of an individual and is used as an indicator of a person's ideal weight. It can be used to classify individuals according to their build [145]. The body mass index is defined as:

$$BMI = \frac{m}{h^2} \quad [kg/m^2] \quad (63)$$

Where  $m$  represents the mass in kg and  $h$  is the height in m. In medical and engineering fields, an attempt is always made to identify an average man/woman representative of the population under examination. Unfortunately, this subject does not exist. However, it can be said that anthropometric measurements are arranged according to a Gauss distribution which can be described using indicators such as mean and square deviation. Considering a high number " $n$ " of subjects of height  $h_i$ , the average height  $\bar{h}$  and the standard deviation  $\sigma_h$  are:

$$\bar{h} = \frac{\sum_{i=1}^n h_i}{n} \quad (64)$$

$$\sigma_h = \sqrt{\frac{\sum_{i=1}^n (h_i - \bar{h})^2}{n}} \quad (65)$$

As shown in the equations previously defined, it can be deduced that in this field, we can rely on population percentiles. Thanks to the percentiles, it is possible to define all subjects below a certain threshold. The human body is made up of deformable segments articulated together. To describe the dynamic behaviour of man, the specific quantities of the segments must be identified, such as size, the position of the centre of mass, moments of inertia and the

orientation of the principal axes of inertia. Among the models used, the simplest is that of Drills and Contini [146], [147], which estimates the segments as a function of the subject's height(Figure 24).

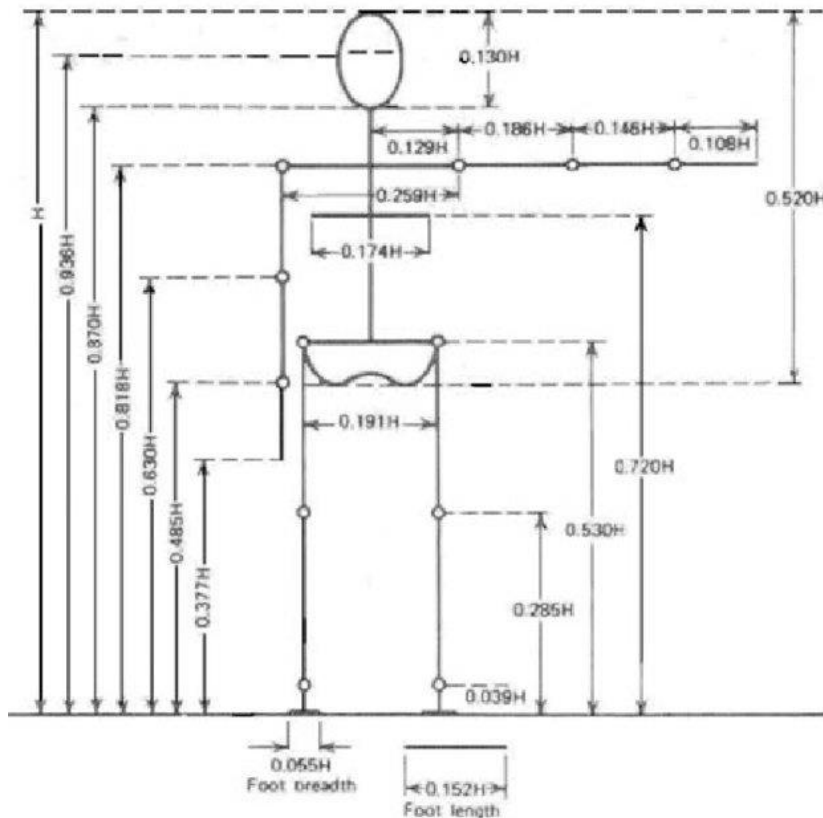


Figure 24: Body segment parameters[146], [147]

The body segments are made up of numerous tissues characterized by different densities. For this reason, there are formulas to calculate the average body density based on weight and height:

$$\rho = 0.69 + 0.9 \frac{h}{\sqrt[3]{m}} \quad (66)$$

Where h indicates the height in m and m indicates the weight in kg. A possible division into segments of the human body and the estimation of the density values was made by Dempster and Clauser, who referred to data obtained on cadavers[148], [149].

### 3.3. Human joint

Two types of joints can be identified within the human body:

- fibrous (bones joined by connective tissue)
- cartilage (bones joined by cartilage).

As seen in Figure 25, in synovial joints cartilage layers on the ends of opposing bones are contained in a sac containing synovial fluid. The coefficient of friction in such joints is lower than any joints made by mankind.

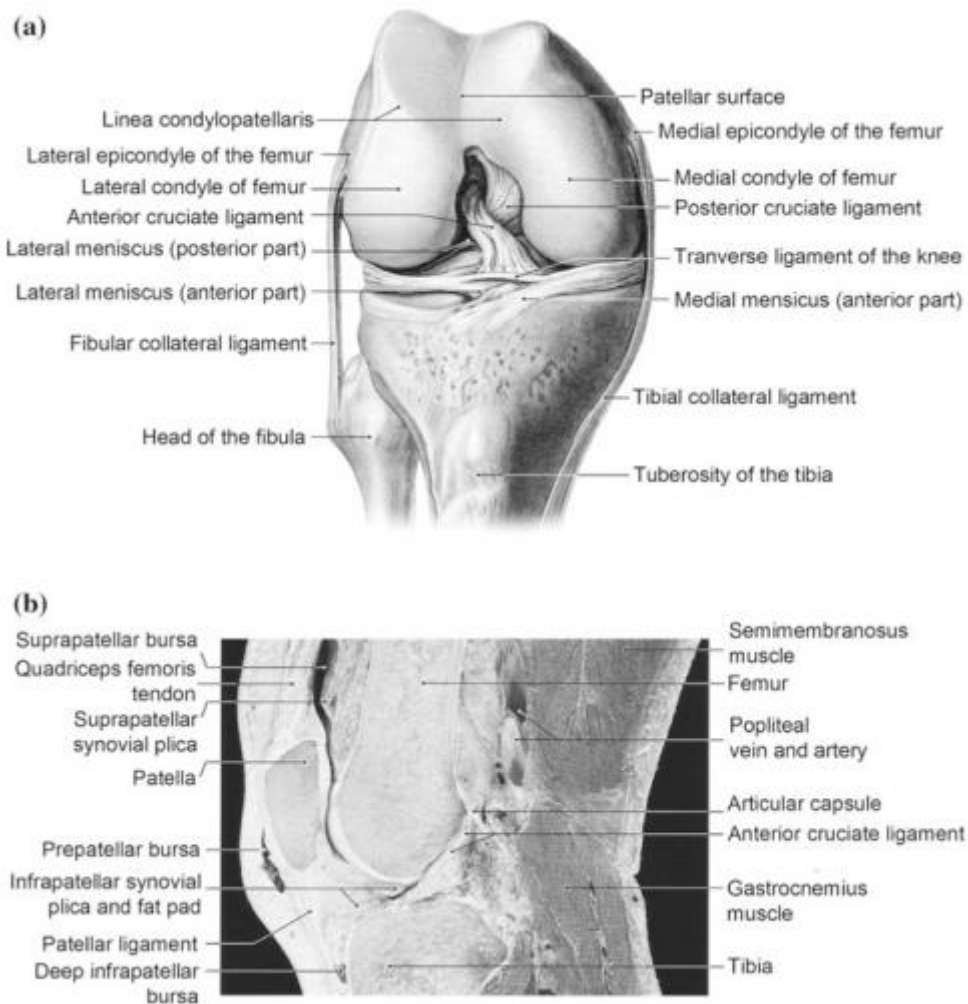


Figure 25: The right knee synovial joint, with a anterior view with the kneecap (patella) removed and b in sagittal section (photo) [150]

There are several types of synovial joints in the body, each with one, two, or three degrees of angular motion. Condylod or ellipsoidal joints are ball-and-socket joints with ellipsoidal balls and sockets. They have only two degrees of freedom because rotation is impossible about the ball's axis emanating. The upper leg bone (femur) is connected to the hip as a ball-and-socket joint (three DOFs). The hip bone is connected to the thigh with a hinge (one DOF). The ankle is a saddle joint (two DOFs). This means that each leg has six degrees of angular motion, as needed for the complete location of the foot. Several of these degrees of freedom have only limited angular motion. The upper arm (humerus) fits into the shoulder as a ball-and-socket joint (three DOFs). The elbow is a hinge (one DOF). The wrist is an ellipsoidal joint (two DOFs). That makes six DOFs. When the angle of a 1D hinge, such as the elbow, increases, it is called extension; when it decreases, it is flexion. When a person rotates his leg away from the body's midline, it is abduction, and when he brings his closer to the midline, it is adduction. Rotating a body part about its long axis is called rotation. The screwdriver motion in the arm is pronation (a front-facing hand rotates towards the body) or supination (away from the body). Supination is the motion of a right hand screwing in a right-handed screw (clockwise looking distally from the shoulder to the hand). Pronation is that of a right hand unscrewing a right-handed screw (counterclockwise looking distally from the shoulder to the hand)

### **3.4. Gait analysis**

Walking is a standard method of locomotion. It is reproduced by alternating the use of legs to produce propulsion in such a way as always to keep one foot in contact with the ground. Numerous muscle groups belonging to the musculoskeletal system take part in this act. There are two types of steps:

- **Static:** moving slowly by dragging from one posture to the next so that the weight force always passes through the support base of the foot. All intermediate postures are positions of balance.
- **Dynamic:** the upright position of the body resting on a reduced base, which can be represented by the foot. This walk forces the whole body to take part in the action to be able to maintain movement. We always move around a point of equilibrium, but the positions are not static equilibrium.

Forces and torques are transmitted to the body via the joints, ligaments, and tendons. The accelerations generated by the upper body keep the body in balance or generate the desired

movement by combining the forces generated by the lower body [151], [152]. The surveys for gait analysis are represented by:

- Subjective observations
- Quantitative methodologies
- Photogrammetric systems
- Platforms of force
- Kinematic and dynamic simulations
- Electromyography
- Energy consumption

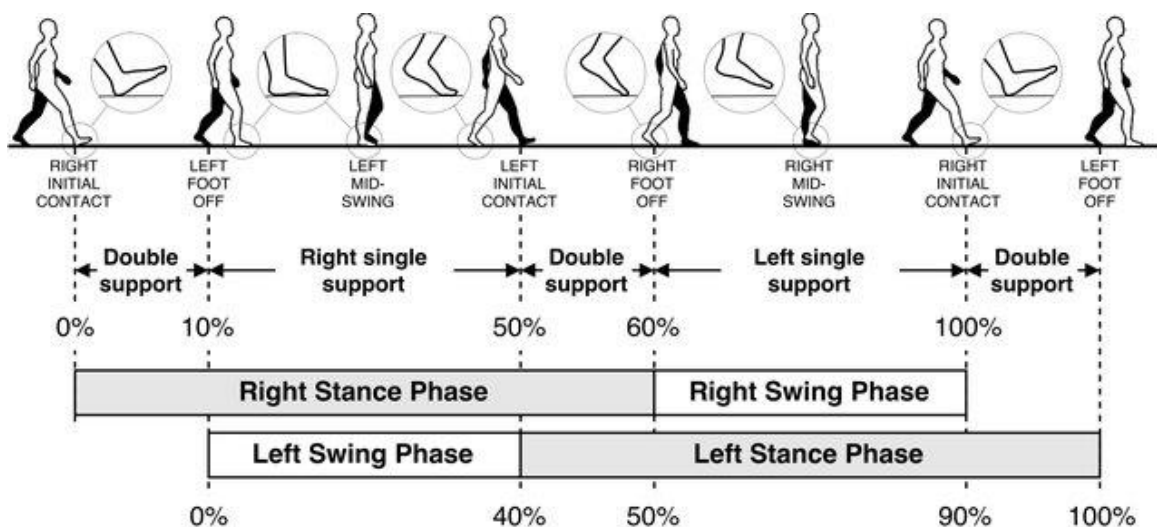


Figure 26: Human gait cycle.[153].

The gait cycle is the entire sequence that goes from the beginning of the support on the ground of one foot to the beginning of the following support of the same foot. The single step, on the other hand, is represented by the mass sequence that ends with the start of the support of the contralateral foot. For each of the two legs, two phases are defined during the walking cycle:

- support phase (stance): begins when the foot first touches the ground and ends when the same foot leaves the ground. The stance phase makes up approximately 60% of the gait cycle.

- suspension phase (swing): begins when the foot first leaves the ground and ends when the same foot touches the ground again. The swing phase makes up the other 40% of the gait cycle.

when we talk about walking, we refer to two specific quantities:

- Cadence (steps / min)  $c$
- Cycle time  $t_c$

The step frequency  $f_p$  is obtained by dividing the cadence by 60; alternatively, the cycle frequency  $f_c$  is obtained by dividing the cadence by 120. The speed of path  $v$  can be calculated as a function of the length of the step  $l_c$  and the respective frequencies[154].

$$t_c = \frac{120}{c} \text{ [s]} \quad (67)$$

$$v = l_c f_c = l_p f_p = \frac{l_c}{t_c} = \frac{l_p}{t_p} \text{ [m/s]} \quad (68)$$

Walking speed, as shown , varies with stride length or stride frequency.

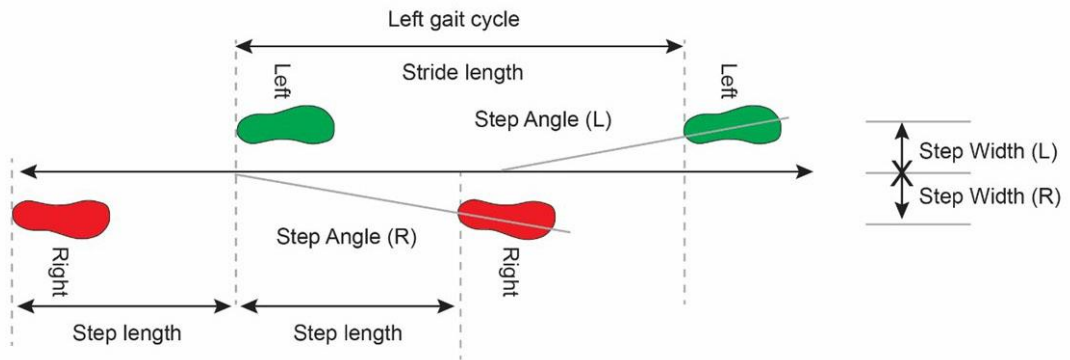


Figure 27: Step parameters.

The length of the step is related to the frequency by the following relationship:

$$l_p = q + b f_c \quad (69)$$

$b > 0$

(70)

$q$  and  $b$  are constant coefficients defined based on the person who undergoes the examination. To better understand how the foot functions, the stance phase can be further broken down into more refined sub-phases to enable a more in-depth look. These phases are called:

- Contact phase: is the first heel contact of the lead leg and ends at the “toe-off” of the contralateral leg. The contact phase makes up 14-20% of the stance phase.
- Foot-flat: or “loading response” phase is essential since body weight is transferred to the lead leg at this point and thus must absorb this weight while maintaining forward momentum. This phase is defined by the first heel contact of the lead leg to the first contact of the first metatarsal head of the lead leg. The foot-flat phase makes up 16-22% of the stance phase.
- Mid-stance phase: the support limb moves from shock absorption to more of a stability function. This phase is defined from the toe-off point of the contralateral leg to the first point the heel comes off the ground of the lead leg. The mid-stance phase makes up 29-37% of the stance phase.
- Propulsive phase (active and passive): During the propulsive phase, the foot typically supinates to allow for a more rigid mid-foot, so it can act more like a lever (Windlass mechanism) to help propel the body forward. The propulsive phase of gait is sometimes broken down into an active and passive propulsive phase. The reason for this division is to isolate the component of the propulsive phase while still in single support and the passive component of the propulsive phase when in double support. The total propulsive phase is the point at which the heel comes off from the lead leg to the toe-off of the lead leg. This phase makes up 45-55% of the stance phase.

### **3.5. Human pose estimation**

Many biomechanical analyses provide an adequate representation of the underlying skeletal structure for describing motor coordination and functional performance. Pose estimation is a prevalent task in Computer Vision. In artificial intelligence (AI), computer vision enables machines to perform image processing tasks to imitate human vision. Essentially it is a way to

capture a set of coordinates for each joint (arm, head, torso), which is a critical point that can describe a person's pose. The connection between these points is known as a pair. The connection between the points has to be significant, meaning that not all points can form a pair. From the outset, HPE aims to form a skeleton-like representation of a human body and then process it further for task-specific applications. However, There are three types of approaches to modelling the human body [155]:

- Skeleton-based model
- Contour-based model
- Volume-based model

The motion capture technique often defines the trajectories of the body's joints in multi-body simulations. With it, the movement of an object is recorded through various video capture devices arranged in space. From the recorded images, it can find the coordinates (X, Y, Z) of a series of markers affixed to the subject; this allows to quantify the position, the speed, the acceleration of these points and, consequently, the movement produced by the subject during a determined action. It will allow us to fully understand the mechanical characteristics underlying the activities of the human body and the rules for controlling motor skills. All approaches for pose estimation can be grouped into bottom-up and top-down methods[156]:

- Bottom-up methods estimate each body joint first and then group them to form a unique pose. Bottom-up methods were pioneered with DeepCut (a method we will cover later in more detail).
- Top-down methods run a person detector first and estimate body joints within the detected bounding boxes.

In traditional object detection, people are only perceived as a bounding box (a square). By performing pose detection and pose tracking, computers can develop an understanding of human body language. However, conventional pose tracking methods are neither fast enough nor robust enough to occlusions to be viable. High-performing real-time pose detection and tracking will drive some of the biggest trends in computer vision. For example, tracking the human pose in real-time will enable computers to develop a finer-grained and more realistic understanding of human behaviour. Pose estimation uses position and orientation to predict and track the movement of a person or object in an image or video. Most pose estimators are 2-pass structures that detect human bounding boxes and then estimate the pose within each box. The

installation estimation works by finding the key points of a person or an object. For a human, the characteristic points are joints such as the elbow, knees, and wrists. There are two types of pose estimation: multiple pose and single pose.

- Single pose is used to estimate the poses of a single object in each scene.
- Multiple poses are used when detecting poses for multiple objects.

CNNs can learn complex features when provided with enough training-validation-testing data. Toshev et al [157] used CNN to estimate human pose, switching from the classical-based approach to the deep learning-based approach. The authors also proposed an additional method where they implemented the cascade of such regressors to get more precise and consistent results. They argued that the proposed Deep Neural Network could holistically model the given data, i.e. the network can model hidden poses, which was not true for the classical approach. there are different types of architecture such as:

- Openpose: is one of the most popular bottom-up approaches for multi-person human pose estimation. This architecture features real-time, multi-person pose estimation. OpenPose is an open-sourced real-time multi-person detection with high accuracy in detecting body, foot, hand, and facial key points. An advantage of OpenPose is that it is an API that allows users to select source images from camera fields, webcams, and others, more importantly for embedded system applications (for instance, integration with CCTV cameras and systems). It supports hardware architectures, such as CUDA GPUs, OpenCL GPUs, or CPU-only devices. The lightweight version is efficient enough for Edge inference applications with on-device processing in real-time with edge devices.
- High-Resolution Net (HRNet) is a neural network for human pose estimation. It is an architecture used in image processing problems to find what we know as key points (joints) concerning the specific object or person in an image. One advantage of this architecture over other architectures is that most existing methods match high-resolution representations of postures from low-resolution representations with respect to using high-low resolution networks. In place of this bias, the neural network maintains high-resolution representations when estimating postures. For

instance, this HRNet architecture is helpful for the detection of human posture in televised sports.

- DeepCut is another popular bottom-up approach for multi-person human pose estimation. DeepCut is used for detecting the poses of multiple people. The model works by detecting the number of people in an image and then predicting the joint locations for each image. DeepCut can be applied to videos or images with multi-persons/objects, for example, football, basketball, and more.
- Regional Multi-Person Pose Estimation (AlphaPose) is a popular top-down pose estimation method. It helps detect poses in the presence of inaccurate human bounding boxes. It is an optimal architecture for estimating human poses via optimally detected bounding boxes. AlphaPose architecture is applicable for detecting both single and multi-person poses in images or video fields.
- DeepPose: This is a human pose estimator that leverages deep neural networks. The deep neural network (DNN) of DeepPose captures all joints, hinges a pooling layer, a convolution layer, and a fully-connected layer to form part of these layers.
- PoseNet: it is a pose estimator architecture built on tensorflow.js to run on lightweight devices such as browser or mobile devices. Hence, PoseNet can estimate either a single pose or multiple poses.
- DensePose: This pose estimation technique aims at mapping all human pixels of an RGB image to the 3D surface of the human body. DensePose can also be used for single and multiple pose estimation problems.
- TensorFlow Pose Estimation: Tensorflow Lite provides pose estimation with a lightweight ML model optimized for low-power edge devices.

Deep learning algorithms need proper evaluation metrics to learn the distribution well during the training and perform well during the inference. Evaluation metrics depend upon the tasks at hand. This section will briefly discuss the four evaluation metrics required for HPE. PCP (Percentage of Correct Parts) is used to measure the correct detection of limbs. If the distance between the two predicted joint locations and the true limb joint locations is almost less than half of the limb length then the limb is considered detected. However, sometimes it penalizes shorter limbs, for example, a lower arm. In order to fix the issue raised by PCP, a new metric was proposed. It measures the distance between the predicted and the true joint within a certain fraction of the torso diameter and it is called the percentage of detected joints (PDJ). PDJ helps to achieve localization precision, which alleviates the drawback of PCP since the

detection criteria for all joints are based on the same distance threshold. PCK is used as an accuracy metric that measures if the predicted keypoint and the true joint are within a certain distance threshold. The PCK is usually set with respect to the scale of the subject, which is enclosed within the bounding box.

### **3.6. Body segment models**

Geometric modelling is a mathematical approach in which shapes are used to represent individual segments of the body. The body CAN be modelled as a combination of cylinders and spheres [158] or as functions that consider the complex geometry of individual body segments [159]. Geometric models require anthropometric measurements representing body size at various points, allowing for individualized estimates. Simmons et al. (1960) wrote the first works in this area, approximating the body as a set of cylinders and spheres[148]. Subsequently, both Hanavan [158] and Whitsett (1963) represented the body composed of 16 and 14 segments, respectively (Figure 28).

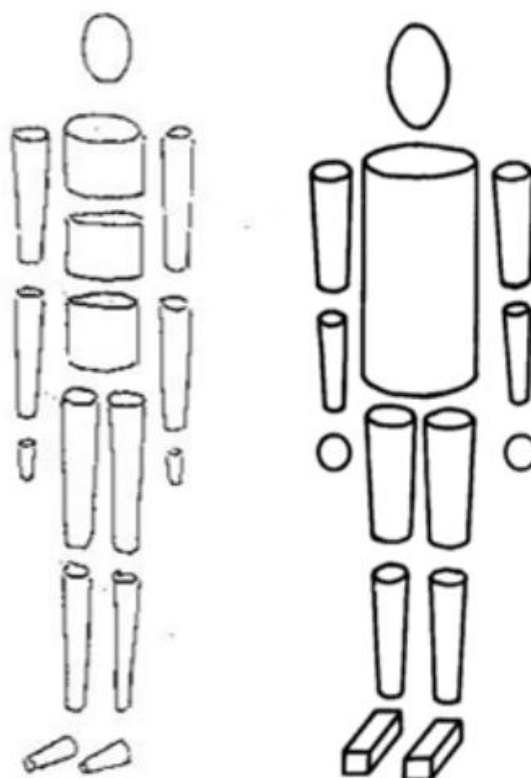


*Figure 28: Geometric models using cylindrical and spherical shapes. These models had a high degree of estimation resulting in large errors in BSIP estimations. Left Side: 16 segment model (Hanavan, 1964). Right Side: 14 segment model (Whitsett, 1963)*

Based on cadaver studies, the models used the mass regression equations developed by Barter [160]. Jensen [160] presented a geometric model, which used elliptical zones stacked on each other to represent the body. Jensen's model was based on some of the ideas proposed by Weinbach [161], which Dempster [149] considered suitable enough for volume estimation (Jensen 1978). With the Elliptical Cylinder Model (ECM), developed by Jensen, the body was segmented into 16 segments. Total body mass estimated using the ECM produced errors of less than 1.5% compared to scale measurements. Jensen's experiment showed that he could reduce the mass estimation error by about 10% compared to the results determined using Hanavan's model [158].

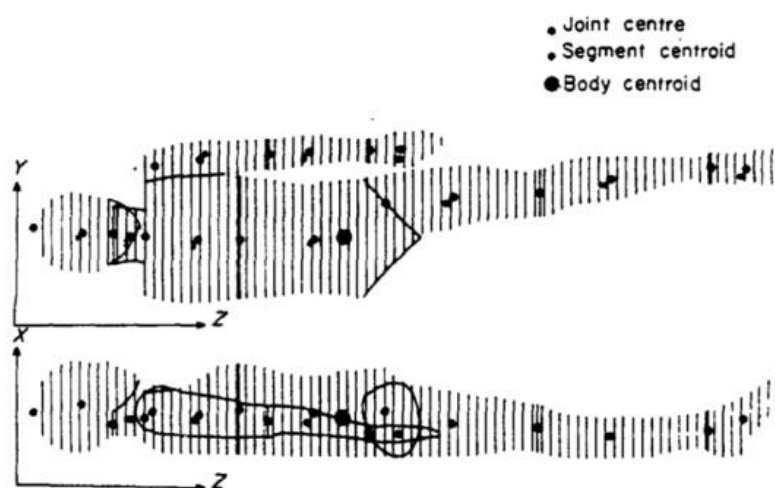


*Figure 29: The Elliptical Cylinder Model (ECM) proposed by Jensen [160]. The model is designed to be adaptive to a range of body morphologies. Shown is a manually digitized human subject. The elliptical shapes are based on the counters of the body and adapt to a range of body morphologies [160].*

In recent years, the ECM model has been used to estimate the BSIP of pregnant women (Figure 30), a poorly represented population in the biomechanical field. The versatility of the ECM model offers the possibility of estimating BSIPs, without a great deal of training from the operator or researcher [162]. A more rigorous model than Hatze [163] presented a geometric model that required 242 anthropometric inputs by dividing the body into 17 segments. The model used gender-dependent density values and did not assume segment symmetry. Hatze used the same body segments as Hanavan [158] but modified the shoulder, trunk and buttock segments to more accurately describe these positions.

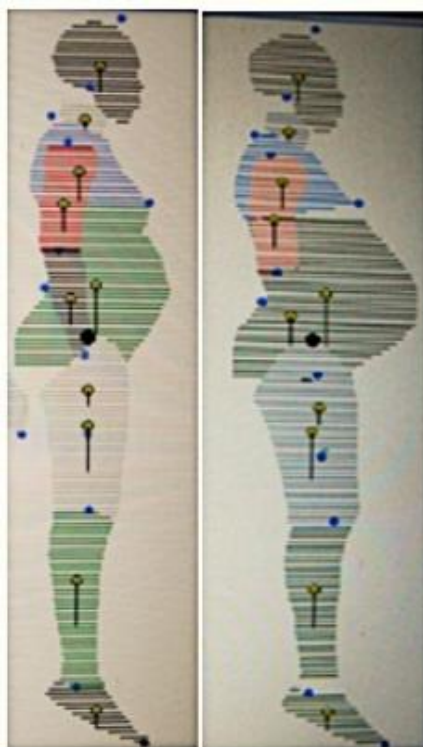


*Figure 30 : Image shows early pregnancy (left) and late pregnancy (right) with the abdomen region significantly increased in size. The ECM is adapted to estimate BSIPs (Yessoufou et al., 2014).*

Although Hatze's model is mathematically rigorous, most calculations can be programmed, and only the 242 anthropometric input parameters are needed to evaluate numerical solutions. An essential aspect of the model is that no assumptions are made about the coronal symmetry of the abdominal pelvic or abdominal-thoracic segments. As a result, any severe non-symmetry in regions such as the breast or large stomach is considered in the parameters, allowing for customization. This robustness allowed the modelling of subjects with more prominent features in the torso and abdomen regions, allowing for highly personalized subject-specific estimates [163]. Hatze's model reports the lowest error between measured and predicted total body mass (error <0.5%), but has rarely been used by researchers, possibly due to the 242 measurement inputs [164]. Figure 31 shows the model and a computerized version proposed by Robertson [164], which has not yet been evaluated in detail. Yeadon [165] proposed a geometric model consisting of 20 body segments and requiring 95 anthropometric inputs for evaluation. Yeadon argued that using ellipses to shape the body is done because it is mathematically convenient. Yeadon proposed solid stadium shapes, a mixture of rectangles and semicircles, to shape the body segments accurately. The Yeadon model estimated total body mass with a maximum error of about 3% [165]. Yeadon commented that this error is sufficient due to the reduced

measurement time of 30-40 minutes compared to Hatze's 90+ minutes (1980). In both Hatze's (1980) and Yeadon's models, the cumbersome demand for 95-242 anthropometric measurement inputs is problematic.

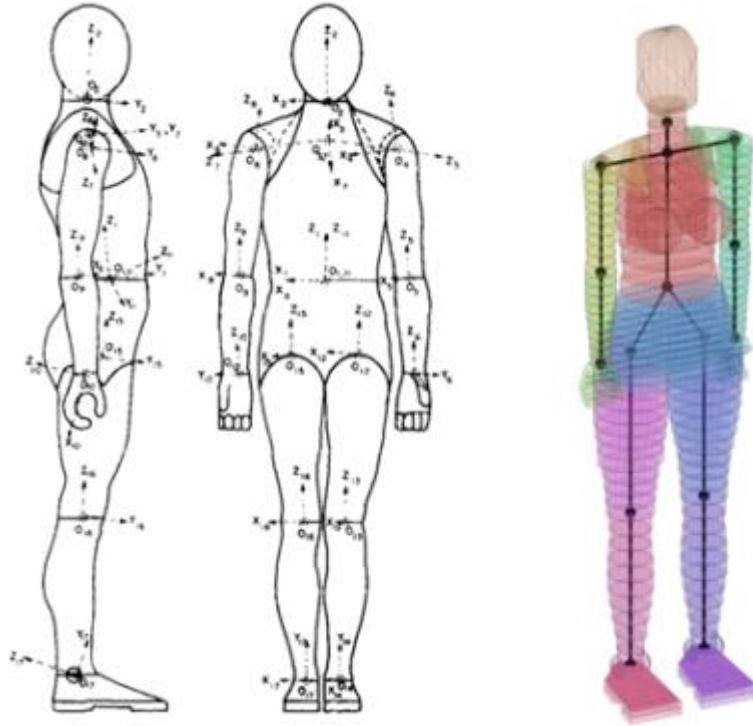


Figure 31: Left Side: The model presented by Hatze requiring 242 measurements of the body to be taken Right Side: A proposed computerized model of Hatze's (1980) model. [163],[164]

Time requirements and the association of errors with anthropometric measurements are some of the inconvenient demands of these techniques. 30 Geometric models present a method for estimating BSIPs. The input parameters for mathematical models can be easily manipulated thanks to the adjustability. For example, tissue density and anthropometric measurement inputs are under the operator's control; however, this requires assumptions about density values. The input density data in the models already mentioned were based on Dempster (1955) and Chandler et al. (1975). However, the density values can be used from other sources, such as medical imaging. A limitation of mathematical models is that they will only be accurate to the extent that they model physical morphology. Other limitations, such as manual measurement requirements and assumptions about the segment's shape, also need to be considered.

**PART II**  
**EXPERIMENTAL ACTIVITIES**

## **4. WORKFLOW**

Thanks to the development of additive manufacturing techniques, prosthetic surgery has reached increasingly advanced levels, revolutionizing the clinical course of patients with joint arthritis, rheumatoid arthritis, post-traumatic arthrosis, and congenital dysplasia. 3D printing has made it possible to obtain customized prostheses according to the use [166] on the needs of patients, using high-performance materials such as 316L stainless steel or Ti-6Al-4V [167], [168]. However, wear is caused by regular gait activities such as walking, sitting, or running, leading to the deterioration of the material used in the joint [169]. Friction and wear in hip prostheses are topics studied by many authors [170], [171]. Shankar et al. [172] investigated the tribological behavior of zirconia-hardened alumina (ZTA) versus titanium alloy (Ti-6Al-4V). The use of traditional materials has been gradually replaced using more performing materials [80–82] which has made it possible to obtain customized devices for the needs of patients and, therefore, more effective. Moreover, to guarantee a longer life cycle of the prosthesis and appropriate lubrication, the application of nanostructured coatings and surface processing was studied [83–86], such as the surface laser texturing technique already widely used in other industrial sectors [180], [181]. Numerical techniques have recently been adopted, such as the Finite Element Method (FEM), which, supporting the experimentation, allows the calculation of the useful life and the optimization of the functionality of the prostheses [182], allowing to precisely evaluate the distribution of the load on the prosthesis. The purpose of the following paper is the development of an algorithm that optimizes the hip prosthesis from the mechanical point of view using a machine-learning algorithm coupled with multi-body and finite element method simulations. The innovative aspect is represented using:

- Artificial intelligence to evaluate human kinematic,
- A humanoid model in the ADAMS® environment
- FEM model, which allows the prosthesis's optimization, suggests the best geometry.

## PART II

### Experimental activities

For optimizing the prosthesis, walking was chosen as the movement, as an act characterizes the great frequency in daily activities. It turns out to be a complex phenomenon that involves many components. As in humans, most of the musculoskeletal and nervous systems participate in walking. The forces and torques exchanged by the lower limbs during walking are transmitted through the joints, ligaments, and muscles to the trunk. The accelerations generated by the movement of upper limbs and, to the extent permitted by vertebral joints and the trunk, generate forces of inertia capable of balancing the body and combining with those generated by the lower limbs to generate the desired movement[183], [184]. Once the type of movement to be analysed has been defined, the algorithm to optimize hip replacement was defined. The algorithm consists of 5 steps, described in the Figure 32.

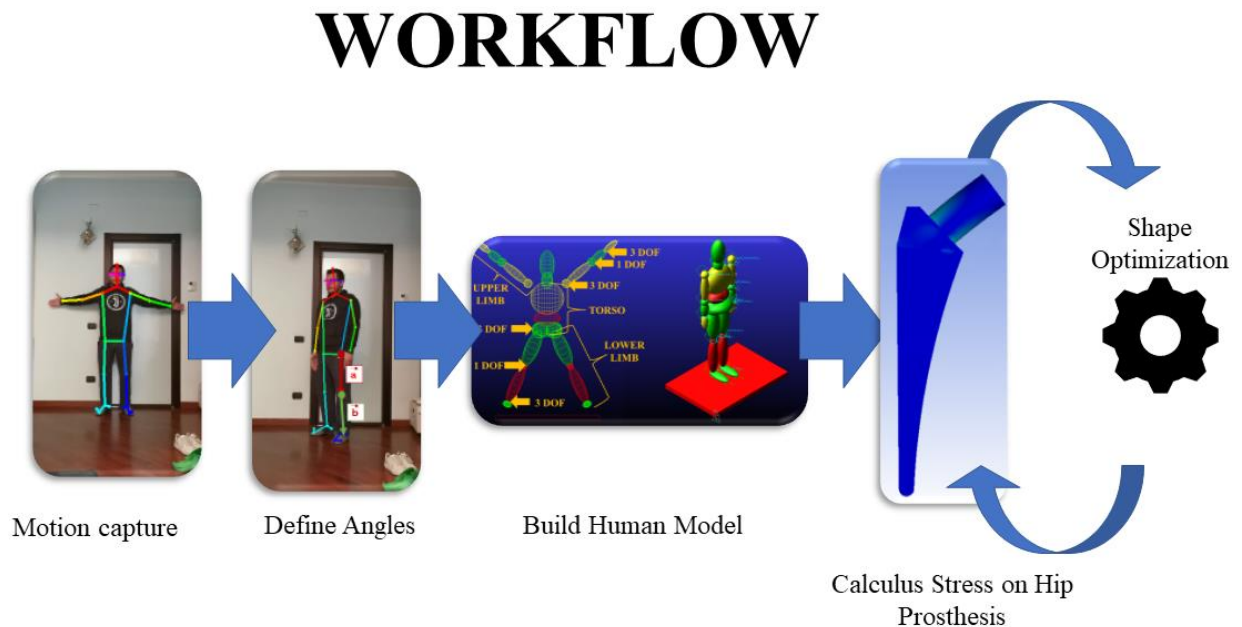


Figure 32: Simulation's steps.

The five steps for the realization of this optimization consist of:

- 1) Motion capture: capturing the subject's pose during movement
- 2) Extraction of the joint angles: extraction of the joint angles, of the positions of the markers that represent the joints between the various joints
- 3) Creation of humanoid model: the creation of a parametric multibody model having the dimensions and weight distribution of the subject under analysis

## *PART II*

### *Experimental activities*

- 4) Fem analysis of the prosthesis: calculation of the stresses acting on the prosthesis based on the loads to which the hip joint is subjected
- 5) Optimization of results: shape optimization algorithm based on the gradient descent method.

#### **4.1. First step – Motion Capture**

In the two-dimensional acquisition of the human pose, the problem of locating key anatomical points or "parts" has been concentrated on the search for parts of the human body[92–101]. Human pose estimation is the process of inferring human poses from a digital image. Pose estimation requires highly accurate detection and identification of human joints. Pose estimation algorithms follow a top-down or bottom-up approach. The execution time of these top-down approaches [102–108] is proportional to the number of people: for each survey, a pose estimator is performed for a one-person, and the more people there are, the higher the computational cost. Conversely, bottom-up approaches are interesting in that they offer solidity to early engagement and have the potential to decouple the complexity of the runtime from the number of people in the image. However, bottom-up approaches do not directly use global contextual cues from other parts of the body and other people. In practice, the previous bottom-up methods [202], [203] do not preserve the efficiency gains since the final analysis requires a costly global inference. One model was evaluated to define the subject's pose while walking, OpenPose.[111–113] It is a bottom-up real-time multi-person human pose detection library that detects the human body, foot, hand, and facial key points on single images. It can detect 135 vital body points from a digital image. The innovative tense is that no markers are needed. A single CNN is used for both key-point detection and association.

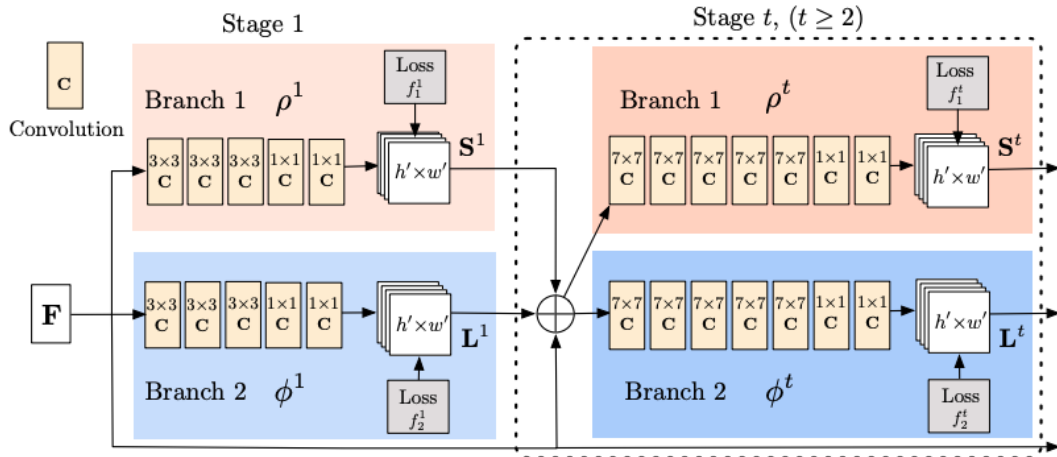


Figure 33: Architecture of the two-branch multi-stage CNN. Each stage in the first branch predicts confidence maps  $S^t$ , and each stage in the second branch predicts PAFs  $L^t$ . After each stage, the predictions from the two branches, along with the image features, are concatenated for next stage[205].

When key points are detected, a numerical score between 0 and 1 is assigned. It is a measure of the overall confidence in the key points estimated. OpenPose has been trained to produce three different pose models. The difference is represented by the number of points identified:

- 1) MPI can estimate a total of 15 key-points
- b) COCO can estimate a total of 18 points
- c) BODY\_25 can estimate a total of 25 points.

The most exhaustive pose model is the third. In addition to the key points estimated by MPI and COCO models, it contains descriptors for the feet and pelvic centre. Exist also a new and experimental model of OpenPose that is named body\_25b(Figure 34). As reported in [207], [208], This model has the highest accuracy parameters, which is more accurate than the default body\_25 and reduces the number of false positives. The keypoint definition differs from MPII for the evaluation of head and neck keypoints and removes the neck and middle hip keypoint of the body\_25 model.

*PART II*  
*Experimental activities*

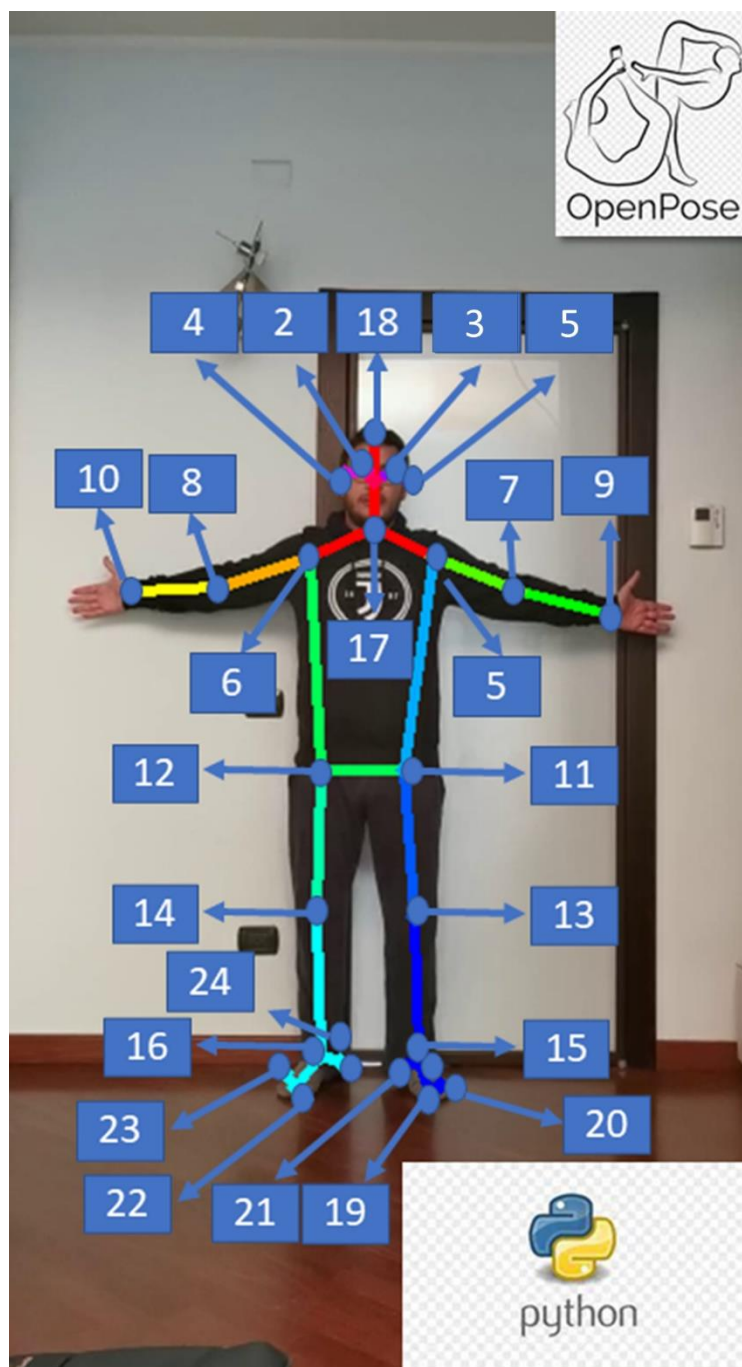


*Figure 34: The experimental body\_25b OpenPose.*

The first step implemented was classifying all the points captured by the algorithm. As in the Figure 34, it can be seen that the algorithm is capable of identifying 25 points. The subject's movement was captured with an action camera placed in front of the subject. The characteristics of the camera are shown in the Table 1.

## PART II

### Experimental activities

Table 1: Technical characteristics.

---

Camera Technical Features	
Resolution	4K(30fps), 2.7K(30fps), 1080P(60/30fps), 720P(120fps)
Pixel	20MP, 16MP, 12MP, 8MP, 5MP
Dimensions	5.9 x 2.5 x 4 cm; 60 g

---

Once the camera was placed in front of the subject, a rehearsal session was started. The next step was to start the algorithm to superimpose the skeleton on the subject, as shown in the Figure 34.

#### 4.2. Second step – Giant analysis and angle extrapolation

The subject was positioned in front of the camera in an upright position. The subject was placed at 90 cm from the camera lens. The initial pose of the subject was defined with an angle of 180 between the trunk and leg. A video of his movement was recorded. The subject performed the walking exercise sequentially. Openpose extrapolated the pose. As in [209] the knee angle was calculated using the vector dot product.

$$\theta = \cos^{-1} \left( \frac{\vec{a} \cdot \vec{b}}{|\vec{a}| |\vec{b}|} \right) \quad (71)$$

Two vectors were constructed from the hip, knee, and ankle coordinates obtained from the pose data. The first vector was formed with the hip and knee joint, while the knee and ankle

## PART II

### Experimental activities

joint formed the second one. The same things were done to evaluate hip angle. The following equation gives the knee angle ( $\theta$ ).

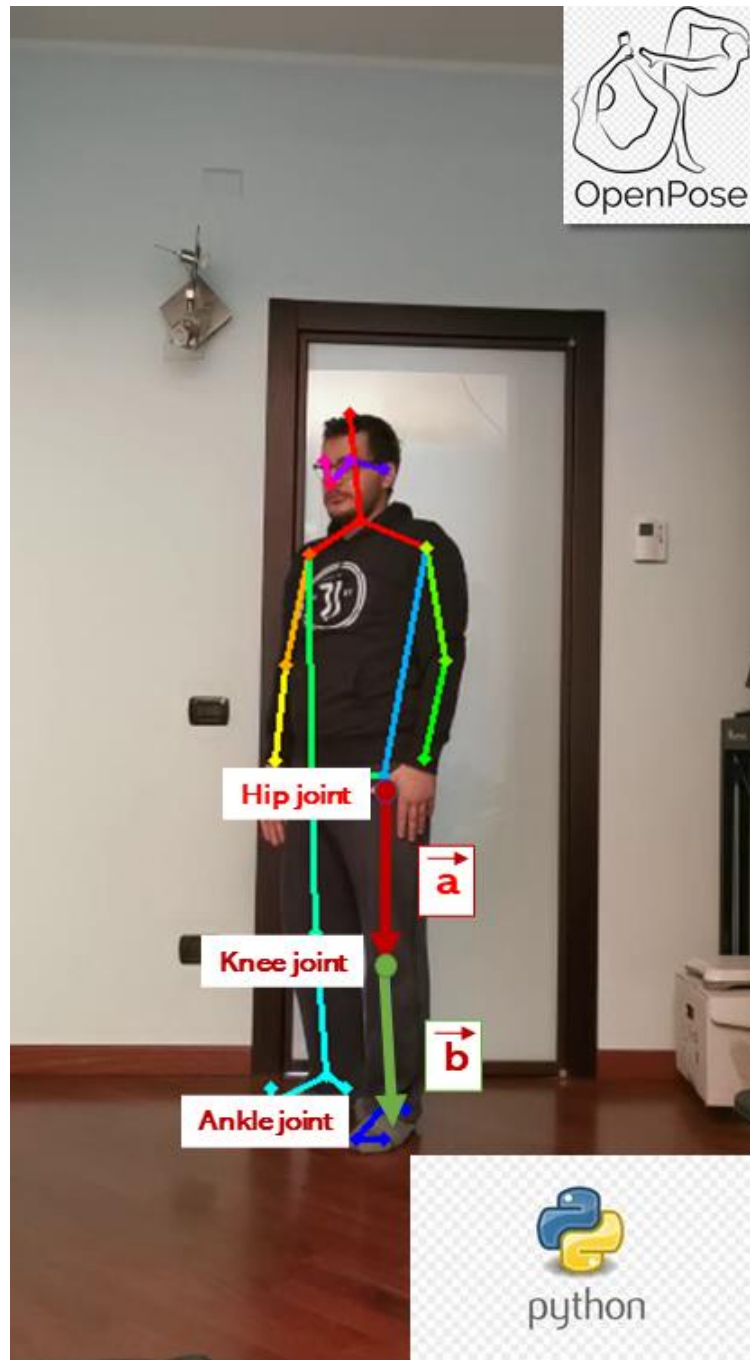


Figure 35: Angle measurements from video frame. [210]

Two vectors were constructed from the hip, knee, and ankle coordinates obtained from the pose data. The first vector was formed with the hip and knee joint, while the knee and ankle joint formed the second one. [210]

PART II

Experimental activities

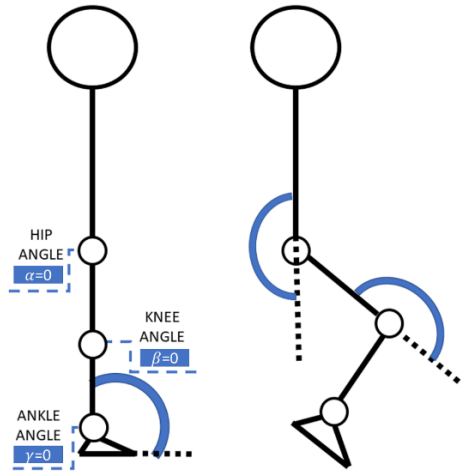


Figure 36: Definition of the joint angles, the hip angle created between trunk and thigh is identified by  $\alpha$ ; the knee angle between thigh and shank is identified with  $\beta$ ; finally, the ankle angle between shank and foot is identified with  $\gamma$ .

Once the vectors have been created, the angles have been redefined as in [211]. The initial pose of the subject provides that the articular angles are all zero; from that moment on, the movements can be calculated as a function of them. After the extrapolation of the angles from the frames, the laws of motion were created in MSC Adams. By way of example, Figure 37 shows values that will be attributed to joint rotations in order to move the human model in MSC Adams environment.

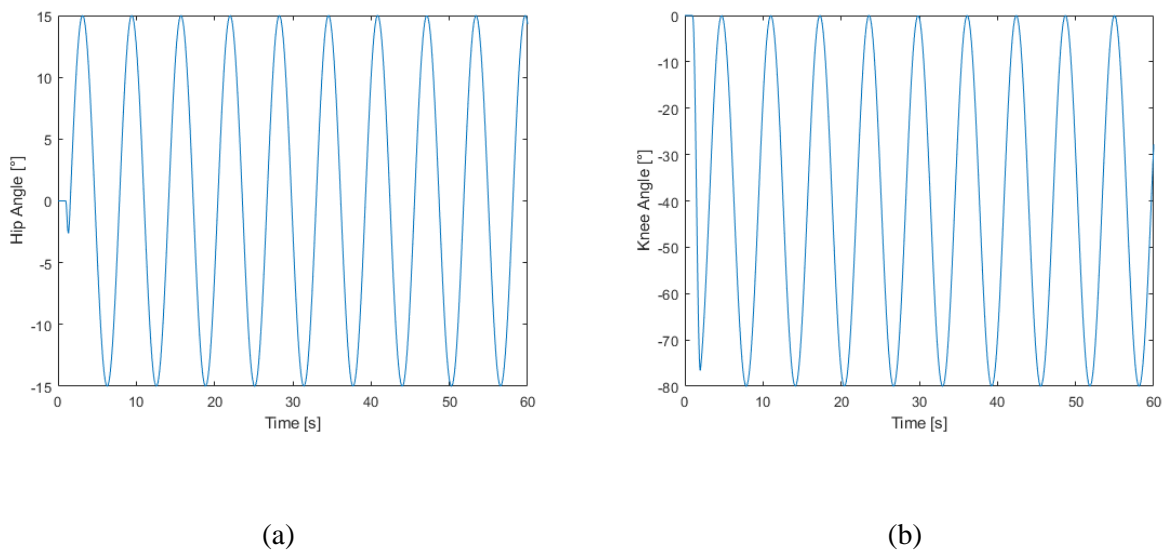


Figure 37: output from motion capture. a) Hip angle variation during the time; b) Knee angle variation during the time.

### **4.3. Third step – Human multi-body system**

The development of virtual human models has grown with the need to understand the biomechanical nature of movements to understand the consequences that affect comfort. [119–122]. Simulation techniques such as the multibody study the movement of the whole body since they consider it a set of joints connected by joints. Multibody simulations [216] find an excellent application in sports biomechanics [217]. On this basis, the definition of the dynamic equation of human movement and the acquisition of the dynamic parameters of human action constitute the critical steps in the theoretical analysis of the biomechanics of movement.

The purpose of the following paper led to the creation of a human multibody model in ADAMS® environment, because this software is the most used software in the world for multibody dynamics supports engineers in studying the dynamics of moving parts and analysing the distribution of forces and loads through mechanical systems. This model has been divided into three major macro areas.

- Upper limbs: Left / Right Upper arm, Left / Right Forearm, Left / Right Hand.
- Torso: Pelvis, Abdomen, Thorax.
- Lower limbs: Left / Right Thigh, Left / Right Shank, Left / Right Foot.

As reported in [143], the global reference system has been set up on the ground with the lines described in the Figure 38.

*PART II*  
*Experimental activities*

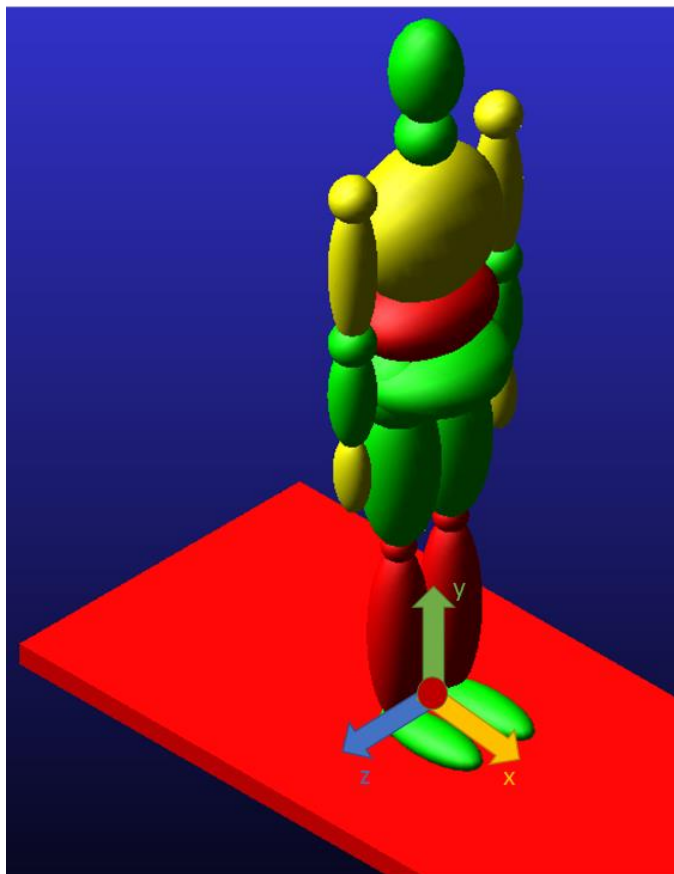
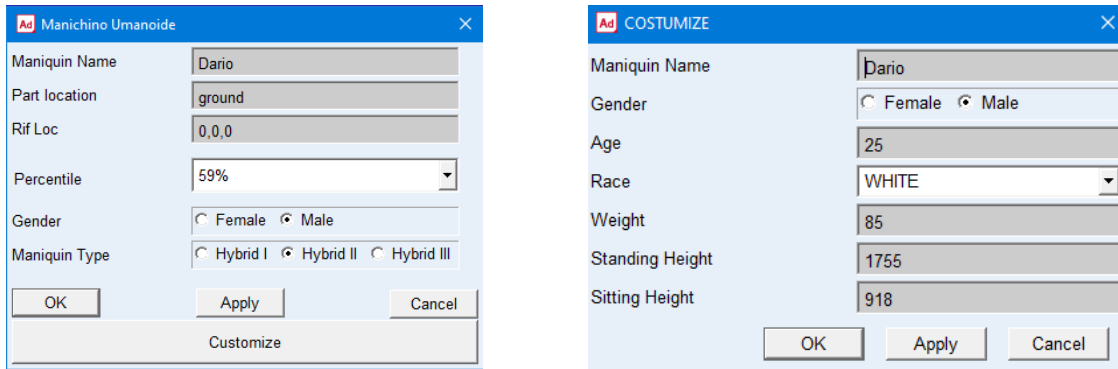


*Figure 38: Global coordinate system.*

### **4.3.1. Mannequins dialog boxes**

The author has set up the system in such a way as to be able to decide whether to analyse subjects defined by human percentiles or on specific subjects. For this reason, two separate dialog boxes have been created, representing respectively in Figure 39a, the option for creating humanoids has been created according to the human percentile, race, sex and number of parts with which they are composed. In contrast, in Figure 39b, it can be seen that the creation of the mannequin has been delegated to specific measures such as the weight, height of the subject and seated height.

*PART II*  
*Experimental activities*



(a)

(b)

*Figure 39: dialog box with anthropometric measures(a), dialog box for a specific subject (b)*

Particular attention was paid to manipulating the subject's posture since the humanoid must make up for different analyses. Therefore, it must be able to be customized both in terms of dimensions to simulate any subject, its positions, and orientations for each joint, to put it with the initial conditions most suitable for the analysis. An example of the potential of the human model created is described in Figure 40. In this case, the mannequin, thanks to the equations that define the range of movement, can be positioned within models, such as the car or motorcycle, and finally define the system's dynamics.

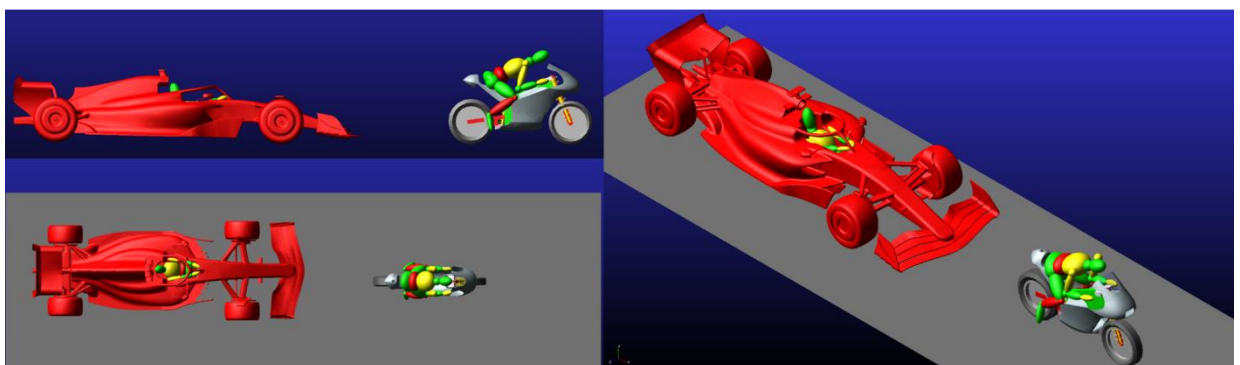


*Figure 40: examples of human posture*

Lastly, Figure 41 shows the dialog box relating to the customization of the angles of the humanoid joints.

*PART II*  
*Experimental activities*

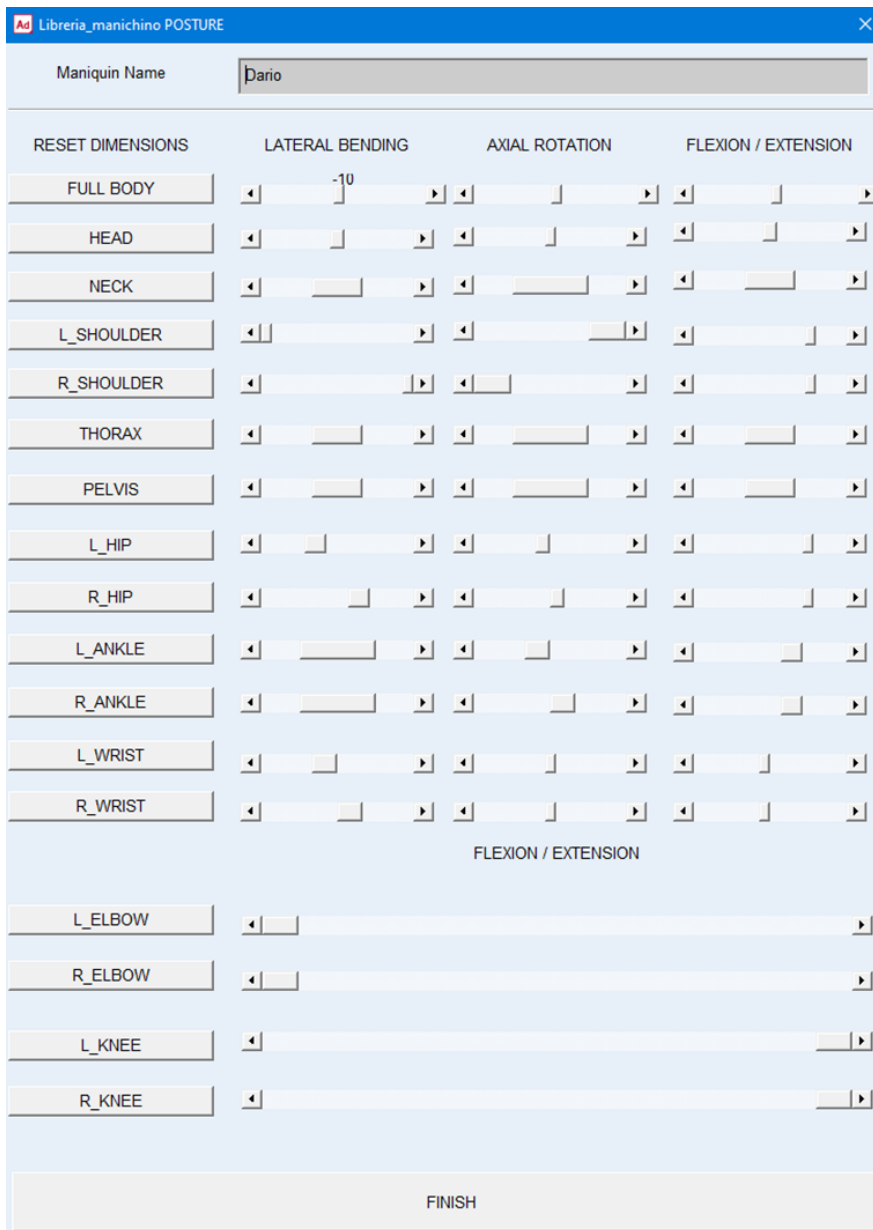


*Figure 41: dialog box for parametric joint orientation.*

Figure 41 shows the dialog box relating to the posture of the subject. As reported in [218]–[220], the limits of static movement that can be performed with the model have been defined. Once created, all this was generated to position the model in the position representing the instant 0 of the analysis. The rotation limits of each joint have been entered since they are helpful in the static phase for positioning the manikin, while in the dynamic phase of the movement, they represent the maximum rotation obtainable from a given joint.

### 4.3.2. Type and orientation of Joint

The term joint refers to the contact area between adjacent bones and the set of organs and tissues that may be present and which influence, allow or prevent the relative movement between the bones. Among the joints those that allow movements are diarthrosis. Regarding the movement of the upper limb, the movement of the shoulder, arm, forearm, and wrist can be distinguished. In particular, the shoulder allows an ante-retroposition movement, i.e. rotation around an axis parallel to the frontal plane and the raising-lowering movement of the shoulder. As for the arm, abduction-adduction, flexion-extension and finally, internal-external rotation are identifiable. The movements allowed for the forearm are flexion-extension and pronation-supination of the hand. Finally, abduction-adduction and flexion-extension movements are identified at the wrist. Seven DOFs can be identified for the upper limb, 3 in the shoulder, 1 (2) in the elbow and 2 (3) in the wrist. Wrist and elbow share pronosupination movements; depending on the analysis, a degree of freedom can be attributed to one and taken away from the other [221], [222]. In the proposed humanoid model, it was decided to proceed as shown in the Figure 42

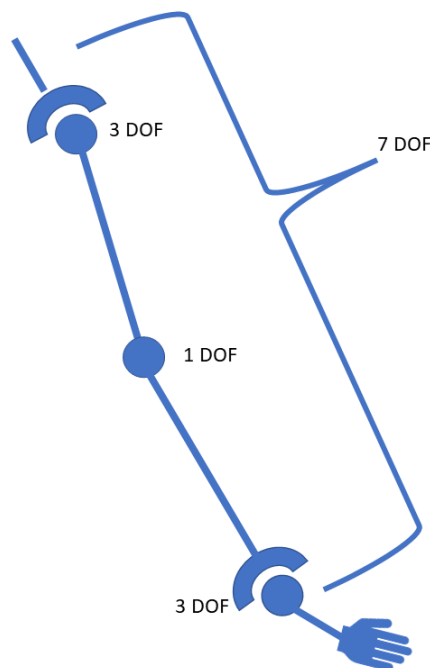


*Figure 42: kinematic schematic of the upper limb.*

## PART II

### Experimental activities

As for the lower limb, the elements that make it up are all the joints starting from the coxo-femoral. The included joints are the thigh, leg, and foot. From the point of view of the movement, the hip allows flexion/extension of the thigh, abduction/adduction of the leg and internal/external rotation of the femur. In the knee, the flexion of the leg itself and the extension that aligns the thigh and leg are allowed. Finally, the ankle allows flexion-extension, eversion, and inversion and finally, internal, and external rotation. Also, in this case, there are seven overall degrees of freedom (Figure 43).

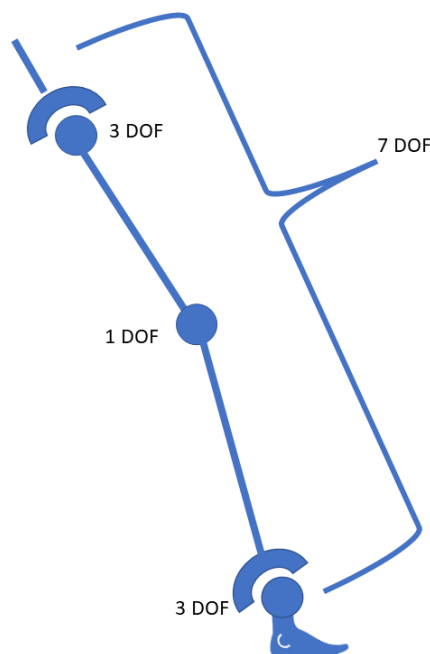


Figure 43: kinematic schematic of the lower limb.

As shown in the Figure 44 Each part was connected to another by a spherical joint. Each human segment has 3 DOF. Two knee and elbow joint rotations were locked. Contact with the ground and left and right feet were created.

## PART II

### Experimental activities

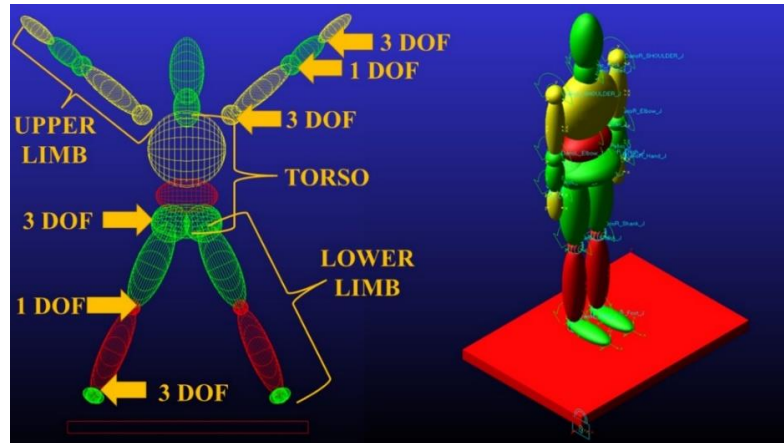


Figure 44: Dummy model.

The ISB (International Society of Biomechanics) standards has been used to define the coordinate systems for each joint [143], [223], [224] .

#### 4.3.3. Body dimension selection

The parametric model of humanoid, as reported in [225] is made up of 32 dimensions listed in Table 2. The model, as described above, provides for the selection of two macro types of humanoids.

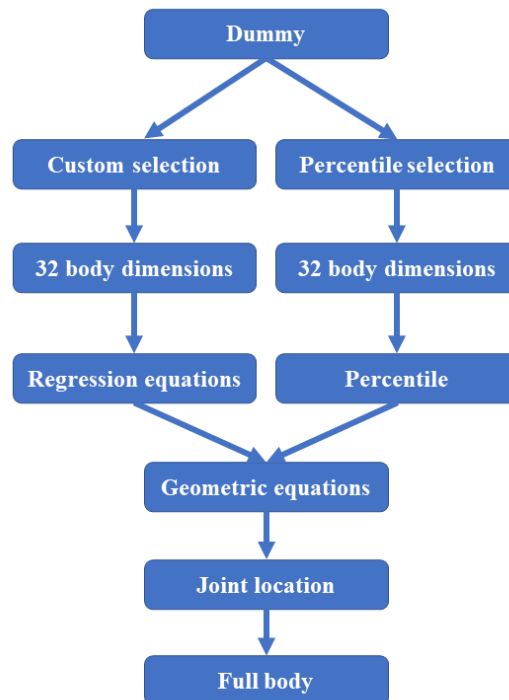


Figure 45: Body selection scheme.

## PART II

### *Experimental activities*

The first, called "custom selection", provides that, as shown in the Figure 45, the characteristic dimensions of the manikin (Table 2) are defined by regression lines. In the second case, all 32 dimensions are known as they represent human percentiles.

*Table 2: Body Dimensions.*

<b>Reference Number</b>	<b>Dimension</b>	<b>Reference Number</b>	<b>Dimension</b>
0	Weight	16	Hip Breadth, Standing
1	Standing Height	17	Shoulder to Elbow Length
2	Shoulder Height	18	Forearm-Hand Length
3	Armpit Height	19	Biceps Circumference
4	Waist Height	20	Elbow Circumference
5	Seated Height	21	Forearm Circumference
6	Head Length	22	Waist Circumference
7	Head Breadth	23	Knee Height, Seated
8	Head to Chin Height	24	Thigh Circumference
9	Neck Circumference	25	Upper Leg Circumference
10	Shoulder Breadth	26	Knee Circumference
11	Chest Depth	27	Calf Circumference
12	Chest Breadth	28	Ankle Circumference
13	Waist Depth	29	Ankle Height, Outside
14	Waist Breadth	30	Foot Breadth
15	Buttock Depth	31	Foot Length

The dimensions in both cases were retrieved from the ANSUR II database [226], the 2012 US Army Anthropometric Survey. As for the creation of the mannequin with human percentiles, the 32 dimensions come from the calculation of the percentiles. For the custom manikin, tests were performed to evaluate that the data follow a Gauss distribution (Normal). In this case, there were made two tests:

*PART II*  
*Experimental activities*

- Graphical Test: These are methods for plotting data and qualitatively assessing whether the data looks Gaussian.
- Statistical Test: These methods calculate statistics on the data and quantify the probability that the data was extracted from a Gaussian distribution.

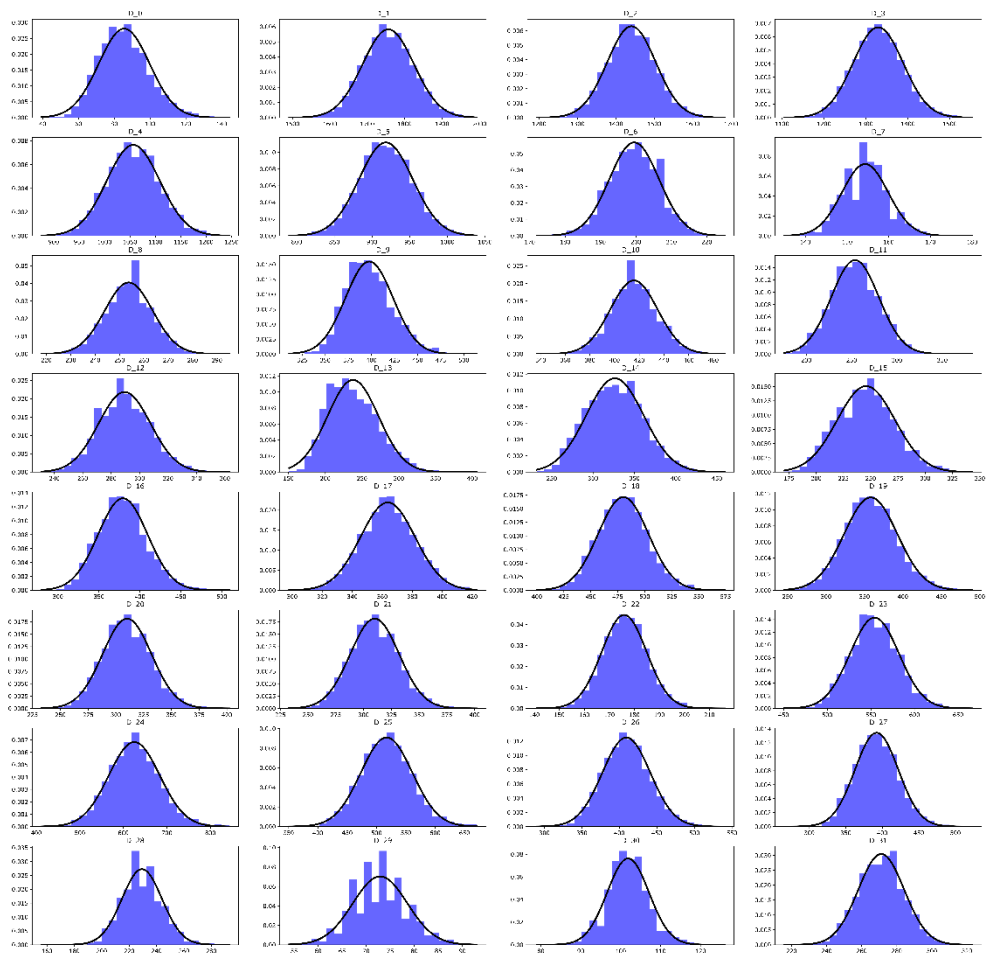


*Figure 46: Histogram plot of body dimensions.*

## PART II

### *Experimental activities*

The histogram is a simple and commonly used plot to check the distribution of a sample of data quickly. The histogram divides the data into a pre-specified number of groups called bins. The plot shows the bins across the x-axis maintaining their ordinal relationship and the count in each bin on the y-axis.

From a first visual inspection, the data were arranged according to a normal distribution (Figure 46). Once the first graphic inspection was done, it was decided to proceed with a statistical test as it is more relevant to the study.

The method used was  $\kappa^2$ . In statistics, D'Agostino's [227], [228] test is a way to measure departure from normality. The test aims to establish whether the given sample comes from a normally distributed population. The test is based on transformations of the sample kurtosis and skewness.

- Skew is a quantification of how much a distribution is pushed left or right, a measure of asymmetry in the distribution.
- Kurtosis quantifies how much of the distribution is in the tail. It is a simple and commonly used statistical test for normality.

With an alpha of 5%, it was all dimensions passed the test, so it was possible to state that all parameters follow a normal distribution.

Established that the data follow a normal distribution, it was decided to do a correlation analysis between the dimensions considered. The results are plotted in the Figure 47. It can be said that there is a direct correlation between the data, so we proceeded to define the regression lines.

*PART II*  
*Experimental activities*

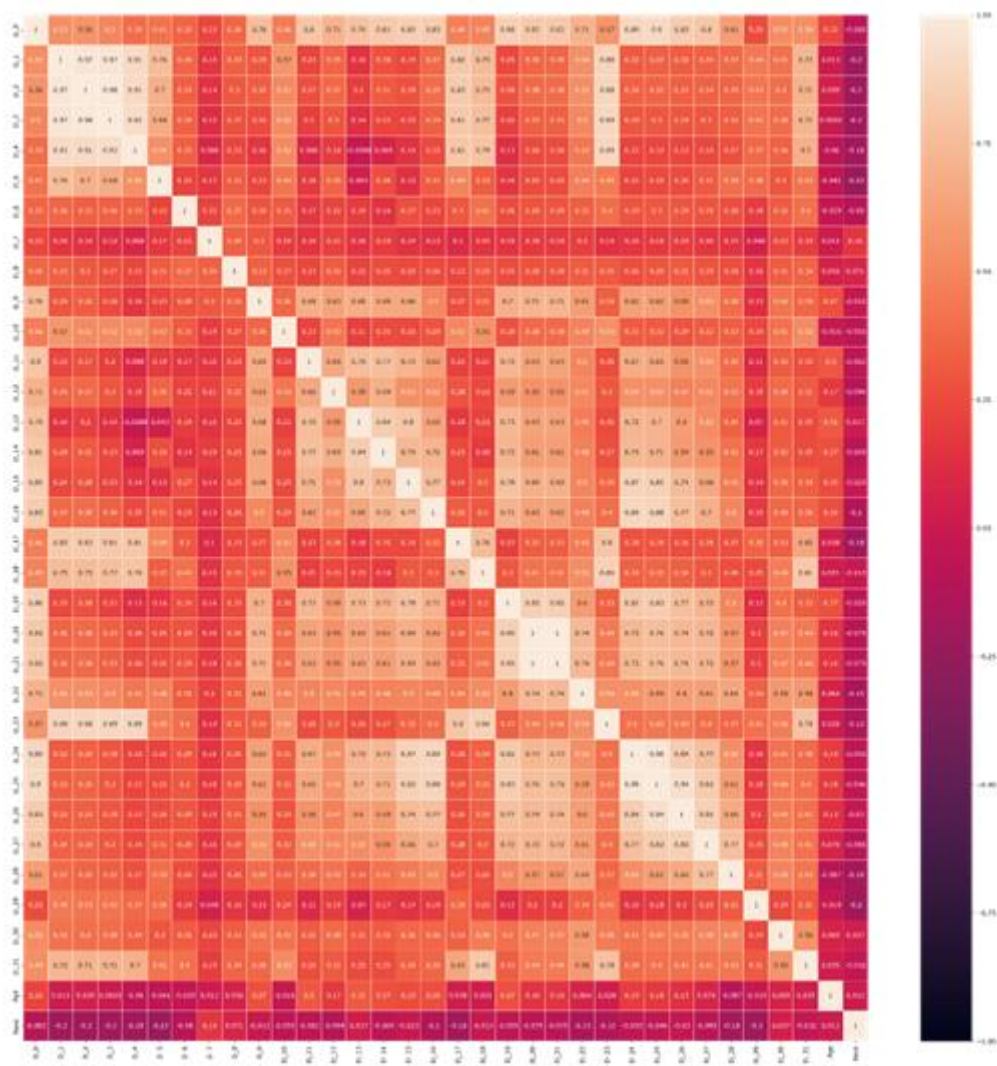


*Figure 47: Correlation matrix body dimensions.*

The parameters taken into consideration to generate the regression lines were:

- 1) Age ;
- 2) Gender;
- 3) Race;
- 4) D0 = Weight;
- 5) D5 = Seated Height;
- 6) D1 = Stature;

PART II

Experimental activities

Table 3: coefficients for human body parameters regression.

	D2	D3	D4	D6	D7	D8	D9	D10
intercept	-35,0752	-88,9414	-67,9392	139,1846	143,1841	-50,2432	349,0654	170,5202
Gender=1	-4,27851	-6,9721	-1,55094	2,329641	2,200917	4,642459	24,67028	14,23185
Gender=2	4,278509	6,9721	1,55094	-2,32964	-2,20092	-4,64246	-24,6703	-14,2318
DODRace=1	2,886842	0,642943	-1,06407	0,40566	-2,0637	-1,0486	1,096223	-2,94326
DODRace=2	-3,12681	1,173143	2,673628	3,797626	-1,06982	-4,97077	3,410271	3,645565
DODRace=3	2,819559	0,824092	-2,66458	-0,71443	-0,70767	-0,10966	1,144341	-0,50916
DODRace=4	0,1358	-1,2516	-3,80248	-4,00328	3,442317	5,25488	-1,88565	-0,01976
DODRace=5	3,653606	0,987634	-3,46435	-0,87705	-1,31647	-0,11059	4,368109	-2,3373
DODRace=6	0,543401	-0,17121	-1,19532	-2,29479	1,448188	2,465993	-2,21955	-1,12008
DODRace=8	-6,91239	-2,205	9,517183	3,686254	0,26715	-1,48125	-5,91374	3,284008
D1	0,961761	0,959749	0,948472	0,008091	-0,00987	0,03216	-0,08359	0,082181
D5	-0,27204	-0,27767	-0,53194	0,036056	0,017902	0,241609	0,033113	0,049896
Age	0,207609	0,020843	-0,42966	-0,04233	-0,0375	0,021484	0,263896	-0,13763
D0	0,382971	-0,08027	-0,43935	0,131941	0,146687	-0,05167	1,531549	0,543288
	D11	D12	D13	D14	D15	D16	D17	D18
intercept	270,8249	187,1619	300,2746	300,0636	235,5625	235,5625	20,97108	-12,8851
Gender=1	-8,03363	0,437929	0,558095	-3,74832	-18,7323	-18,7323	1,567949	-4,32025
Gender=2	8,033626	-0,43793	-0,55809	3,748316	18,73233	18,73233	-1,56795	4,320252
DODRace=1	3,130378	3,553167	5,54259	5,364772	1,741953	1,741953	-0,49389	1,283766
DODRace=2	-5,6795	-4,00538	-0,71357	-15,7674	-7,70292	-7,70292	-1,99274	-4,25511
DODRace=3	2,881168	3,058379	4,051204	4,4603	0,774624	0,774624	-1,27621	2,422319
DODRace=4	-0,93896	2,128051	0,295663	0,569265	-2,68698	-2,68698	-2,7644	2,621483
DODRace=5	6,728274	4,26936	5,647507	6,322115	-3,04108	-3,04108	-0,86677	5,09703
DODRace=6	-4,31745	-1,5694	-1,51684	1,068048	-1,37887	-1,37887	-2,00709	2,791252
DODRace=8	-1,80392	-7,43418	-13,3066	-2,01708	12,29327	12,29327	9,401099	-9,96074
D1	-0,04457	-0,00975	-0,09878	-0,07347	-0,02916	-0,02916	0,288175	-0,31413
D5	-0,11129	0,032895	-0,12748	-0,06649	0,046067	0,046067	-0,18221	0,833149
Age	0,359245	0,170009	0,680797	0,309605	0,020104	0,020104	0,05572	0,181823
D0	1,860624	0,951855	2,37097	2,444981	1,604672	1,604672	0,018717	0,49996
	D19	D20	D21	D22	D23	D24	D25	D26
intercept	58,99494	237,0901	1003,805	85,76155	21,85094	613,9906	339,3991	159,4887
Gender=1	5,652799	13,71748	-7,8856	5,306619	-0,40075	-21,5069	-11,6297	-0,7638
Gender=2	-5,6528	-13,7175	7,885604	-5,30662	0,400745	21,50691	11,62972	0,763798
DODRace=1	-1,92269	-1,68502	17,48515	-0,0968	-1,35741	-1,18089	-3,50796	0,814544
DODRace=2	-0,1498	4,952964	-27,8709	0,389397	1,618652	10,05841	1,529692	-1,82095
DODRace=3	-0,97957	-3,51971	16,15016	-1,3394	0,437177	-0,81797	-3,60727	-1,37594
DODRace=4	-0,66447	-4,28816	3,311566	-2,17919	-2,33762	-5,13557	1,114973	-1,0112
DODRace=5	-2,21701	-2,08291	20,83149	-1,23112	-2,46222	-11,2751	-5,03291	-0,09604
DODRace=6	-3,95651	-1,52185	0,147556	-0,41871	-0,84744	-1,06595	2,897605	0,031818
DODRace=8	9,890053	8,144687	-30,055	4,875824	4,948863	9,417041	6,60587	3,45778
D1	-0,03768	-0,04023	-0,27006	0,011924	0,497649	-0,21449	-0,10102	-0,01878
D5	0,080274	0,018511	-0,35618	0,032571	-0,3963	0,054767	0,077417	0,04886
Age	0,069382	0,000493	1,793394	0,016554	-0,04134	-0,67732	-0,26531	-0,36311
D0	0,429696	1,330543	7,97775	0,394273	0,287769	4,431975	2,31966	0,813644

*PART II*

*Experimental activities*

*Table 4: coefficients for human body parameters regression.*

	D27	D28	D29	D30	D31
intercept	343,3524	159,4887	14,13556	55,04734	53,30592
Gender=1	-4,37168	-0,7638	2,380362	2,03831	3,97116
Gender=2	4,371681	0,763798	-2,38036	-2,03831	-3,97116
DODRace=1	-1,0082	0,814544	0,833649	-1,32355	-2,00122
DODRace=2	-2,58204	-1,82095	-1,55921	0,318322	4,459381
DODRace=3	-5,43996	-1,37594	0,090156	-0,19662	0,553188
DODRace=4	5,757421	-1,0112	-1,28971	0,741282	-2,77116
DODRace=5	-5,16481	-0,09604	-0,73488	-0,46507	0,843705
DODRace=6	5,371055	0,031818	-0,19701	1,728862	2,181747
DODRace=8	3,066539	3,45778	2,856993	-0,80323	-3,26564
d1	-0,08758	-0,01878	0,034958	0,017484	0,142605
d5	0,048142	0,04886	-0,0125	0,001221	-0,05402
Age	-0,30639	-0,36311	0,006212	-0,04423	-0,07435
D0	2,030296	0,813644	0,070043	0,176949	0,186842

The equations that define the dimensions are defined as follows:

$$D_i = G + R + D_1x_1 + D_5x_2 + D_0x_3 + Age x_4 \quad (72)$$

Where  $D_i$  represents the dimension to be calculated,  $G$  represents the gender chosen for the analysis. As seen in the table, there are two choices for gender, male and female. The coefficient to be replaced in the equation changes depending on the choice.  $R$  represents the race. There are 8 different types of choices for the breed.  $x_1$  represents the  $D_1$  dimension entered by the user, which must be multiplied by the relative coefficient shown in the Table 3-Table 4. The same goes for the coefficients  $x_2$  (dimension  $D_5$ ),  $x_3$  (dimension  $D_0$ ) and  $x_4$  (age). The missing dimensions are obtained from the combination of the following variables, according to the parameters defined in (72).

The following analysis decided to evaluate the custom modelling based on a specific subject whose dimensions are shown in the Table 5.

*PART II*

*Experimental activities*

*Table 5: Subject dimension.*

---

Human characteristics	
Weight	85 kg
Standing Height	1755 mm
Seated Height	918 mm
Age	28

---

**4.3.4. Inertial parameters**

In the following paper, the mass properties have been calculated as:

$$m_s = p_s M \tag{73}$$

Where  $p_s$  is a percentage of the mass of the joint concerning the total mass  $M$ . The position of the centre of mass was calculated about a known reference system.

$$r_s = L_s \begin{pmatrix} c_s^X \\ c_s^Y \\ c_s^Z \end{pmatrix} \tag{74}$$

$c_s^X, c_s^Y, c_s^Z$  are the coordinates of the centre of mass expressed as a percentage of the length of the segment under examination  $L_s$ .

*PART II*  
*Experimental activities*

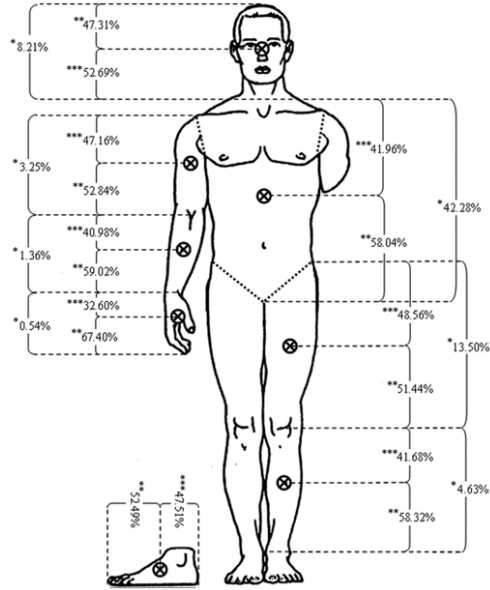


*Figure 48: An MRIBSP human model (\*, the ratio of the segment mass is expressed as a percentage of total body mass; \*\*, the percentage of segment length from the proximal end; \*\*\*, the percentage of segment length from the distal end). [229]*

The inertia matrix, on the other hand, is defined as:

$$r_s = m_s(L_s)^2 \begin{bmatrix} (r_s^{XX})^2 & (r_s^{XY})^2 & (r_s^{XZ})^2 \\ (r_s^{YY})^2 & (r_s^{YY})^2 & (r_s^{YZ})^2 \\ sym & & (r_s^{ZZ})^2 \end{bmatrix} \quad (75)$$

Where  $r_s^{XX}, r_s^{YY}, r_s^{ZZ}$  are the gyrating radii of inertia expressed as a percentage of the length of the segment. Figure 49 shows the positions of the reference points taken into consideration for calculating the length of the segments.

## PART II

### Experimental activities

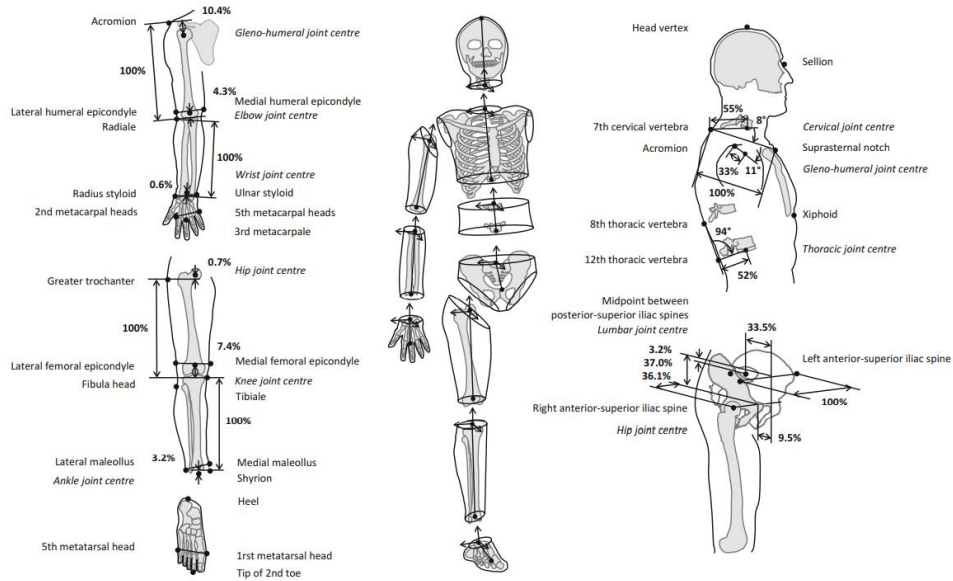


*Figure 49: Skin landmarks, joint centers estimated by regression equations, and body segments[230].*

#### 4.3.5. Multibody simulation output

Once the mannequin model has been defined, as reported previously, the state variables have been created. The set of variables represents the angle variation in the three components of the 25 points identified by the motion capture algorithm. As shown in Figure 50, the system's input is the neural network output. At the same time, the three components relating to the forces along the three axes of rotation of the spherical joint located in the hip are calculated at the output.

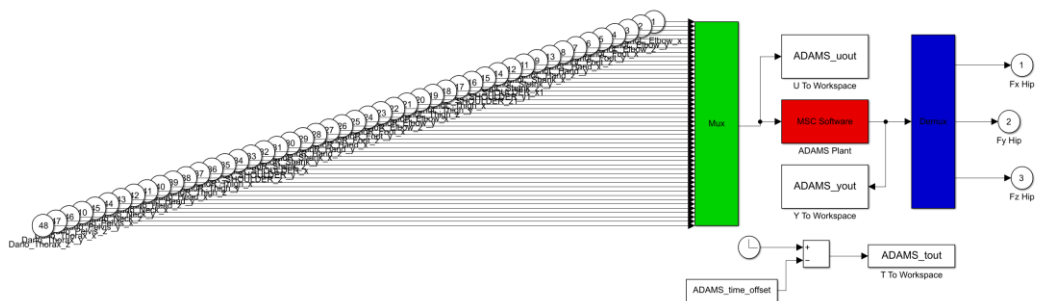


*Figure 50: Model for load calculus from the multibody system*

## PART II

### Experimental activities

The system receives the inputs from Openpose, instant by instant, it transfers the data on the angles reproduced by each joint, and the mannequin reproduces the movement (Figure 51)

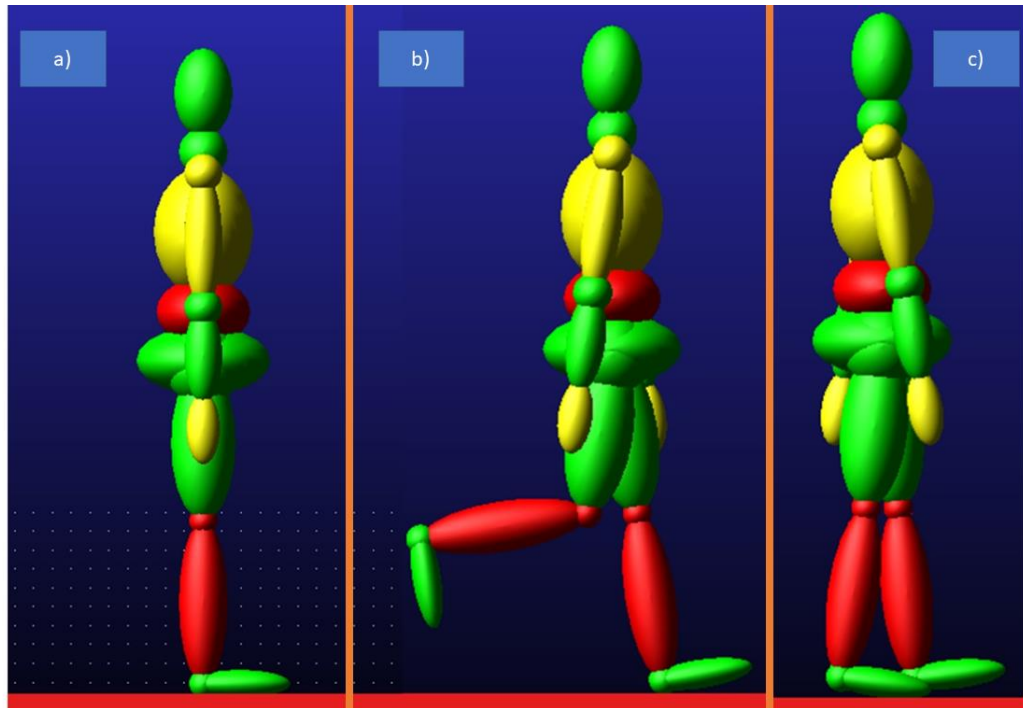


Figure 51: Dummy motion.

Figure 51 describes the walking cycle. At the instant of departure in which both feet are in support (Figure 51a), it can be seen in Figure 51b that the left foot is in stance position and the right foot in swing position, it is clear that the movement has begun. Finally, Figure 51c shows the cycle's end and the beginning of the next cycle. As described above, the characteristic parameters of walking were calculated.

Table 6: Gait parameters.

Gait Parameters	
$f_p$ Step frequencies [step/min]	18
$l_c$ Cycle length [m]	1.4

## PART II

### Experimental activities

From the parameters in Table 6, it is possible to calculate the walking speed, the cycle time and energy consumption. Speed and cycle time was calculated as follows:

$$v = \frac{l_p f_p}{60} = \frac{0.7 \times 18}{60} = 0,21 \text{ m/s} = 0.76 \text{ km/h} \quad (76)$$

$$t_p = 3,33 \text{ s} \quad (77)$$

$$t_c = 6,66 \text{ s} \quad (78)$$

Finally, the enegretium consumption was calculated as reported in [152]:

$$\dot{E}_w = 2.23 + 1.26v^2 = 2.23 + 1.26 \times 0,21 = 2,3 \frac{W}{kg} \quad (79)$$

The reaction forces due to the contact between the floor and the feet have been calculated. Finally, the forces acting on the hip are calculated (Figure 52) and then transferred to the fem model. The nine walking cycles within Figure 52 have been highlighted, equivalent to the 18 steps taken during the 60 s simulation. The data shown in Figure 52 represent the forces generated at the right hip joint.

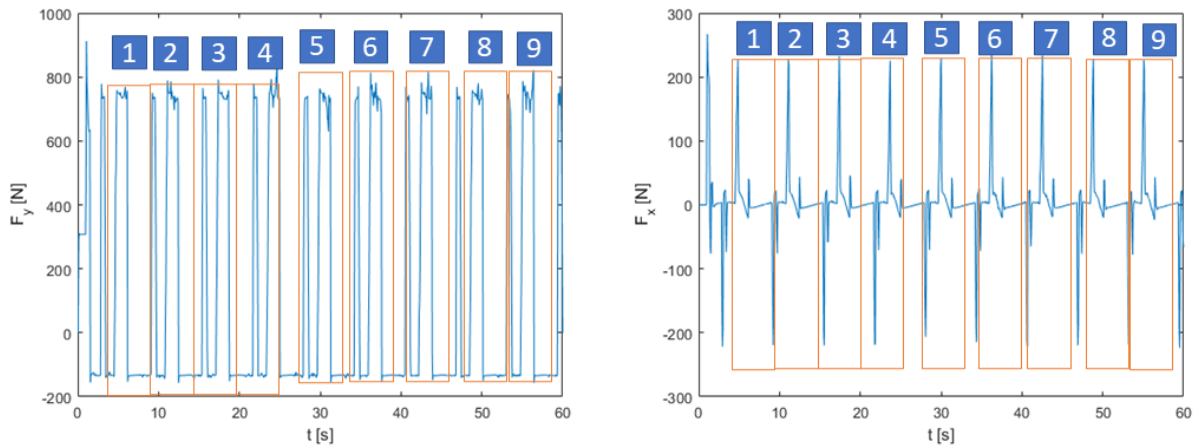


Figure 52: Forces applied on hip joint.

By Analyzing Figure 52, there are two phases considering a cycle of nine described. The first phase causes an increase of forces in x and y direction, and a sharp decrease in the same

*PART II*

*Experimental activities*

characterizes the second. During the first phase, there is an increase in the forces because the foot is in a stance position, so all the vertical load is discharged on the hip, while in the x direction, the increase in force is due to friction with the ground. While in the second, doing the vertical load acting on the hip is due only to the weight force since the leg is lifted off the ground.

**4.4. Fourth step – Fem Analysis**

The fourth phase is characterized by the structural analysis of the "hip prosthesis" component. This process was included in the workflow with the fifth step - optimization since the static type of analysis was set using the loads from the multibody model as input. The tested component is a hip prosthesis.

**4.4.1. Pre-processing – Loads and Constraints**

The prosthesis is of the parametric type as a succession of static analyzes were carried out in the workflow until the correct shape was obtained for the loads acting on the system. A sensitivity analysis was carried out based on the system's displacement values reproduced in the output. For this reason, the mesh was thickened until a displacement value equal to or less than 2% compared to the previous simulation was obtained. Figure 53 shows the outputs of this procedure. The mesh used for the geometry consists of tetrahedral (SOLID186) elements with a lower limit of 1 mm in size for the prosthesis. SOLID186 is a higher-order 3-D 20-node solid element that exhibits quadratic displacement behaviour. The element is defined by 20 nodes having three degrees of freedom per node: translations in the nodal x, y, and z directions. The mesh has been generated through the “MultiZone method” also, in this case, implemented in Ansys. It allows using hexahedral elements to have a smoother mesh to apply the load conditions.

*Table 7: Mesh properties*

---

Node	150,000
Elements	105,000

---

## PART II

### Experimental activities

Table 7 shows the average number of nodes and elements for analysis during the optimization process. It is considered an average number because, during each cycle, the geometry evolves and changes its size.

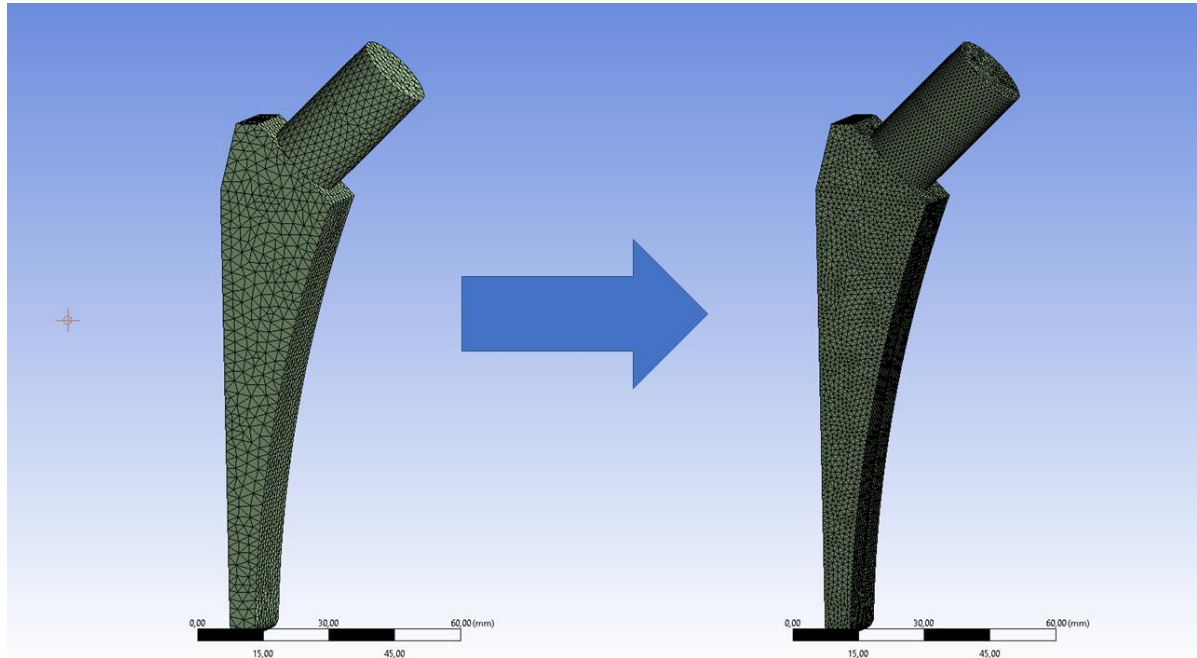


*Figure 53: Mesh sensitivity.*

As previously defined, the loads come from the multibody system. Schematically, the system was tested as follows:

- 1) Constraints: the constraint is of the fixed type, applied on the lower faces of the prosthesis.
- 2) Loads: concentrated load applied on the horizontal face of the prosthesis neck.

Figure 54 shows the diagram of the loads and constraints. The constraints are represented in blue, while the loads are secured according to their lines of action using a different colour for each axis.

*PART II*  
*Experimental activities*

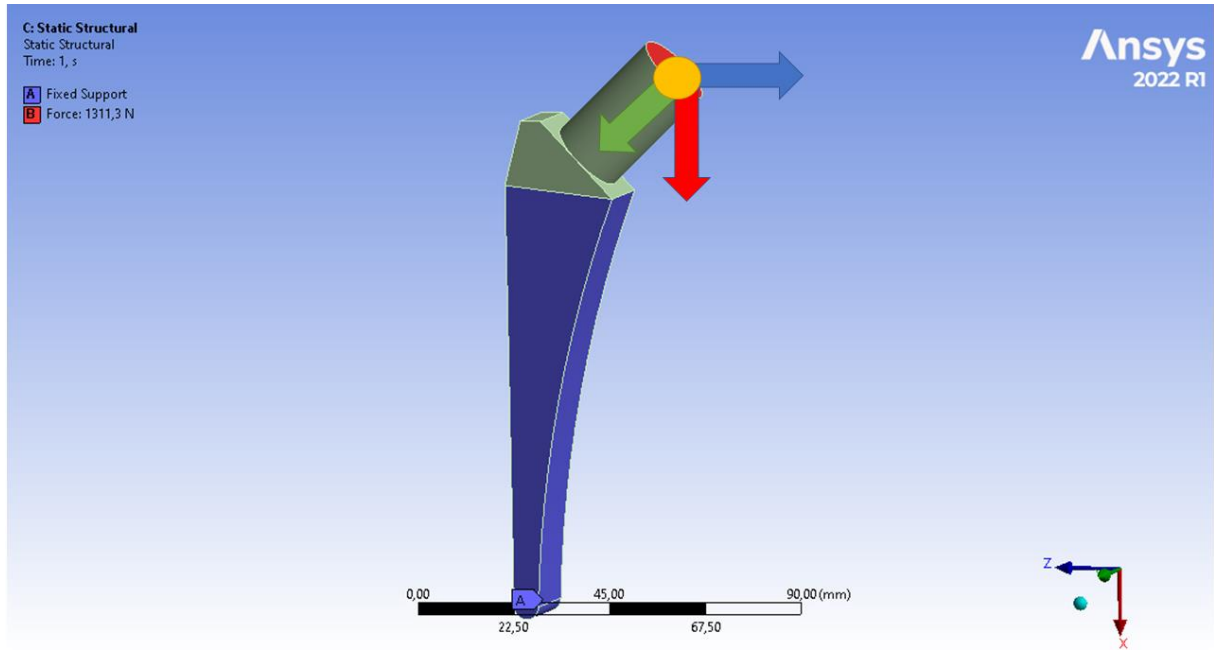


*Figure 54: Load and constraint of the system.*

#### **4.4.2. Pre-processing – Material selection**

For the choice of material, AISI 316 L was decided, a material studied in the literature to produce custom hip prostheses [231], [232]. Specimens were made, and the material was tested to obtain its properties. An analysis was also carried out using the static thermographic method. This approach returns limiting stress which represents the first damage to the material. It can be said that, during a static tensile test of common engineering materials, the temperature evolution detected employing an infrared camera is characterized by three phases (Figure 55). Firstly, an approximately linear decrease due to the thermoelastic effect (Phase I); therefore, the temperature deviates from linearity up to a minimum temperature value (Phase II), then undergoes a higher increase until the material fails (Phase III)[233], [234].

*PART II*  
*Experimental activities*

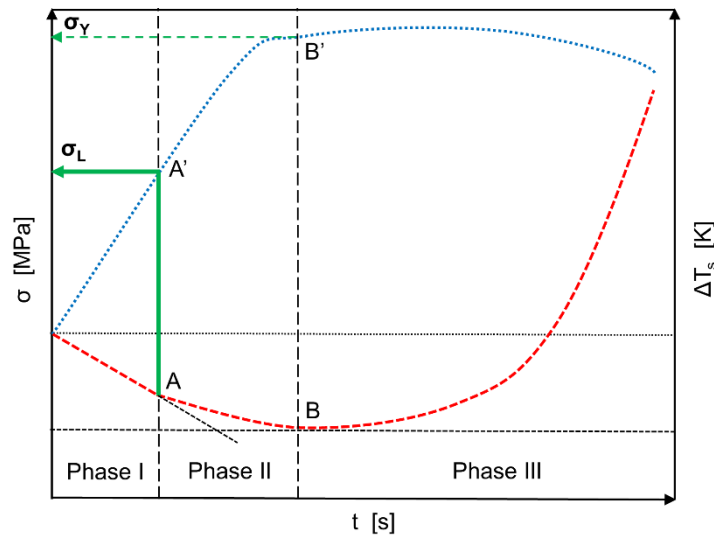


*Figure 55: Qualitative  $\Delta T_s$  trend vs machine time ( $t$ ) vs applied stress ( $\sigma$ )[235].*

Under uniaxial stress and adiabatic test conditions, Lord Kelvin's thermoelastic law can be simplified as:

$$\Delta T = K_m T_0 \sigma_m \tag{80}$$

here  $K_m$  is the thermoelastic coefficient ( $\text{Pa}^{-1}$ ),  $T_0$  is the initial specimen's temperature (K), and  $\sigma_m$  is the average stress in the specimen cross-section (MPa). Within the material, in the first phase (Phase I), where all the crystals are elastically stressed, the temperature trend follows the linear thermoelastic law; while, in the second phase (Phase II), some crystals are plastically deformed, and the temperature trend deviates from the linearity as the plastic deformations are more prevalent, in correspondence of the yielding stress of the material [233], [234], temperature increase up to failure. Important information derives from the fact that, if it is possible during a static test to estimate the stress related to the macroscopic damage at which the temperature trend loses the linearity characteristics, this stress could be correlated to a stress level that creates microscopic irreversible deformation. This critical stress is the same that, if applied cyclically to the material, will lead to fatigue failure.

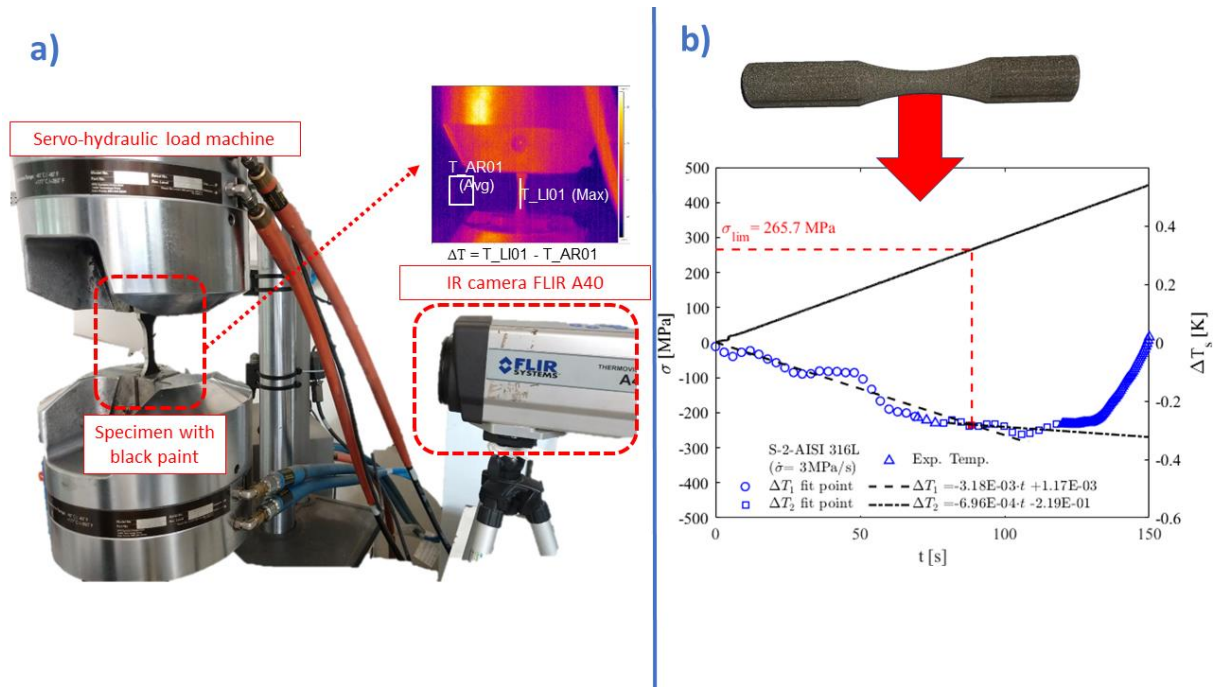


Figure 56: a) Experimental setup for STM, b) Qualitative  $\Delta T_s$  trend vs machine time ( $t$ ) vs applied stress ( $\sigma$ ) AISI 316 L

As shown in Figure 56a, the tests were conducted, under stress or displacement control, adopting a rate to assure adiabatic conditions during the tests, i.e. the specimen must not have the time to exchange heat with the surrounding environment. Under this hypothesis, as reported by Melvin and Lucia [233], [234], the “characteristic heat diffusion time” for the specimen is more and more less than the whole test time. Environmental conditions, such as room temperature, can severally affect the energy release of the material, allowing it to exchange heat with the surrounding environment by conduction and convection. All the static tensile test under consideration were performed at the mechanical laboratory of the University of Messina. The materials under study were stainless steel AISI 316L. The typical experimental setup requires a servo-hydraulic loading machine and an infrared camera (Figure 56a). For steel specimens, an INSTRON 8854 and an MTS 810, up to 250 kN of maximum load, were adopted. For plastic and composite material, an ITALSIGMA 25 kN servo-hydraulic load machine was adopted. The infrared camera FLIR A40 (thermal sensitivity of  $0.08^\circ\text{C}$  at  $30^\circ\text{C}$ ) with a sample rate of 1 image per second was adopted to monitor the surface of the specimen’s reduced section. The maximum temperature value has been recorded and filtered in MATLAB® with a *rlowess* filter with a data range of 5%. To enhance the thermal emissivity of the material up to 0.98, the specimen’s surface was covered with a black paint. Finally, the data were processed by creating the two adjustment lines that will identify the transition from

## PART II

### Experimental activities

linear to non-linear behaviour; their intersection, as already mentioned, defines the limit stress of the material (Figure 56b). The value of the limit stress determinate by STM on specimens change between  $\sigma_{lim\ ave} = 236 \pm 30 \text{ MPa}$ . The characteristics of the material used in the FEM are shown Table 8.

Table 8: AISI 316 L properties

Material Properties	
Density[kg/mm <sup>3</sup> ]	7954
Young Modulus [GPa]	195
Poisson Ratio	0,25
Bulk Modulus [GPa]	190
Shear Modulus [GPa]	78
Yeld Strength [MPa]	250
Tangent Modulus [MPa]	2091

### 4.5. Fifth step - Optimization Process

The creation of an optimization algorithm characterized the last part of the analysis. The algorithm in question is FMINCON, a function included in MATLAB's Optimization Toolbox, which seeks the minimizer of a scalar function of multiple variables within a region specified by linear constraints and bounds. The algorithm follows the procedure shown in Figure 57.

*PART II*  
*Experimental activities*

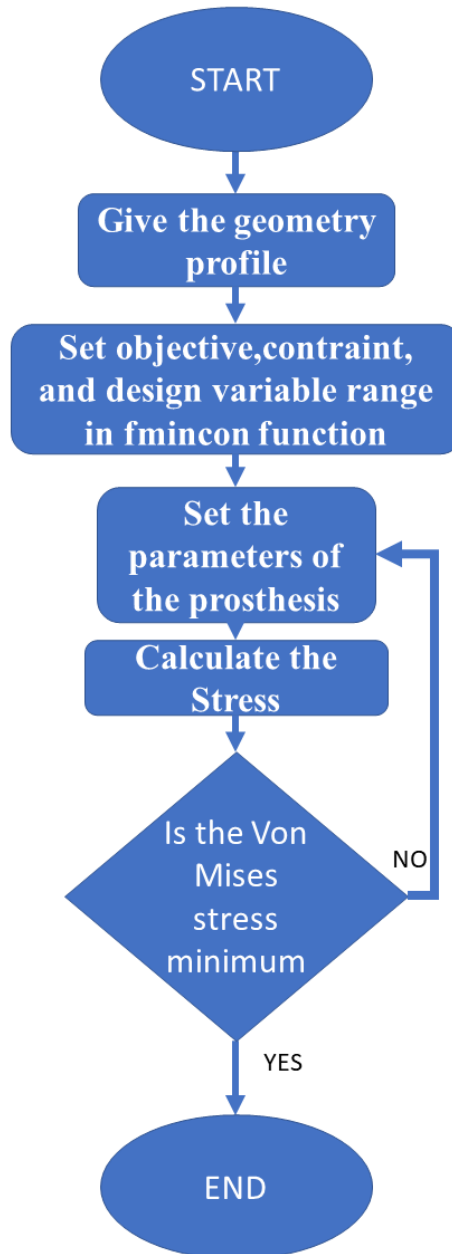


*Figure 57: Optimization chart.*

As mentioned in the introduction, this work aimed to describe a general but practical optimization framework and use that framework in the context of a structural optimization problem. The Fmincon is chosen because this algorithm converges significantly faster than other algorithms. Fmincon is the preferred algorithm, especially when function evaluations are expensive. The objective function to be minimized has as input the geometric characteristics (the three parameters that define the shape of the prosthesis) of the prosthesis system, while in output, the request is to minimize the stress of Von Mises Massimo within the system studied(Figure 57).

## PART II

### Experimental activities

The first phase of the following procedure was characterized by setting the parameters of the prosthesis. As shown in Figure 58, three independent parameters were identified for the prosthesis study. Each iteration cycle has provided that one / or more of them change simultaneously.

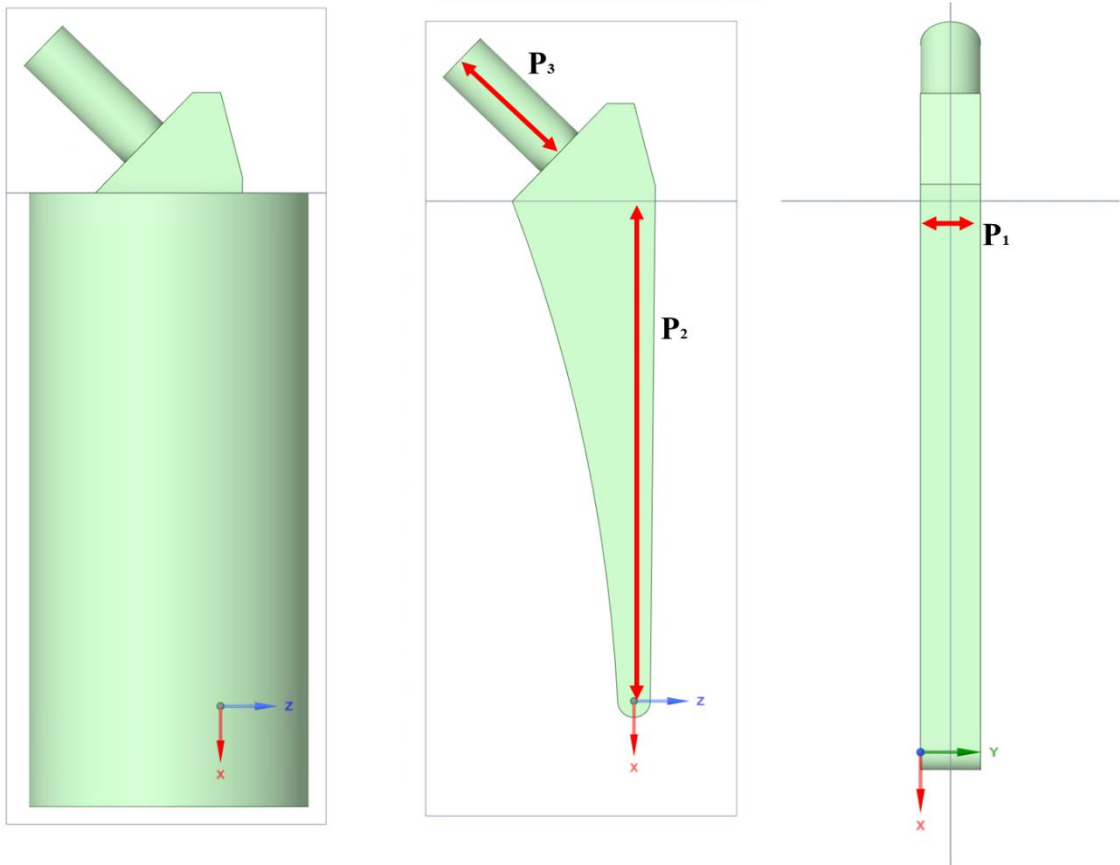
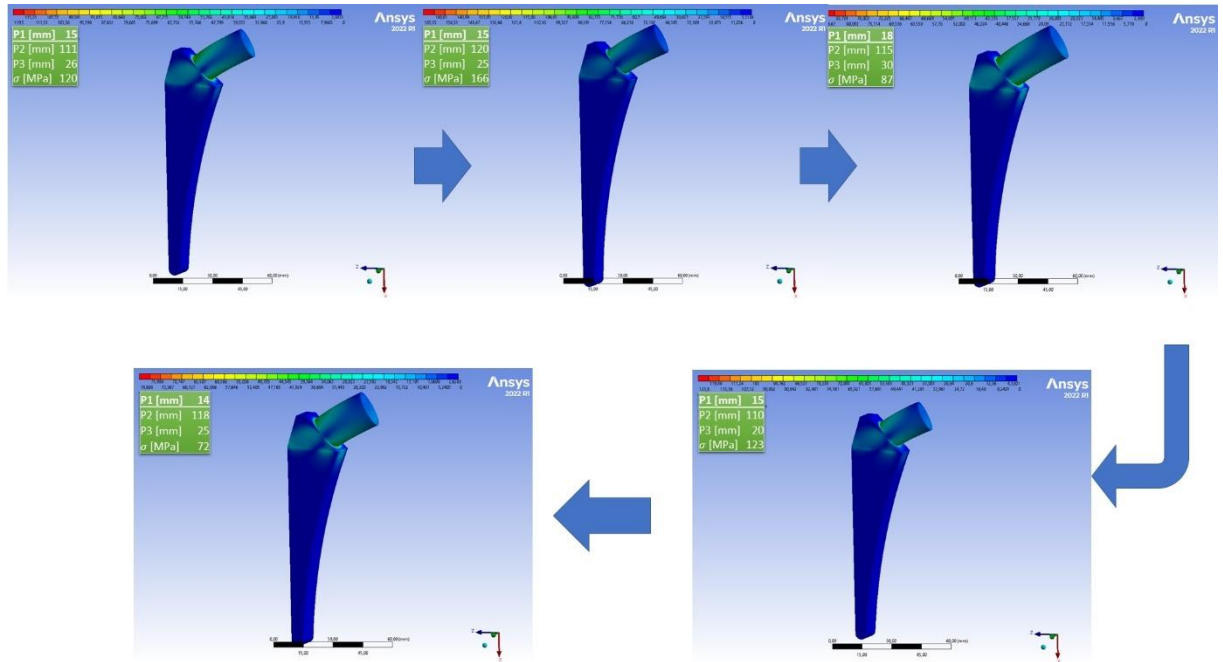


Figure 58: Parameters setting.

Three parameters have been constrained so as not to be able to assume values outside the predetermined ranges, to overcome problems such as calculating trivial solutions. Once the parameters were obtained and the geometry created, the algorithm began to iterate by calculating the system solution for the set parameters. As shown in Figure 59, the first solution was identified with characteristic prosthesis parameters for the subject chosen under examination and was identified as the target. Subsequently, the subsequent solutions were compared with this target. When the solution elaborated in the "i" cycle reported a value lower than the target, it was overwritten on it. The system carried out iterations until it captured the minimum of the objective function. Figure 59 shows a flow of simulations performed by the optimization algorithm.

*PART II*  
*Experimental activities*



*Figure 59: Simulation flow*

Once the system has been optimized, the data have been extrapolated and evaluated. Table 9 shows the change in size between the initial prosthesis and the one in which the shape has been optimized for loading.

*Table 9: Shape optimization parameters.*

Shape Optimization		
	Original Dimensions	Optimized Dimensions
P <sub>1</sub> [mm]	15	18
P <sub>2</sub> [mm]	111	114,78
P <sub>3</sub> [mm]	26	25

## PART II

### Experimental activities

Once the system has been optimized, the data have been extrapolated and evaluated. Table 10 shows the change in size between the initial prosthesis and the one in which the shape has been optimized for loading.

Table 10: Volume and mass variation.

Shape Optimization			
	Original Dimensions	Optimized Dimensions	Variation
Volume [mm <sup>3</sup> ]	28012	35066	20%
Mass [kg]	0,22	0,28	21%
Stress [MPa]	120	72	39%

It can be seen that:

- There was an increase of around 20% in both the volume and mass of the prosthesis.
- The maximum Von Mises stress calculated by the system was reduced by 39%.

It was decided to proceed with a second optimization, to optimize the weights. In this case, the optimization was topological.

Thanks to the rapid evolution of additive manufacturing today, it is possible to realize high strength open porous scaffolds constructed with beam elements [140–142], which can provide favourable property compromises when considering mechanical and biological factors. Parametric approaches can help design lattices for scaffold applications by exploiting parameter coupling and scale relationships, which has been a successful approach for designing complex biomechanical systems [237], [238]. As previously reported lattice structures can generally be classified according to their mechanical response as dominated by bending or dominated by elongation. The cellular topology of a lattice structure defines if will be bent or dominated by elongation. The most common strut-based cell topologies that have been studied

PART II

Experimental activities

are the body-centred cube (BCC). These structures dominated by elongation are rigid and robust, especially considering their mass, while structures dominated by flexion conform and deform more consistently. As in [173] this structure are used to realise hip prostheses. For this reason, Cubic cells, with crossed rods centred on the body, were used as the basis for the lattice structures. The future aim is to make a comparison between structures and obtain the best one for this type of application

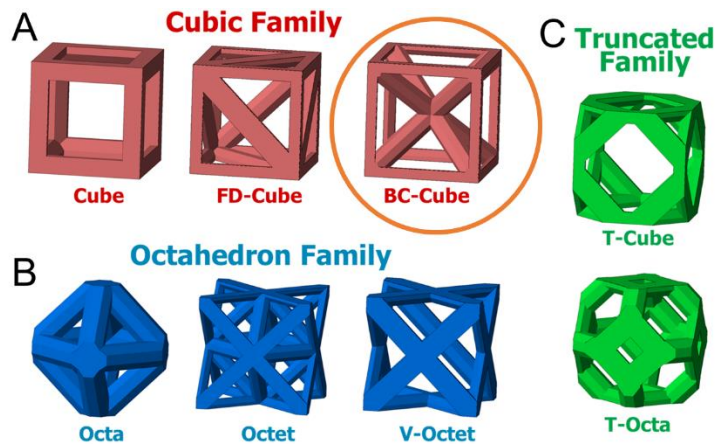


Figure 60: Unit cells are grouped in (A) Cubic, (B) Octahedron, and (C) Truncated families based on their topology.[238]

Table 11 shows the characteristics chosen for the unit cell.

Table 11: Lattice cell features.

Cell features	
Minimum density	0,1
Maximum density	0,8
Lattice cell size [mm]	1

## PART II

### Experimental activities

Once the properties attributed to the lattice were defined, a subsequent fem analysis was defined using the same conditions previously used. Once the correct shape was obtained, the following analysis identified the internal areas of the prosthesis in which the stress was lower than the critical one and overlapped them with lattice structures to decrease the sample's mass while maintaining the same values compared to the previous case. Figure 61 shows the output obtained.

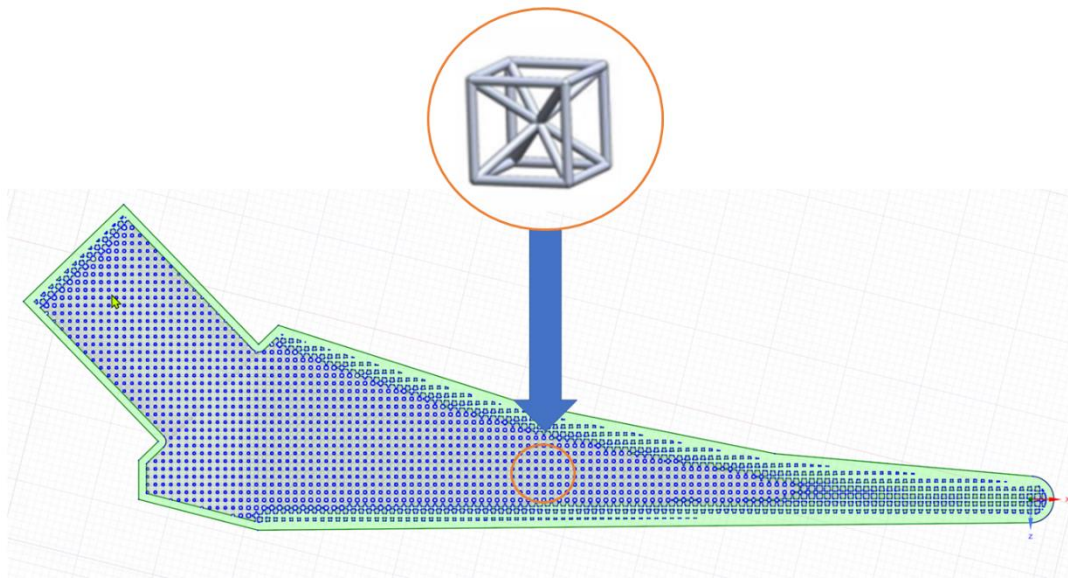


Figure 61: Lattice optimization output.

From the evaluation of the masses, after the topological optimization, a mass reduction was obtained compared to the initial case of 18%. If the choice had relapsed only to perform the shape optimization, the result would have been the opposite, i.e. an increase in mass of 21%. In this case, comparing the two optimizations, there is a 35% decrease in mass in favour of topological optimization compared to simple shape optimization. Table 12 shows the results obtained.

## PART II

### Experimental activities

Table 12: mass properties of the system before optimization and after optimization.

---

Shape Optimization			
	Original Dimensions	Shape Optimization	Lattice Optimization
Mass [kg]	0,22	0,28	0,18

---

## 5. CONCLUDING REMARKS

---

The work presented in this Ph.D. thesis is the synthesis of the intense activity research, performed over a period of three years, in the field of biomechanics.

Most of the research activities have been presented in national conferences and published in peer reviewed journals.

The main aim of the research activities performed has been the application of a new approach to define a custom geometry for an hip prosthesis.

The approach using Deep Learning algorithms has made it possible to demonstrate that it is possible to identify the pose of a subject more quickly and at a lower cost than traditional techniques.

## *PART II*

### *Experimental activities*

Using a parametric human model has broadened the horizons of the following evaluation since it allows us to identify the dynamics of several subjects simultaneously. It also allows you to define a specific subject to be analyzed.

The combined use of the multibody model with Openpose has made it possible to reduce the evaluation times for the gait analysis, thus allowing the identification of the loads acting on the hip during this cycle.

As can be seen, the use of a shape optimization algorithm has allowed optimizing the shape of the prosthesis for the load to which it is subjected. Unfortunately it has led to an increase in its weight and volume, which required the use of a second procedure, topological optimization, which made it possible to reduce the masses by about 20% compared to the initial case.

The following analysis has also deduced that neither the yield strength for this prosthesis nor the limit stress of first damage has been reached. For this reason, the analysis of the static case has been completed.

Finally, it can be deduced that the AISI 316 L material is confirmed as correct for the realization of such prostheses.

---

## REFERENCES

- [1] H. Hatze, “The meaning of the term ‘biomechanics,’” *J. Biomech.*, vol. 7, no. 2, pp. 189–190, Mar. 1974, doi: 10.1016/0021-9290(74)90060-8.
- [2] D. A. Winter, *Biomechanics and Motor Control of Human Movement: Fourth Edition*. 2009.
- [3] W. R. Shadish, T. D. Cook, and D. T. Campbell, *Experimental and Quasi-Experimental Designs for Generalized Causal Inference*. Boston: Houghton Mifflin., vol. 127. 2002.
- [4] B. Di Ventura, C. Lemerle, K. Michalodimitrakis, and L. Serrano, “From in vivo to in silico biology and back,” *Nature*, vol. 443, no. 7111. 2006, doi: 10.1038/nature05127.
- [5] H. Kitano, “Computational systems biology,” *Nature*, vol. 420, no. 6912. 2002, doi: 10.1038/nature01254.
- [6] J. H. Reif, “Computing: Successes and challenges,” *Science*, vol. 296, no. 5567. 2002, doi: 10.1126/science.1070978.
- [7] “Biomechanics of the Musculoskeletal System: Modeling of Data Uncertainty and ... - Marie-Christine Ho Ba Tho, Tien Tuan Dao - Google Libri.” [https://books.google.it/books?hl=it&lr=&id=cxuNAwAAQBAJ&oi=fnd&pg=PP6&dq=Biomechanics+of+the+Musculoskeletal+System,+Modeling+of+Data+Uncertainty+and+Knowledge&ots=6DEX0qcQTE&sig=JSsh34gTV2yGmUmNaRLvJpgQrz8&redir\\_esc=y#v=onepage&q=Biomechanics of the Musculoskeletal System%2C Modeling of Data Uncertainty and Knowledge&f=false](https://books.google.it/books?hl=it&lr=&id=cxuNAwAAQBAJ&oi=fnd&pg=PP6&dq=Biomechanics+of+the+Musculoskeletal+System,+Modeling+of+Data+Uncertainty+and+Knowledge&ots=6DEX0qcQTE&sig=JSsh34gTV2yGmUmNaRLvJpgQrz8&redir_esc=y#v=onepage&q=Biomechanics of the Musculoskeletal System%2C Modeling of Data Uncertainty and Knowledge&f=false) (accessed Aug. 23, 2022).
- [8] “Computational Modeling.” <https://www.nibib.nih.gov/science-education/science-topics/computational-modeling> (accessed Aug. 24, 2022).

## References

- [9] H. Alidousti, M. Taylor, and N. W. Bressloff, “Do capsular pressure and implant motion interact to cause high pressure in the periprosthetic bone in total hip replacement?,” *J. Biomech. Eng.*, vol. 133, no. 12, 2011, doi: 10.1115/1.4005455.
- [10] H. J. Lundberg, D. R. Pedersen, T. E. Baer, M. Muste, J. J. Callaghan, and T. D. Brown, “Effects of implant design parameters on fluid convection, potentiating third-body debris ingress into the bearing surface during THA impingement/subluxation,” *J. Biomech.*, vol. 40, no. 8, pp. 1676–1685, Jan. 2007, doi: 10.1016/J.JBIOMECH.2007.01.021.
- [11] A. E. Anderson, B. J. Ellis, and J. A. Weiss, “Verification, validation and sensitivity studies in computational biomechanics,” <http://dx.doi.org/10.1080/10255840601160484>, vol. 10, no. 3, pp. 171–184, 2007, doi: 10.1080/10255840601160484.
- [12] D. Waltemath *et al.*, “Minimum Information About a Simulation Experiment (MIASE),” *PLOS Comput. Biol.*, vol. 7, no. 4, p. e1001122, Apr. 2011, doi: 10.1371/JOURNAL.PCBI.1001122.
- [13] A. Erdemir, T. M. Guess, J. Halloran, S. C. Tadepalli, and T. M. Morrison, “Considerations for reporting finite element analysis studies in biomechanics,” *J. Biomech.*, vol. 45, no. 4, pp. 625–633, Feb. 2012, doi: 10.1016/J.JBIOMECH.2011.11.038.
- [14] A. Erdemir *et al.*, “Deciphering the ‘Art’ in Modeling and Simulation of the Knee Joint: Overall Strategy,” *J. Biomech. Eng.*, vol. 141, no. 7, p. 0710021, Jul. 2019, doi: 10.1115/1.4043346.
- [15] L. Tsai, “Robot analysis: the mechanics of serial and parallel manipulators,” *Mech. Ser. Parallel Manip.*, p. 520, 1999, Accessed: Aug. 27, 2022. [Online]. Available: <https://www.wiley.com/en-us/Robot+Analysis%3A+The+Mechanics+of+Serial+and+Parallel+Manipulators-p-9780471325932>.
- [16] T. Davies, “Kinematics and dynamics of planar machinery, Burton Paul, Prentice-Hall, N.J., 1979. Price: £21.85,” *Int. J. Numer. Methods Eng.*, vol. 15, no. 3, pp. 477–477, Mar. 1980, doi: 10.1002/NME.1620150316.

## References

- [17] “Planar Multibody Dynamics: Formulation, Programming with MATLAB®, and ... - Parviz E. Nikravesh - Google Libri.” [https://books.google.it/books?hl=it&lr=&id=3jcPEAAAQBAJ&oi=fnd&pg=PP1&dq=Nikravesh+PE+\(2008\)+Planar+multibody+dynamics:+formulation,+programming,+and+applications.+CRC+Press,+London&ots=E3NTywfXqw&sig=wuRQ\\_hao-Pa-CGDnGpsdZRpO\\_zo#v=onepage&q&f=false](https://books.google.it/books?hl=it&lr=&id=3jcPEAAAQBAJ&oi=fnd&pg=PP1&dq=Nikravesh+PE+(2008)+Planar+multibody+dynamics:+formulation,+programming,+and+applications.+CRC+Press,+London&ots=E3NTywfXqw&sig=wuRQ_hao-Pa-CGDnGpsdZRpO_zo#v=onepage&q&f=false) (accessed Aug. 27, 2022).
- [18] “Kinematics & dynamics of multibody systems with imperfect joints: Models & case studies (Lecture notes in applied & computational mechanics, Vol. 34) Flores Paulo, Ambrósio Jorge, Pimenta Claro J.C., Lankarani Hamid M.” [http://www.lavoisier.eu/books/physics/kinematics-et-dynamics-of-multibody-systems-with-imperfect-joints-models-et-case-studies-lecture-notes-in-applied-et-computational-mechanics-vol-34/description\\_2316358](http://www.lavoisier.eu/books/physics/kinematics-et-dynamics-of-multibody-systems-with-imperfect-joints-models-et-case-studies-lecture-notes-in-applied-et-computational-mechanics-vol-34/description_2316358) (accessed Aug. 27, 2022).
- [19] M. A. Neto and J. Ambrósio, “Stabilization methods for the integration of DAE in the presence of redundant constraints,” *Multibody Syst. Dyn.*, vol. 10, no. 1, pp. 81–105, 2003, doi: 10.1023/A:1024567523268.
- [20] “Dynamics of Multibody Systems - Ahmed A. Shabana - Google Libri.” [https://books.google.it/books?hl=it&lr=&id=zxuG-17J5rgC&oi=fnd&pg=PR11&dq=Shabana+AA+\(1989\)+Dynamics+of+multibody+systems.+Wiley,+New+York&ots=gQ-MDQ4xho&sig=EvG5v9j8iYtULD4S-VpA0rIx3po#v=onepage&q=Shabana+AA+\(1989\)+Dynamics+of+multibody+systems.+Wiley%2C+New+York&f=false](https://books.google.it/books?hl=it&lr=&id=zxuG-17J5rgC&oi=fnd&pg=PR11&dq=Shabana+AA+(1989)+Dynamics+of+multibody+systems.+Wiley,+New+York&ots=gQ-MDQ4xho&sig=EvG5v9j8iYtULD4S-VpA0rIx3po#v=onepage&q=Shabana+AA+(1989)+Dynamics+of+multibody+systems.+Wiley%2C+New+York&f=false) (accessed Aug. 27, 2022).
- [21] “Multibody Systems Handbook,” *Multibody Syst. Handb.*, 1990, doi: 10.1007/978-3-642-50995-7.
- [22] P. E. Nikravesh, “Computer-Aided Analysis of Mechanical Systems,” *Aerosp. Mech. Eng. Dep. Univ. Arizona*, pp. 370–388, 1988.
- [23] W. H. Zhu, J. C. Piedboeuf, and Y. Gonthier, “A dynamics formulation of general constrained robots,” *Multibody Syst. Dyn.* 2006 161, vol. 16, no. 1, pp. 37–54, Jun. 2006, doi: 10.1007/S11044-006-9011-9.
- [24] J. Ambrósio and P. Verissimo, “Sensitivity of a vehicle ride to the suspension bushing

## References

- characteristics,” *J. Mech. Sci. Technol.* 2009 234, vol. 23, no. 4, pp. 1075–1082, May 2009, doi: 10.1007/S12206-009-0344-1.
- [25] M. P. T. Silva and J. A. C. Ambrósio, “Kinematic data consistency in the inverse dynamic analysis of biomechanical systems,” *Multibody Syst. Dyn.*, vol. 8, no. 2, pp. 219–239, Sep. 2002, doi: 10.1023/A:1019545530737.
- [26] P. Flores, “A methodology for quantifying the kinematic position errors due to manufacturing and assembly tolerances,” *Stroj. Vestnik/Journal Mech. Eng.*, vol. 57, no. 6, pp. 457–467, 2011, doi: 10.5545/SV-JME.2009.159.
- [27] J. C. Pombo and J. A. C. Ambrósio, “Application of a wheel-rail contact model to railway dynamics in small radius curved tracks,” *Multibody Syst. Dyn.*, vol. 19, no. 1–2, pp. 91–114, Feb. 2008, doi: 10.1007/S11044-007-9094-Y.
- [28] R. Pàmies-Vilà, O. Pätkau, A. Dòria-Cerezo, and J. M. Font-Llagunes, “Influence of the controller design on the accuracy of a forward dynamic simulation of human gait,” *Mech. Mach. Theory*, vol. 107, pp. 123–138, Jan. 2017, doi: 10.1016/J.MECHMACHTHEORY.2016.09.002.
- [29] R. L. Huston, “Multibody Dynamics Since 1990,” *Appl. Mech. Rev.*, vol. 49, no. 10S, pp. S35–S40, Oct. 1996, doi: 10.1115/1.3101974.
- [30] A. Müller, “Generic mobility of rigid body mechanisms,” *Mech. Mach. Theory*, vol. 44, no. 6, pp. 1240–1255, Jun. 2009, doi: 10.1016/J.MECHMACHTHEORY.2008.08.002.
- [31] H. Pessink, “Theory of Machines and Mechanisms by John J. Uicker, Jr., Gordon R. Pennock, Joseph E. Shigley.” Accessed: Aug. 28, 2022. [Online]. Available: [https://www.academia.edu/44918849/Theory\\_of\\_Machines\\_and\\_Mechanisms\\_by\\_John\\_J\\_Uicker\\_Jr\\_Gordon\\_R\\_Pennock\\_Joseph\\_E\\_Shigley](https://www.academia.edu/44918849/Theory_of_Machines_and_Mechanisms_by_John_J_Uicker_Jr_Gordon_R_Pennock_Joseph_E_Shigley).
- [32] R. WEHAGE and H. EJ, “GENERALIZED COORDINATE PARTITIONING FOR DIMENSION REDUCTION IN ANALYSIS OF CONSTRAINED DYNAMIC SYSTEMS,” *Gen. Coord. PARTITIONING Dimens. Reduct. Anal. CONSTRAINED Dyn. Syst.*, 1982.
- [33] N. Orlandea, M. A. Chace, and D. A. Calahan, “A Sparsity-Oriented Approach to the

## References

- Dynamic Analysis and Design of Mechanical Systems—Part 1,” *undefined*, vol. 99, no. 3, pp. 773–779, 1977, doi: 10.1115/1.3439312.
- [34] M. A. Chace, “Analysis of the Time-Dependence of Multi-Freedom Mechanical Systems in Relative Coordinates,” *J. Eng. Ind.*, vol. 89, no. 1, pp. 119–125, Feb. 1967, doi: 10.1115/1.3609982.
- [35] J. García de Jalón and E. Bayo, “Kinematic and Dynamic Simulation of Multibody Systems,” 1994, doi: 10.1007/978-1-4612-2600-0.
- [36] “Dynamics of Multibody Systems - Ahmed A. Shabana .” [https://books.google.it/books?hl=it&lr=&id=zxuG-17J5rgC&oi=fnd&pg=PR11&dq=Shabana+AA+\(1989\)+Dynamics+of+multibody+systems.+Wiley,+New+York&ots=gQ-MEP3xhi&sig=1RmnT-4Ty1IZB-kSuM9csyTb9WE#v=onepage&q=Shabana+AA+\(1989\)+Dynamics+of+multibody+systems.+Wiley%2C+New+York&f=false](https://books.google.it/books?hl=it&lr=&id=zxuG-17J5rgC&oi=fnd&pg=PR11&dq=Shabana+AA+(1989)+Dynamics+of+multibody+systems.+Wiley,+New+York&ots=gQ-MEP3xhi&sig=1RmnT-4Ty1IZB-kSuM9csyTb9WE#v=onepage&q=Shabana+AA+(1989)+Dynamics+of+multibody+systems.+Wiley%2C+New+York&f=false) (accessed Aug. 28, 2022).
- [37] P. Flores, “Global and local coordinates,” *SpringerBriefs Appl. Sci. Technol.*, vol. 168, pp. 11–14, 2015, doi: 10.1007/978-3-319-16190-7\_3.
- [38] “Kinematics & dynamics of multibody systems with imperfect joints: Models & case studies (Lecture notes in applied & computational mechanics, Vol. 34) Flores Paulo, Ambrósio Jorge, Pimenta Claro J.C., Lankarani Hamid M.” .
- [39] “Goldstein, H. (1980) Classical Mechanics. 2nd Edition, Addison-Wesley, Reading, 31. - References - Scientific Research Publishing.” .
- [40] L. D. Landau and E. M. Lifshitz, “Volume 1 -- Mechanics,” *Course Theor. Phys.*, p. 224, 1982, Accessed: Aug. 29, 2022. [Online]. Available: [http://books.google.com/books?id=bE-9tUH2J2wC&printsec=frontcover&dq=intitle:Mechanics+inauthor:landau&hl=&cd=1&source=gbs\\_api](http://books.google.com/books?id=bE-9tUH2J2wC&printsec=frontcover&dq=intitle:Mechanics+inauthor:landau&hl=&cd=1&source=gbs_api).
- [41] P. Flores, “Fundamental concepts in multibody dynamics,” *SpringerBriefs Appl. Sci. Technol.*, vol. 168, pp. 5–9, 2015, doi: 10.1007/978-3-319-16190-7\_2.
- [42] P. Flores, “Concepts and Formulations for Spatial Multibody Dynamics,” 2015, doi:

## References

- 10.1007/978-3-319-16190-7.
- [43] P. Flores, “Euler angles, bryant angles and euler parameters,” *SpringerBriefs Appl. Sci. Technol.*, vol. 168, pp. 15–22, 2015, doi: 10.1007/978-3-319-16190-7\_4.
- [44] J. García de Jalón and E. Bayo, “Kinematic and Dynamic Simulation of Multibody Systems,” 1994, doi: 10.1007/978-1-4612-2600-0.
- [45] F. Landovitor, “General Motion of a Rigid Body.” Accessed: Aug. 30, 2022. [Online]. Available: [https://www.academia.edu/34447227/General\\_Motion\\_of\\_a\\_Rigid\\_Body](https://www.academia.edu/34447227/General_Motion_of_a_Rigid_Body).
- [46] P. E. Nikravesh, “Planar Multibody Dynamics : Formulation, Programming and Applications,” *Planar Multibody Dyn.*, Nov. 2007, doi: 10.1201/B15878.
- [47] P. E. Nikravesh, “Initial condition correction in multibody dynamics,” *Multibody Syst. Dyn. 2007 181*, vol. 18, no. 1, pp. 107–115, Jun. 2007, doi: 10.1007/S11044-007-9069-Z.
- [48] P. Flores, “Methods to solve the equations of motion,” *SpringerBriefs Appl. Sci. Technol.*, vol. 168, pp. 61–66, 2015, doi: 10.1007/978-3-319-16190-7\_12.
- [49] *The Finite Element Method: Its Basis and Fundamentals - Olek C Zienkiewicz, R. L. Taylor, J.Z. Zhu . .*
- [50] A. Hrennikoff, “Solution of Problems of Elasticity by the Framework Method,” *J. Appl. Mech.*, vol. 8, no. 4, pp. A169–A175, Dec. 1941, doi: 10.1115/1.4009129.
- [51] R. Courant, “Variational methods for the solution of problems of equilibrium and vibrations,” *Bull. Am. Math. Soc.*, vol. 49, no. 1, pp. 1–23, Jan. 1943, doi: bams/1183504922.
- [52] R. Clough and E. Wilson, “EARLY FINITE ELEMENT RESEARCH AT BERKELEY 1,” *undefined*, 1999.
- [53] “An Investigation of the Stresses in Cantilever Flat Slabs: George Alfred Maney .” .
- [54] N. Jensen-Eriksen, “Building trust: the history of DNV 1864–2014,” <https://doi.org/10.1080/03585522.2015.1032341>, vol. 63, no. 2, pp. 205–207, May 2015, doi: 10.1080/03585522.2015.1032341.

## References

- [55] M. D. Gunzburger and P. B. Bochev, “Least-Squares Finite Element Methods,” vol. 166, 2009, doi: 10.1007/B13382.
- [56] O. C. Zienkiewicz, R. L. (Robert L. Taylor, and J. Z. Zhu, “The finite element method : its basis and fundamentals,” p. 714.
- [57] T. Belytschko, D. Organ, and Y. Krongauz, “A coupled finite element-element-free Galerkin method,” *Comput. Mech.* 1995 173, vol. 17, no. 3, pp. 186–195, May 1995, doi: 10.1007/BF00364080.
- [58] J. C. Butcher, “A history of Runge-Kutta methods,” *Appl. Numer. Math.*, vol. 20, no. 3, pp. 247–260, Mar. 1996, doi: 10.1016/0168-9274(95)00108-5.
- [59] K. H. Huebner and K. H. Huebner, “The finite element method for engineers,” p. 720, 2001, Accessed: Sep. 01, 2022. [Online]. Available: <https://www.wiley.com/en-us/The+Finite+Element+Method+for+Engineers%2C+4th+Edition-p-9780471370789>.
- [60] N. M. A. Nik Long, A. A. Khaldjigitov, and U. Adambaev, “On the constitutive relations for isotropic and transversely isotropic materials,” *Appl. Math. Model.*, vol. 37, no. 14–15, pp. 7726–7740, Aug. 2013, doi: 10.1016/J.APM.2013.03.012.
- [61] F. Göncü, O. Durán, and S. Luding, “Constitutive relations for the isotropic deformation of frictionless packings of polydisperse spheres,” *Comptes Rendus Mécanique*, vol. 338, no. 10–11, pp. 570–586, Oct. 2010, doi: 10.1016/J.CRME.2010.10.004.
- [62] J. Ulrich and R. Zengerle, “Static and dynamic flow simulation of a KOH-etched microvalve using the finite-element method,” *Sensors Actuators A Phys.*, vol. 53, no. 1–3, pp. 379–385, May 1996, doi: 10.1016/0924-4247(96)80162-2.
- [63] A. Pitilakis, D. Chatzidimitriou, and E. E. Kriezis, “Theoretical and numerical modeling of linear and nonlinear propagation in graphene waveguides,” *Opt. Quantum Electron.*, vol. 48, no. 4, pp. 1–22, Apr. 2016, doi: 10.1007/S11082-016-0510-5/FIGURES/8.
- [64] “Linear Elastic Fracture Mechanics,” *Fract. Mech.*, pp. 39–72, Jan. 2004, doi: 10.1007/1-4020-7861-7\_3.
- [65] J. I. Ramos, “Linearization methods in classical and quantum mechanics,” *Comput. Phys. Commun.*, vol. 153, no. 2, pp. 199–208, Jun. 2003, doi: 10.1016/S0010-

## References

4655(03)00226-1.

- [66] *Theory of Matrix Structural Analysis - J. S. Przemieniecki . .*
- [67] J. S. Prentice, J. Homann, K. D. Simmons, G. Tkačik, V. Balasubramanian, and P. C. Nelson, “Newton-Raphson Method,” *Encycl. Appl. Comput. Math.*, pp. 1023–1028, 2015, doi: 10.1007/978-3-540-70529-1\_374.
- [68] Y. Waki, B. R. Mace, and M. J. Brennan, “Free and forced vibrations of a tyre using a wave/finite element approach,” *J. Sound Vib.*, vol. 323, no. 3–5, pp. 737–756, Jun. 2009, doi: 10.1016/J.JSV.2009.01.006.
- [69] J. S. Sun, K. H. Lee, and H. P. Lee, “Comparison of implicit and explicit finite element methods for dynamic problems,” *J. Mater. Process. Technol.*, vol. 105, no. 1–2, pp. 110–118, Sep. 2000, doi: 10.1016/S0924-0136(00)00580-X.
- [70] P. Hadagali, “Subject-specific finite element modeling of the adolescent thoracic spine for scoliosis research,” *undefined*, 2014.
- [71] W. E. Frazier, “Metal additive manufacturing: A review,” *J. Mater. Eng. Perform.*, vol. 23, no. 6, pp. 1917–1928, Apr. 2014, doi: 10.1007/S11665-014-0958-Z/FIGURES/9.
- [72] I. Campbell, D. Bourell, and I. Gibson, “Additive manufacturing: rapid prototyping comes of age,” *Rapid Prototyp. J.*, vol. 18, no. 4, pp. 255–258, Jun. 2012, doi: 10.1108/13552541211231563/FULL/PDF.
- [73] H. J. Jee and E. Sachs, “A visual simulation technique for 3D printing,” *Adv. Eng. Softw.*, vol. 31, no. 2, pp. 97–106, Feb. 2000, doi: 10.1016/S0965-9978(99)00045-9.
- [74] C. M. Cheah, C. K. Chua, C. W. Lee, C. Feng, and K. Totong, “Rapid prototyping and tooling techniques: a review of applications for rapid investment casting,” *Int. J. Adv. Manuf. Technol.* 2004 253, vol. 25, no. 3, pp. 308–320, Aug. 2004, doi: 10.1007/S00170-003-1840-6.
- [75] “Rapid Prototyping, Principles and Applications,” *Assem. Autom.*, vol. 30, no. 4, Sep. 2010, doi: 10.1108/AA.2010.03330DAE.001.
- [76] J. Giannatsis and V. Dedoussis, “Additive fabrication technologies applied to medicine

## References

- and health care: a review,” *Int. J. Adv. Manuf. Technol.* 2007 401, vol. 40, no. 1, pp. 116–127, Dec. 2007, doi: 10.1007/S00170-007-1308-1.
- [77] F. Rengier *et al.*, “3D printing based on imaging data: review of medical applications,” *Int. J. Comput. Assist. Radiol. Surg.* 2010 54, vol. 5, no. 4, pp. 335–341, May 2010, doi: 10.1007/S11548-010-0476-X.
- [78] E. L. S. Da Rosa, C. F. Oleskovicz, and B. N. Aragão, “Rapid prototyping in Maxillofacial Surgery and Traumatology,” *Braz. Dent. J.*, vol. 15, no. 3, pp. 243–247, 2004, doi: 10.1590/S0103-64402004000300015.
- [79] V. Petrovic *et al.*, “Additive layered manufacturing: sectors of industrial application shown through case studies,” <https://doi.org/10.1080/00207540903479786>, vol. 49, no. 4, pp. 1061–1079, Feb. 2010, doi: 10.1080/00207540903479786.
- [80] X. Yan and P. Gu, “A review of rapid prototyping technologies and systems,” *Comput. Des.*, vol. 28, no. 4, pp. 307–318, Apr. 1996, doi: 10.1016/0010-4485(95)00035-6.
- [81] S. H. Choi and S. Samavedam, “Visualisation of rapid prototyping,” *Rapid Prototyp. J.*, vol. 7, no. 2, pp. 99–114, 2001, doi: 10.1108/13552540110386763/FULL/PDF.
- [82] T. G. Spears and S. A. Gold, “In-process sensing in selective laser melting (SLM) additive manufacturing,” *Integr. Mater. Manuf. Innov.*, vol. 5, no. 1, pp. 16–40, Dec. 2016, doi: 10.1186/S40192-016-0045-4.
- [83] F. Amado, M. Schmid, G. Levy, and K. Wegener, “Advances in SLS Powder Characterization,” *undefined*, 2011.
- [84] T. Kurzynowski, E. Chlebus, B. Kuźnicka, and J. Reiner, “Parameters in selective laser melting for processing metallic powders,” <https://doi.org/10.1117/12.907292>, vol. 8239, pp. 317–322, Feb. 2012, doi: 10.1117/12.907292.
- [85] I. Yadroitsev, P. Bertrand, and I. Smurov, “Parametric analysis of the selective laser melting process,” *Appl. Surf. Sci.*, vol. 253, no. 19, pp. 8064–8069, Jul. 2007, doi: 10.1016/J.APSUSC.2007.02.088.
- [86] M. Van Elsen, “Complexity of selective laser melting : a new optimisation approach.” 2007, Accessed: Sep. 24, 2022. [Online]. Available: <https://lirias.kuleuven.be/1746431>.

## References

- [87] P. Fischer *et al.*, “Microstructure of near-infrared pulsed laser sintered titanium samples,” *Appl. Phys. A* 2003 788, vol. 78, no. 8, pp. 1219–1227, May 2004, doi: 10.1007/S00339-003-2205-6.
- [88] P. Fischer, V. Romano, H. P. Weber, N. P. Karapatis, E. Boillat, and R. Glardon, “Sintering of commercially pure titanium powder with a Nd:YAG laser source,” *Acta Mater.*, vol. 51, no. 6, pp. 1651–1662, Apr. 2003, doi: 10.1016/S1359-6454(02)00567-0.
- [89] D. Buchbinder, H. Schleifenbaum, S. Heidrich, W. Meiners, and J. Bültmann, “High Power Selective Laser Melting (HP SLM) of Aluminum Parts,” *undefined*, vol. 12, no. PART 1, pp. 271–278, 2011, doi: 10.1016/J.PHPRO.2011.03.035.
- [90] K. A. Mumtaz, P. Erasenthiran, and N. Hopkinson, “High density selective laser melting of Waspaloy®,” *J. Mater. Process. Technol.*, vol. 195, no. 1–3, pp. 77–87, Jan. 2008, doi: 10.1016/J.JMATPROTEC.2007.04.117.
- [91] W. M. Steen and J. Mazumder, “Laser material processing: Fourth edition,” *Laser Mater. Process. Fourth Ed.*, pp. 1–558, 2010, doi: 10.1007/978-1-84996-062-5/COVER.
- [92] M. Agarwala, D. Bourell, J. Beaman, H. Marcus, and J. Barlow, “Direct selective laser sintering of metals,” *Rapid Prototyp. J.*, vol. 1, no. 1, pp. 26–36, 1995, doi: 10.1108/13552549510078113/FULL/XML.
- [93] C. Hauser *et al.*, “Direct Selective Laser Sintering of Tool Steel Powders to High Density: Part A - Effects of Laser Beam Width and Scan Strategy,” 2003, doi: 10.26153/TSW/5625.
- [94] J. P. Kruth, L. Froyen, J. Van Vaerenbergh, P. Mercelis, M. Rombouts, and B. Lauwers, “Selective laser melting of iron-based powder,” *J. Mater. Process. Technol.*, vol. 149, no. 1–3, pp. 616–622, Jun. 2004, doi: 10.1016/J.JMATPROTEC.2003.11.051.
- [95] A. V. Gusarov and J. P. Kruth, “Modelling of radiation transfer in metallic powders at laser treatment,” *Int. J. Heat Mass Transf.*, vol. 48, no. 16, pp. 3423–3434, Jul. 2005, doi: 10.1016/J.IJHEATMASSTRANSFER.2005.01.044.
- [96] A. V. Gusarov and I. Smurov, “Radiation transfer in metallic powder beds used in laser

## References

- processing,” *J. Quant. Spectrosc. Radiat. Transf.*, vol. 111, no. 17–18, pp. 2517–2527, Nov. 2010, doi: 10.1016/J.JQSRT.2010.07.009.
- [97] N. K. Tolochko, M. K. Arshinov, A. V. Gusarov, V. I. Titov, T. Laoui, and L. Froyen, “Mechanisms of selective laser sintering and heat transfer in Ti powder,” *Rapid Prototyp. J.*, vol. 9, no. 5, pp. 314–326, 2003, doi: 10.1108/13552540310502211/FULL/XML.
- [98] J. Hoffman and Z. Szymański, “Time-dependent spectroscopy of plasma plume under laser welding conditions,” *J. Phys. D. Appl. Phys.*, vol. 37, no. 13, p. 1792, Jun. 2004, doi: 10.1088/0022-3727/37/13/010.
- [99] C. Hauser, T. H. C. Childs, K. W. Dalgarno, and R. B. Eane, “Atmospheric Control during Direct Selective Laser Sintering of Stainless Steel 314S Powder,” 1999, doi: 10.26153/TSW/747.
- [100] C. X. Zhao *et al.*, “The effect of oxygen on transitional Marangoni flow in laser spot welding,” *Acta Mater.*, vol. 58, no. 19, pp. 6345–6357, Nov. 2010, doi: 10.1016/J.ACTAMAT.2010.07.056.
- [101] S. Lu, H. Fujii, and K. Nogi, “Sensitivity of Marangoni convection and weld shape variations to welding parameters in O<sub>2</sub>–Ar shielded GTA welding,” *Scr. Mater.*, vol. 51, no. 3, pp. 271–277, Aug. 2004, doi: 10.1016/J.SCRIPTAMAT.2004.03.004.
- [102] S. Lu, H. Fujii, and K. Nogi, “Marangoni convection and weld shape variations in Ar–O<sub>2</sub> and Ar–CO<sub>2</sub> shielded GTA welding,” *Mater. Sci. Eng. A*, vol. 380, no. 1–2, pp. 290–297, Aug. 2004, doi: 10.1016/J.MSEA.2004.05.057.
- [103] J. P. Kruth, G. Levy, F. Klocke, and T. H. C. Childs, “Consolidation phenomena in laser and powder-bed based layered manufacturing,” *CIRP Ann.*, vol. 56, no. 2, pp. 730–759, Jan. 2007, doi: 10.1016/J.CIRP.2007.10.004.
- [104] T. Prosthetics, O. Author, and D. Shurr, “Text Book(s) BME 542 Prosthetics and Orthotics,” Accessed: Sep. 24, 2022. [Online]. Available: <http://www.bmcentral.com/publications/>-<http://www.sciencedirect.com>-<http://www.elsevier.com>-<http://www.springer.com>-<http://www.scholar.google.com>-<http://www.resna.org/>.

## References

- [105] P. Han, “Additive Design and Manufacturing of Jet Engine Parts,” *Engineering*, vol. 3, no. 5, pp. 648–652, Oct. 2017, doi: 10.1016/J.ENG.2017.05.017.
- [106] D. Totah, I. Kovalenko, M. Saez, and K. Barton, “Manufacturing Choices for Ankle-Foot Orthoses: A Multi-objective Optimization,” *Procedia CIRP*, vol. 65, pp. 145–150, Jan. 2017, doi: 10.1016/J.PROCIR.2017.04.014.
- [107] T. Kurfess and W. J. Cass, “Rethinking Additive Manufacturing and Intellectual Property Protection,” <http://dx.doi.org/10.5437/08956308X5705256>, vol. 57, no. 5, pp. 35–42, Sep. 2015, doi: 10.5437/08956308X5705256.
- [108] Q. Yan *et al.*, “A Review of 3D Printing Technology for Medical Applications,” *Engineering*, vol. 4, no. 5, pp. 729–742, Oct. 2018, doi: 10.1016/J.ENG.2018.07.021.
- [109] C. Weller, R. Kleer, and F. T. Piller, “Economic implications of 3D printing: Market structure models in light of additive manufacturing revisited,” *Int. J. Prod. Econ.*, vol. 164, pp. 43–56, Jun. 2015, doi: 10.1016/J.IJPE.2015.02.020.
- [110] J. H. P. Pallari *et al.*, “Design and Additive Fabrication of Foot and Ankle-Foot Orthoses,” 2010, doi: 10.26153/TSW/15248.
- [111] A. Bandyopadhyay and B. Heer, “Additive manufacturing of multi-material structures,” *Mater. Sci. Eng. R Reports*, vol. 129, pp. 1–16, Jul. 2018, doi: 10.1016/J.MSER.2018.04.001.
- [112] Y. Jin, Y. He, and A. Shih, “Process Planning for the Fuse Deposition Modeling of Ankle-Foot-Othoses,” *Procedia CIRP*, vol. 42, pp. 760–765, Jan. 2016, doi: 10.1016/J.PROCIR.2016.02.315.
- [113] M. C. Faustini, R. R. Neptune, R. H. Crawford, and S. J. Stanhope, “Manufacture of passive dynamic ankle-foot orthoses using selective laser sintering,” *IEEE Trans. Biomed. Eng.*, vol. 55, no. 2, pp. 784–790, Feb. 2008, doi: 10.1109/TBME.2007.912638.
- [114] C. Mavroidis *et al.*, “Patient specific ankle-foot orthoses using rapid prototyping,” *J. Neuroeng. Rehabil.*, vol. 8, no. 1, 2011, doi: 10.1186/1743-0003-8-1.
- [115] N. G. Harper, E. M. Russell, J. M. Wilken, and R. R. Neptune, “Selective laser sintered versus carbon fiber passive-dynamic ankle-foot orthoses: A comparison of patient

## References

- walking performance,” *J. Biomech. Eng.*, vol. 136, no. 9, 2014, doi: 10.1115/1.4027755.
- [116] A. S. Salles and D. E. Gy, “An evaluation of personalised insoles developed using additive manufacturing,” <https://doi.org/10.1080/02640414.2012.736629>, vol. 31, no. 4, pp. 442–450, Apr. 2013, doi: 10.1080/02640414.2012.736629.
- [117] A. S. Salles and D. E. Gyi, “The specification of personalised insoles using additive manufacturing,” *Work*, vol. 41, no. Supplement 1, pp. 1771–1774, Jan. 2012, doi: 10.3233/WOR-2012-0383-1771.
- [118] J. H. P. Pallari, K. W. Dalgarno, and J. Woodburn, “Mass customization of foot orthoses for rheumatoid arthritis using selective laser sintering,” *IEEE Trans. Biomed. Eng.*, vol. 57, no. 7, pp. 1750–1756, 2010, doi: 10.1109/TBME.2010.2044178.
- [119] S. Telfer, J. Pallari, J. Munguia, K. Dalgarno, M. McGeough, and J. Woodburn, “Embracing additive manufacture: Implications for foot and ankle orthosis design,” *BMC Musculoskelet. Disord.*, vol. 13, 2012, doi: 10.1186/1471-2474-13-84.
- [120] H. L. Fan, F. H. Meng, and W. Yang, “Sandwich panels with Kagome lattice cores reinforced by carbon fibers,” *Compos. Struct.*, vol. 81, no. 4, pp. 533–539, Dec. 2007, doi: 10.1016/J.COMPSTRUCT.2006.09.011.
- [121] G. W. Kooistra, V. S. Deshpande, and H. N. G. Wadley, “Compressive behavior of age hardenable tetrahedral lattice truss structures made from aluminium,” *Acta Mater.*, vol. 52, no. 14, pp. 4229–4237, Aug. 2004, doi: 10.1016/J.ACTAMAT.2004.05.039.
- [122] D. T. Queheillalt, Y. Murty, and H. N. G. Wadley, “Mechanical properties of an extruded pyramidal lattice truss sandwich structure,” *Scr. Mater.*, vol. 58, no. 1, pp. 76–79, Jan. 2008, doi: 10.1016/J.SCRIPTAMAT.2007.08.041.
- [123] H. Fan, F. Sun, L. Yang, F. Jin, and D. Zhao, “Interlocked hierarchical lattice materials reinforced by woven textile sandwich composites,” *Compos. Sci. Technol.*, vol. 87, pp. 142–148, Oct. 2013, doi: 10.1016/J.COMPSCITECH.2013.07.028.
- [124] H. L. Fan, T. Zeng, D. N. Fang, and W. Yang, “Mechanics of advanced fiber reinforced lattice composites,” *Acta Mech. Sin. 2011 266*, vol. 26, no. 6, pp. 825–835, Jan. 2011, doi: 10.1007/S10409-010-0390-Z.

## References

- [125] W. Li, F. Sun, P. Wang, H. Fan, and D. Fang, “A novel carbon fiber reinforced lattice truss sandwich cylinder: Fabrication and experiments,” *Compos. Part A Appl. Sci. Manuf.*, vol. 81, pp. 313–322, Feb. 2016, doi: 10.1016/J.COMPOSITESA.2015.11.034.
- [126] I. Maskery, N. T. Aboulkhair, A. O. Aremu, C. J. Tuck, and I. A. Ashcroft, “Compressive failure modes and energy absorption in additively manufactured double gyroid lattices,” *Addit. Manuf.*, vol. 16, pp. 24–29, Aug. 2017, doi: 10.1016/J.ADDMA.2017.04.003.
- [127] T. Maconachie *et al.*, “SLM lattice structures: Properties, performance, applications and challenges,” *Mater. Des.*, vol. 183, p. 108137, Dec. 2019, doi: 10.1016/J.MATDES.2019.108137.
- [128] M. Leary *et al.*, “Inconel 625 lattice structures manufactured by selective laser melting (SLM): Mechanical properties, deformation and failure modes,” *Mater. Des.*, vol. 157, pp. 179–199, Nov. 2018, doi: 10.1016/J.MATDES.2018.06.010.
- [129] M. F. Ashby, “The properties of foams and lattices,” *Philos. Trans. R. Soc. A Math. Phys. Eng. Sci.*, vol. 364, no. 1838, pp. 15–30, Nov. 2005, doi: 10.1098/RSTA.2005.1678.
- [130] C. Yan, L. Hao, A. Hussein, P. Young, and D. Rayment, “Advanced lightweight 316L stainless steel cellular lattice structures fabricated via selective laser melting,” *Mater. Des.*, vol. 55, pp. 533–541, Mar. 2014, doi: 10.1016/J.MATDES.2013.10.027.
- [131] M. E. Hiller *et al.*, “The design of impact absorbing structures for additive manufacture,” *J. Phys. Conf. Ser.*, vol. 382, no. 1, p. 012042, Aug. 2012, doi: 10.1088/1742-6596/382/1/012042.
- [132] N. Guo and M. C. Leu, “Additive manufacturing: technology, applications and research needs,” *Front. Mech. Eng. 2013* 83, vol. 8, no. 3, pp. 215–243, May 2013, doi: 10.1007/S11465-013-0248-8.
- [133] E. Alabort, D. Barba, and R. C. Reed, “Design of metallic bone by additive manufacturing,” *Scr. Mater.*, vol. 164, pp. 110–114, Apr. 2019, doi: 10.1016/J.SCRIPTAMAT.2019.01.022.

## References

- [134] L. Mullen, R. C. Stamp, W. K. Brooks, E. Jones, and C. J. Sutcliffe, “Selective Laser Melting: A regular unit cell approach for the manufacture of porous, titanium, bone in-growth constructs, suitable for orthopedic applications,” *J. Biomed. Mater. Res. Part B Appl. Biomater.*, vol. 89B, no. 2, pp. 325–334, May 2009, doi: 10.1002/JBM.B.31219.
- [135] A. A. Zadpoor, “Mechanical performance of additively manufactured meta-biomaterials,” *Acta Biomater.*, vol. 85, pp. 41–59, Feb. 2019, doi: 10.1016/J.ACTBIO.2018.12.038.
- [136] P. Köhnen, C. Haase, J. Bültmann, S. Ziegler, J. H. Schleifenbaum, and W. Bleck, “Mechanical properties and deformation behavior of additively manufactured lattice structures of stainless steel,” *Mater. Des.*, vol. 145, pp. 205–217, May 2018, doi: 10.1016/J.MATDES.2018.02.062.
- [137] S. Babaei, J. Shim, J. C. Weaver, E. R. Chen, N. Patel, and K. Bertoldi, “3D Soft Metamaterials with Negative Poisson’s Ratio,” *Adv. Mater.*, vol. 25, no. 36, pp. 5044–5049, Sep. 2013, doi: 10.1002/ADMA.201301986.
- [138] E. B. Duoss *et al.*, “Three-Dimensional Printing of Elastomeric, Cellular Architectures with Negative Stiffness,” *Adv. Funct. Mater.*, vol. 24, no. 31, pp. 4905–4913, Aug. 2014, doi: 10.1002/ADFM.201400451.
- [139] X. Zheng *et al.*, “Ultralight, ultrastiff mechanical metamaterials,” *Science (80-. )*, vol. 344, no. 6190, pp. 1373–1377, Jun. 2014, doi: 10.1126/SCIENCE.1252291/SUPPL\_FILE/ZHENG.SM.PDF.
- [140] H. E. Burton *et al.*, “The design of additively manufactured lattices to increase the functionality of medical implants,” *Mater. Sci. Eng. C*, vol. 94, pp. 901–908, Jan. 2019, doi: 10.1016/J.MSEC.2018.10.052.
- [141] A. Zargarian, M. Esfahanian, J. Kadkhodapour, S. Ziaei-Rad, and D. Zamani, “On the fatigue behavior of additive manufactured lattice structures,” *Theor. Appl. Fract. Mech.*, vol. 100, pp. 225–232, Apr. 2019, doi: 10.1016/J.TAFMEC.2019.01.012.
- [142] B. N. Tillmann, “Atlas der Anatomie des Menschen,” 2016, doi: 10.1007/978-3-662-49288-8.

## References

- [143] G. Wu and P. R. Cavanagh, "ISB recommendations for standardization in the reporting of kinematic data," *J. Biomech.*, vol. 28, no. 10, pp. 1257–1261, Oct. 1995, doi: 10.1016/0021-9290(95)00017-C.
- [144] E. G. Kamel *et al.*, "Measurement of abdominal fat by magnetic resonance imaging, dual-energy X-ray absorptiometry and anthropometry in non-obese men and women," *Int. J. Obes. Relat. Metab. Disord.*, vol. 23, no. 7, pp. 686–692, 1999, doi: 10.1038/SJ.IJO.0800904.
- [145] M. Garrouste-Orgeas *et al.*, "Body mass index: An additional prognostic factor in ICU patients," *Intensive Care Med.*, vol. 30, no. 3, pp. 437–443, Mar. 2004, doi: 10.1007/S00134-003-2095-2/TABLES/5.
- [146] M. A. Rahim, M. O. Tokhi, and N. F. M. Nasir, "Modeling and simulation of sit-to-stand exercise," *IFMBE Proc.*, vol. 15, pp. 204–207, 2007, doi: 10.1007/978-3-540-68017-8\_53.
- [147] R. Contini, R. J. Drillis, and M. Bluestein, "DETERMINATION OF BODY SEGMENT PARAMETERS," *Hum. Factors*, vol. 5, no. 5, pp. 493–504, 1963, doi: 10.1177/001872086300500508.
- [148] R. F. Chandler, C. E. Clauser, J. Mcconville, H. Reynolds, and J. Young, "INVESTIGATION OF INERTIAL PROPERTIES OF THE HUMAN BODY," *undefined*, 1975.
- [149] W. T. (Wilfrid T. Dempster, "Space requirements of the seated operator : geometrical, kinematic, and mechanical aspects of the body, with special reference to the limbs," 1955, Accessed: Sep. 24, 2022. [Online]. Available: <http://deepblue.lib.umich.edu/handle/2027.42/4540>.
- [150] B. N. Tillmann, "Atlas der Anatomie des Menschen: [mit Muskeltrainer; neue Approbationsordnung]," 2005.
- [151] D. A. Winter, "Biomechanics and Motor Control of Human Movement: Fourth Edition," *Biomech. Mot. Control Hum. Mov. Fourth Ed.*, pp. 1–370, Sep. 2009, doi: 10.1002/9780470549148.

## References

- [152] M. W. Whittle, “An introduction to gait analysis,” *An Introd. to Gait Anal.*, pp. 1–255, Feb. 2007, doi: 10.1016/B978-0-7506-8883-3.X5001-6.
- [153] C. Tunca, N. Pehlivan, N. Ak, B. Arnrich, G. Salur, and C. Ersoy, “Inertial Sensor-Based Robust Gait Analysis in Non-Hospital Settings for Neurological Disorders,” *Sensors 2017, Vol. 17, Page 825*, vol. 17, no. 4, p. 825, Apr. 2017, doi: 10.3390/S17040825.
- [154] K. Tong and M. H. Granat, “A practical gait analysis system using gyroscopes,” *Med. Eng. Phys.*, vol. 21, no. 2, pp. 87–94, Mar. 1999, doi: 10.1016/S1350-4533(99)00030-2.
- [155] A. Qammaz, D. Michel, and A. Argyros, “A Hybrid Method for 3D Pose Estimation of Personalized Human Body Models,” *Proc. - 2018 IEEE Winter Conf. Appl. Comput. Vision, WACV 2018*, vol. 2018-January, pp. 456–465, May 2018, doi: 10.1109/WACV.2018.00056.
- [156] S. Jin *et al.*, “Towards Multi-Person Pose Tracking: Bottom-up and Top-down Methods,” 2017.
- [157] A. Toshev and C. Szegedy, “DeepPose: Human Pose Estimation via Deep Neural Networks,” *Proc. IEEE Comput. Soc. Conf. Comput. Vis. Pattern Recognit.*, pp. 1653–1660, Dec. 2013, doi: 10.1109/CVPR.2014.214.
- [158] H. Ep, “A MATHEMATICAL MODEL OF THE HUMAN BODY. AMRL-TR-64-102.,” *undefined*, 1964.
- [159] J. Wicke and G. A. Dumas, “Influence of the Volume and Density Functions Within Geometric Models for Estimating Trunk Inertial Parameters,” *J. Appl. Biomech.*, vol. 26, no. 1, pp. 26–31, Feb. 2010, doi: 10.1123/JAB.26.1.26.
- [160] “Estimation of the Mass of Body Segments - James T. Barter - Google Libri.” [https://books.google.it/books/about/Estimation\\_of\\_the\\_Mass\\_of\\_Body\\_Segments.html?id=HVniO-Yy0\\_QC&redir\\_esc=y](https://books.google.it/books/about/Estimation_of_the_Mass_of_Body_Segments.html?id=HVniO-Yy0_QC&redir_esc=y) (accessed Sep. 24, 2022).
- [161] “Contour Maps, Center of Gravity, Moment of Inertia and Surface Area of the ... - A. P. Weinbach - Google Books.” [https://books.google.it/books/about/Contour\\_Maps\\_Center\\_of\\_Gravity\\_Moment\\_of.htm](https://books.google.it/books/about/Contour_Maps_Center_of_Gravity_Moment_of.htm)

## References

- l?id=7XkIngEACAAJ&hl=en&output=html\_text&redir\_esc=y (accessed Sep. 24, 2022).
- [162] Y. L. L. MM, and D. G, “Study of the Inertial Parameters Segments among 30 Women of Porto/Novo (Benin) by the Application of the Method of Jensen,” *Gynecol. Obstet.*, vol. 4, no. 9, pp. 1–5, 2014, doi: 10.4172/2161-0932.1000241.
- [163] H. Hatze, “A mathematical model for the computational determination of parameter values of anthropomorphic segments,” *J. Biomech.*, vol. 13, no. 10, pp. 833–843, Jan. 1980, doi: 10.1016/0021-9290(80)90171-2.
- [164] W. Robertson, “A modern take on the theoretical modelling of inertial properties of a human body for biomechanical simulations,” *MODSIM2013*, Jan. 2013, Accessed: Sep. 24, 2022. [Online]. Available: [https://www.academia.edu/5324287/A\\_modern\\_take\\_on\\_the\\_theoretical\\_modelling\\_of\\_inertial\\_properties\\_of\\_a\\_human\\_body\\_for\\_biomechanical\\_simulations](https://www.academia.edu/5324287/A_modern_take_on_the_theoretical_modelling_of_inertial_properties_of_a_human_body_for_biomechanical_simulations).
- [165] M. R. Yeadon, “The simulation of aerial movement—II. A mathematical inertia model of the human body,” *J. Biomech.*, vol. 23, no. 1, pp. 67–74, Jan. 1990, doi: 10.1016/0021-9290(90)90370-I.
- [166] F. Cucinotta, E. Guglielmino, G. Longo, G. Risitano, D. Santonocito, and F. Sfravara, “Topology optimization additive manufacturing-oriented for a biomedical application,” *Lect. Notes Mech. Eng.*, pp. 184–193, 2019, doi: 10.1007/978-3-030-12346-8\_18.
- [167] G. Epasto *et al.*, “Experimental investigation of rhombic dodecahedron micro-lattice structures manufactured by Electron Beam Melting,” *Mater. Today Proc.*, vol. 7, pp. 578–585, Jan. 2019, doi: 10.1016/J.MATPR.2018.12.011.
- [168] G. Epasto, G. Palomba, D. D’Andrea, E. Guglielmino, S. Di Bella, and F. Traina, “Ti-6Al-4V ELI microlattice structures manufactured by electron beam melting: Effect of unit cell dimensions and morphology on mechanical behaviour,” *Mater. Sci. Eng. A* 2019, Vol. 753, Pages 31-41, vol. 753, pp. 31–41, Mar. 2019, doi: 10.1016/J.MSEA.2019.03.014.
- [169] M. Fellah, M. Labaiz, O. Assala, L. Dekhil, N. Zerniz, and A. Iost, “Tribological behavior of biomaterial for total hip prosthesis,” *Mater. Tech.*, vol. 102, no. 6–7, 2014,

## References

doi: 10.1051/MATTECH/2014027.

- [170] V. O. Saikko, “A three-axis hip joint simulator for wear and friction studies on total hip prostheses,” *Proc. Inst. Mech. Eng. H.*, vol. 210, no. 3, pp. 175–185, 1996, doi: 10.1243/PIME\_PROC\_1996\_210\_410\_02.
- [171] A. Unsworth, R. M. Hall, I. C. Burgess, B. M. Wroblewski, R. M. Streicher, and M. Semlitsch, “Frictional resistance of new and explanted artificial hip joints,” *Wear*, vol. 2, no. 190, pp. 226–231, 1995, Accessed: Sep. 04, 2022. [Online]. Available: <https://www.infona.pl/resource/bwmetal.element.elsevier-3db4ee57-aa15-3634-a6bf-4ce0b7515bcf>.
- [172] S. Shankar *et al.*, “Tribological behavior of zirconia-toughened alumina (ZTA) against Ti6Al4V under different bio-lubricants in hip prosthesis using experimental and finite element concepts,” *Mater. Lett.*, vol. 307, Jan. 2022, doi: 10.1016/j.matlet.2021.131107.
- [173] G. Cortis, I. Mileti, F. Nalli, E. Palermo, and L. Cortese, “Additive manufacturing structural redesign of hip prostheses for stress-shielding reduction and improved functionality and safety,” *Mech. Mater.*, vol. 165, p. 104173, Feb. 2022, doi: 10.1016/J.MECHMAT.2021.104173.
- [174] L. E. Murr, “Additive manufacturing of biomedical devices: an overview,” *Mater. Technol.*, vol. 33, no. 1, pp. 57–70, Jan. 2018, doi: 10.1080/10667857.2017.1389052.
- [175] N. Kourra *et al.*, “Computed tomography metrological examination of additive manufactured acetabular hip prosthesis cups,” *Addit. Manuf.*, vol. 22, pp. 146–152, Aug. 2018, doi: 10.1016/J.ADDMA.2018.04.033.
- [176] R. M. R. Prince *et al.*, “ZrC-Impregnated titanium-based coating as an effective lubricating barrier for artificial hip prosthesis,” *Mater. Perform. Charact.*, vol. 10, no. 1, pp. 189–205, Jan. 2021, doi: 10.1520/MPC20200075.
- [177] V. Kashyap and P. Ramkumar, “DLC coating over pre-oxidized and textured Ti6Al4V for superior adhesion and tribo-performance of hip implant,” *Surf. Coatings Technol.*, vol. 440, p. 128492, Jun. 2022, doi: 10.1016/J.SURFCOAT.2022.128492.
- [178] V. Kashyap and P. Ramkumar, “Comprehensive analysis of geometrical parameters of

## References

- crosshatched texture for enhanced tribological performance under biological environment:,” <https://doi.org/10.1177/1350650120915136>, vol. 235, no. 2, pp. 434–452, Mar. 2020, doi: 10.1177/1350650120915136.
- [179] Q. Allen and B. Raeymaekers, “The Effect of Texture Floor Profile on the Lubricant Film Thickness in a Textured Hard-On-Soft Bearing With Relevance to Prosthetic Hip Implants,” *J. Tribol.*, vol. 143, no. 2, Feb. 2021, doi: 10.1115/1.4047753.
- [180] A. Khaskhoussi, G. Risitano, L. Calabrese, and D. D’andrea, “Investigation of the Wettability Properties of Different Textured Lead/Lead-Free Bronze Coatings,” *Lubr. 2022, Vol. 10, Page 82*, vol. 10, no. 5, p. 82, May 2022, doi: 10.3390/LUBRICANTS10050082.
- [181] A. Senatore, G. Risitano, L. Scappaticci, and D. D’andrea, “Investigation of the Tribological Properties of Different Textured Lead Bronze Coatings under Severe Load Conditions,” *Lubr. 2021, Vol. 9, Page 34*, vol. 9, no. 4, p. 34, Mar. 2021, doi: 10.3390/LUBRICANTS9040034.
- [182] D. D’Andrea, A. Pistone, G. Risitano, D. Santonocito, L. Scappaticci, and F. Alberti, “Tribological characterization of a hip prosthesis in Si<sub>3</sub>N<sub>4</sub>-TiN ceramic composite made with Electrical Discharge Machining (EDM),” *Procedia Struct. Integr.*, vol. 33, no. C, pp. 469–481, Jan. 2021, doi: 10.1016/J.PROSTR.2021.10.054.
- [183] D. A. Winter, “Biomechanics and Motor Control of Human Movement: Fourth Edition,” *Biomech. Mot. Control Hum. Mov. Fourth Ed.*, pp. 1–370, Sep. 2009, doi: 10.1002/9780470549148.
- [184] M. W. Whittle, “Gait Analysis,” *Gait Anal.*, 2007, doi: 10.1016/B978-0-7506-8883-3.X5001-6.
- [185] V. Ramakrishna, D. Munoz, M. Hebert, J. Andrew Bagnell, and Y. Sheikh, “Pose machines: Articulated pose estimation via inference machines,” *Lect. Notes Comput. Sci. (including Subser. Lect. Notes Artif. Intell. Lect. Notes Bioinformatics)*, vol. 8690 LNCS, no. PART 2, pp. 33–47, 2014, doi: 10.1007/978-3-319-10605-2\_3/COVER.
- [186] A. Bulat and G. Tzimiropoulos, “Human pose estimation via Convolutional Part Heatmap Regression,” *Lect. Notes Comput. Sci. (including Subser. Lect. Notes Artif.*

## References

- Intell. Lect. Notes Bioinformatics*), vol. 9911 LNCS, pp. 717–732, Sep. 2016, doi: 10.1007/978-3-319-46478-7\_44.
- [187] D. Ramanan, D. A. Forsyth, and A. Zisserman, “Strike a pose: Tracking people by finding stylized poses,” *Proc. - 2005 IEEE Comput. Soc. Conf. Comput. Vis. Pattern Recognition, CVPR 2005*, vol. I, pp. 271–278, 2005, doi: 10.1109/CVPR.2005.335.
- [188] S. Johnson and M. Everingham, “Clustered pose and nonlinear appearance models for human pose estimation,” *Br. Mach. Vis. Conf. BMVC 2010 - Proc.*, 2010, doi: 10.5244/C.24.12.
- [189] Y. Yang and D. Ramanan, “Articulated human detection with flexible mixtures of parts,” *IEEE Trans. Pattern Anal. Mach. Intell.*, vol. 35, no. 12, pp. 2878–2890, 2013, doi: 10.1109/TPAMI.2012.261.
- [190] M. Andriluka, S. Roth, and B. Schiele, “Pictorial structures revisited: People detection and articulated pose estimation,” pp. 1014–1021, Mar. 2010, doi: 10.1109/CVPR.2009.5206754.
- [191] M. Andriluka, S. Roth, and B. Schiele, “Monocular 3D pose estimation and tracking by detection,” *Proc. IEEE Comput. Soc. Conf. Comput. Vis. Pattern Recognit.*, pp. 623–630, 2010, doi: 10.1109/CVPR.2010.5540156.
- [192] P. F. Felzenszwalb and D. P. Huttenlocher, “Pictorial Structures for Object Recognition,” *Int. J. Comput. Vis. 2005 611*, vol. 61, no. 1, pp. 55–79, Jan. 2005, doi: 10.1023/B:VISI.0000042934.15159.49.
- [193] S.-E. Wei, V. Ramakrishna, T. Kanade, and Y. Sheikh, “Convolutional Pose Machines.” pp. 4724–4732, 2016.
- [194] T. Simon, H. Joo, I. Matthews, and Y. Sheikh, “Hand Keypoint Detection in Single Images Using Multiview Bootstrapping.” pp. 1145–1153, 2017.
- [195] T. Pfister, J. Charles, and A. Zisserman, “Flowing ConvNets for Human Pose Estimation in Videos,” Jun. 2015, Accessed: Sep. 05, 2022. [Online]. Available: <http://arxiv.org/abs/1506.02897>.
- [196] A. Toshev and C. Szegedy, “DeepPose: Human Pose Estimation via Deep Neural

## References

- Networks,” *Proc. IEEE Comput. Soc. Conf. Comput. Vis. Pattern Recognit.*, pp. 1653–1660, Dec. 2013, doi: 10.1109/cvpr.2014.214.
- [197] X. Chen and A. L. Yuille, “Articulated Pose Estimation by a Graphical Model with Image Dependent Pairwise Relations,” *Adv. Neural Inf. Process. Syst.*, vol. 27, 2014.
- [198] J. Tompson, A. Jain, Y. LeCun, and C. Bregler, “Joint Training of a Convolutional Network and a Graphical Model for Human Pose Estimation,” *Adv. Neural Inf. Process. Syst.*, vol. 2, no. January, pp. 1799–1807, Jun. 2014, doi: 10.48550/arxiv.1406.2984.
- [199] J. Tompson, R. Goroshin, A. Jain, Y. LeCun, and C. Bregler, “Efficient Object Localization Using Convolutional Networks,” *Proc. IEEE Comput. Soc. Conf. Comput. Vis. Pattern Recognit.*, vol. 07-12-June-2015, pp. 648–656, Nov. 2014, doi: 10.48550/arxiv.1411.4280.
- [200] W. Ouyang, X. Chu, and X. Wang, “Multi-source deep learning for human pose estimation,” *Proc. IEEE Comput. Soc. Conf. Comput. Vis. Pattern Recognit.*, pp. 2337–2344, Sep. 2014, doi: 10.1109/CVPR.2014.299.
- [201] A. Newell, K. Yang, and J. Deng, “Stacked Hourglass Networks for Human Pose Estimation,” *Lect. Notes Comput. Sci. (including Subser. Lect. Notes Artif. Intell. Lect. Notes Bioinformatics)*, vol. 9912 LNCS, pp. 483–499, Mar. 2016, doi: 10.48550/arxiv.1603.06937.
- [202] E. Insafutdinov, L. Pishchulin, B. Andres, M. Andriluka, and B. Schiele, “DeeperCut: A Deeper, Stronger, and Faster Multi-Person Pose Estimation Model,” *Lect. Notes Comput. Sci. (including Subser. Lect. Notes Artif. Intell. Lect. Notes Bioinformatics)*, vol. 9910 LNCS, pp. 34–50, May 2016, doi: 10.48550/arxiv.1605.03170.
- [203] L. Pishchulin *et al.*, “DeepCut: Joint Subset Partition and Labeling for Multi Person Pose Estimation.” pp. 4929–4937, 2016, Accessed: Sep. 05, 2022. [Online]. Available: <http://pose.mpi-inf.mpg.de>.
- [204] Z. Cao, G. Hidalgo, T. Simon, S. E. Wei, and Y. Sheikh, “OpenPose: Realtime Multi-Person 2D Pose Estimation using Part Affinity Fields,” *IEEE Trans. Pattern Anal. Mach. Intell.*, vol. 43, no. 1, pp. 172–186, Dec. 2018, doi: 10.48550/arxiv.1812.08008.

## References

- [205] Z. Cao, T. Simon, S.-E. Wei, and Y. Sheikh, “Realtime Multi-Person 2D Pose Estimation Using Part Affinity Fields.” pp. 7291–7299, 2017, Accessed: Sep. 04, 2022. [Online]. Available: <https://youtu.be/pW6nZXeWlGM>.
- [206] T. Simon, H. Joo, I. Matthews, and Y. Sheikh, “Hand Keypoint Detection in Single Images using Multiview Bootstrapping.”
- [207] G. H. Martinez *et al.*, “Single-Network Whole-Body Pose Estimation,” *Proc. IEEE Int. Conf. Comput. Vis.*, vol. 2019-October, pp. 6981–6990, Sep. 2019, doi: 10.48550/arxiv.1909.13423.
- [208] D. Pagnon, M. Domalain, and L. Reveret, “Pose2Sim: An End-to-End Workflow for 3D Markerless Sports Kinematics—Part 1: Robustness,” *Sensors 2021, Vol. 21, Page 6530*, vol. 21, no. 19, p. 6530, Sep. 2021, doi: 10.3390/S21196530.
- [209] A. Viswakumar, V. Rajagopalan, T. Ray, and C. Parimi, “Human Gait Analysis Using OpenPose,” *undefined*, vol. 2019-November, pp. 310–314, Nov. 2019, doi: 10.1109/ICIIP47207.2019.8985781.
- [210] D. Milone, G. Risitano, A. Pistone, D. Crisafulli, and F. Alberti, “A New Approach for the Tribological and Mechanical Characterization of a Hip Prosthesis Trough a Numerical Model Based on Artificial Intelligence Algorithms and Humanoid Multibody Model,” *Lubr. 2022, Vol. 10, Page 160*, vol. 10, no. 7, p. 160, Jul. 2022, doi: 10.3390/LUBRICANTS10070160.
- [211] B. J. C. Bastiaansen *et al.*, “An inertial measurement unit based method to estimate hip and knee joint kinematics in team sport athletes on the field,” *J. Vis. Exp.*, vol. 2020, no. 159, pp. 1–8, May 2020, doi: 10.3791/60857.
- [212] J. Shi, N. Curtis, L. C. Fitton, P. O’Higgins, and M. J. Fagan, “Developing a musculoskeletal model of the primate skull: Predicting muscle activations, bite force, and joint reaction forces using multibody dynamics analysis and advanced optimisation methods,” *J. Theor. Biol.*, vol. 310, pp. 21–30, Oct. 2012, doi: 10.1016/J.JTBI.2012.06.006.
- [213] A. Moskaljuk, P. Vee, S. Lee, G. Dimitroulis, D. C. Ackland, and C. Hart, “Ackland etal 2015 TMJ Prosthesis Loading After Temporomandibular Joint Replacement Surgery: A

## References

- Musculoskeletal Modeling Study,” 2015, doi: 10.1115/1.4029503.
- [214] F. Gröning *et al.*, “The importance of accurate muscle modelling for biomechanical analyses: a case study with a lizard skull,” *J. R. Soc. Interface*, vol. 10, no. 84, Jul. 2013, doi: 10.1098/RSIF.2013.0216.
- [215] G. E. J. Langenbach and A. G. Hannam, “The role of passive muscle tensions in a three-dimensional dynamic model of the human jaw,” *Arch. Oral Biol.*, vol. 44, no. 7, pp. 557–573, Jul. 1999, doi: 10.1016/S0003-9969(99)00034-5.
- [216] S. N. Young, W. R. VanWye, and H. W. Wallmann, “Sport simulation as a form of implicit motor training in a geriatric athlete after stroke: a case report,” <https://doi.org/10.1080/09593985.2018.1488322>, vol. 36, no. 4, pp. 524–532, Apr. 2018, doi: 10.1080/09593985.2018.1488322.
- [217] P. W. CAMERON, N. C. SOLTERO, and J. BYERS, “Effects of a 60 Minute on Ice Game Simulation on the Balance Error Scoring System,” *Int. J. Exerc. Sci.*, vol. 11, no. 6, p. 462, 2018, Accessed: Jun. 09, 2022. [Online]. Available: </pmc/articles/PMC5841677/>.
- [218] D. H. Gates, L. S. Walters, J. Cowley, J. M. Wilken, and L. Resnik, “Range of Motion Requirements for Upper-Limb Activities of Daily Living,” *Am. J. Occup. Ther.*, vol. 70, no. 1, p. 7001350010p1, Jan. 2016, doi: 10.5014/AJOT.2016.015487.
- [219] U. C. Ugbolue *et al.*, “Joint Angle, Range of Motion, Force, and Moment Assessment: Responses of the Lower Limb to Ankle Plantarflexion and Dorsiflexion,” *Appl. Bionics Biomech.*, vol. 2021, 2021, doi: 10.1155/2021/1232468.
- [220] K. Moromizato, R. Kimura, H. Fukase, K. Yamaguchi, and H. Ishida, “Whole-body patterns of the range of joint motion in young adults: Masculine type and feminine type,” *J. Physiol. Anthropol.*, vol. 35, no. 1, pp. 1–12, Jan. 2016, doi: 10.1186/S40101-016-0112-8/FIGURES/3.
- [221] G. Legnani and G. Palmieri, “Fondamenti di Meccanica e Biomeccanica del Movimento,” 2016, Accessed: Sep. 06, 2022. [Online]. Available: <https://www.goodbook.it/scheda-libro/giovanni-legnani-giacomo-palmieri/fondamenti-di-meccanica-e-biomeccanica-del-movimento-9788825174076-1131518.html>.

## References

- [222] G. Averta, C. Della Santina, E. Battaglia, F. Felici, M. Bianchi, and A. Bicchi, “Unveiling the principal modes of human upper limb movements through functional analysis,” *Front. Robot. AI*, vol. 4, no. AUG, p. 37, Aug. 2017, doi: 10.3389/FROBT.2017.00037/XML/NLM.
- [223] G. Wu *et al.*, “ISB recommendation on definitions of joint coordinate systems of various joints for the reporting of human joint motion--Part II: shoulder, elbow, wrist and hand,” *J. Biomech.*, vol. 38, no. 5, pp. 981–992, May 2005, doi: 10.1016/J.JBIOMECH.2004.05.042.
- [224] G. Wu *et al.*, “ISB recommendation on definitions of joint coordinate system of various joints for the reporting of human joint motion - Part I: Ankle, hip, and spine,” *J. Biomech.*, vol. 35, no. 4, pp. 543–548, 2002, doi: 10.1016/S0021-9290(01)00222-6.
- [225] H. Cheng, L. Obergefell, and A. Rizer, “Generator of Body Data (GEBOD) , Manual.” Mar. 01, 1994, Accessed: Sep. 07, 2022. [Online]. Available: <https://apps.dtic.mil/sti/citations/ADA289721>.
- [226] “Anthropometric Database - Army Public Health Center.” <https://phc.amedd.army.mil/topics/workplacehealth/ergo/Pages/Anthropometric-Database.aspx> (accessed Sep. 07, 2022).
- [227] R. D’Agostino and E. S. Pearson, “Tests for departure from normality. Empirical results for the distributions of  $b_2$  and  $\sqrt{b_1}$ ,” *Biometrika*, vol. 60, no. 3, pp. 613–622, 1973, doi: 10.2307/2335012.
- [228] R. B. D’Agostino, “An Omnibus Test of Normality for Moderate and Large Size Samples,” *Biometrika*, vol. 58, no. 2, p. 341, Aug. 1971, doi: 10.2307/2334522.
- [229] W. H. Ho, T. Y. Shiang, C. C. Lee, and S. Y. Cheng, “Body segment parameters of young Chinese men determined with magnetic resonance imaging,” *Med. Sci. Sports Exerc.*, vol. 45, no. 9, pp. 1759–1766, Sep. 2013, doi: 10.1249/MSS.0B013E3182923B2A.
- [230] R. Dumas and J. Wojtusich, “Estimation of the body segment inertial parameters for the rigid body biomechanical models used in motion analysis,” *Handb. Hum. Motion*, vol. 1–3, pp. 47–77, Apr. 2018, doi: 10.1007/978-3-319-14418-4\_147/COVER.

## References

- [231] D. Milone, G. Risitano, A. Pistone, D. Crisafulli, and F. Alberti, “A New Approach for the Tribological and Mechanical Characterization of a Hip Prosthesis Through a Numerical Model Based on Artificial Intelligence Algorithms and Humanoid Multibody Model,” *Lubr. 2022, Vol. 10, Page 160*, vol. 10, no. 7, p. 160, Jul. 2022, doi: 10.3390/LUBRICANTS10070160.
- [232] J. Walczak, F. Shahgaldi, and F. Heatley, “In vivo corrosion of 316L stainless-steel hip implants: morphology and elemental compositions of corrosion products,” *Biomaterials*, vol. 19, no. 1–3, pp. 229–237, Jan. 1998, doi: 10.1016/S0142-9612(97)00208-1.
- [233] F. Cucinotta, A. D’Aveni, E. Guglielmino, A. Risitano, G. Risitano, and D. Santonocito, “Thermal Emission analysis to predict damage in specimens of High Strength Concrete,” *Frat. ed Integrità Strutt.*, vol. 15, no. 55, pp. 258–270, 2021, doi: 10.3221/IGF-ESIS.55.19.
- [234] A. D. Melvin, A. C. Lucia, and G. P. Solomos, “The thermal response to deformation to fracture of a carbon/epoxy composite laminate,” *Compos. Sci. Technol.*, vol. 46, no. 4, pp. 345–351, Jan. 1993, doi: 10.1016/0266-3538(93)90180-O.
- [235] P. Foti, D. Santonocito, P. Ferro, G. Risitano, and F. Berto, “Determination of Fatigue Limit by Static Thermographic Method and Classic Thermographic Method on Notched Specimens,” *Procedia Struct. Integr.*, vol. 26, pp. 166–174, Jan. 2020, doi: 10.1016/J.PROSTR.2020.06.020.
- [236] S. Arabnejad, R. Burnett Johnston, J. A. Pura, B. Singh, M. Tanzer, and D. Pasini, “High-strength porous biomaterials for bone replacement: A strategy to assess the interplay between cell morphology, mechanical properties, bone ingrowth and manufacturing constraints,” *Acta Biomater.*, vol. 30, pp. 345–356, Jan. 2016, doi: 10.1016/J.ACTBIO.2015.10.048.
- [237] P. F. Egan, V. C. Gonella, M. Engensperger, S. J. Ferguson, and K. Shea, “Computationally designed lattices with tuned properties for tissue engineering using 3D printing,” *PLoS One*, vol. 12, no. 8, p. e0182902, Aug. 2017, doi: 10.1371/JOURNAL.PONE.0182902.
- [238] P. F. Egan, V. C. Gonella, M. Engensperger, S. J. Ferguson, and K. Shea,

## *References*

“Computationally designed lattices with tuned properties for tissue engineering using 3D printing,” *PLoS One*, vol. 12, no. 8, p. e0182902, Aug. 2017, doi: 10.1371/JOURNAL.PONE.0182902.

---

## **LIST OF PUBLICATIONS**

[1] Cervino, G., Romeo, U., Lauritano, F., Bramanti, E., Fiorillo, L., D'Amico, C., Milone, D., Laino, L., Campolongo, F., Rapisarda, S., Cicciù, M. (2018). Fem and Von Mises Analysis of OSSTEM ® Dental Implant Structural Components: Evaluation of Different Direction Dynamic Loads, *Open Dent. J.*, , Doi: 10.2174/1874210601812010219.

[2] Cicciù, M., Cervino, G., Milone, D., Risitano, G. (2018). FEM Investigation of the Stress Distribution over Mandibular Bone Due to Screwed Overdenture Positioned on Dental Implants, *Mater.* 2018, Vol. 11, Page 1512, 11(9), pp. 1512, Doi: 10.3390/MA11091512.

[3] Cicciù, M., Cervino, G., Milone, D., Risitano, G. (2019). FEM Analysis of Dental Implant-Abutment Interface Overdenture Components and Parametric Evaluation of Equator® and Locator® Prosthodontics Attachments, *Mater.* 2019, Vol. 12, Page 592, 12(4), pp. 592, Doi: 10.3390/MA12040592.

[4] Cervino, G., Cicciù, M., Fedi, S., Milone, D., Fiorillo, L. (2020). FEM Analysis Applied to OT Bridge Abutment with Seeger Retention System, , Doi: 10.1055/s-0040-1715550.

[5] D'Andrea, D., Risitano, G., Desiderio, E., Quintarelli, A., Milone, D., Alberti, F. (2021). Artificial Neural Network Prediction of the Optimal Setup Parameters of a Seven Degrees of Freedom Mathematical Model of a Race Car: IndyCar Case Study, *Vehicles*, , Doi: 10.3390/vehicles3020019.

[6] Scappaticci, L., Risitano, G., Santonocito, D., D'Andrea, D., Milone, D. (2021). An Approach to the Definition of the Aerodynamic Comfort of Motorcycle Helmets, *Vehicles*, , Doi: 10.3390/vehicles3030033.

*List of publications*

- [7] D'Andrea, D., Milone, D., Nicita, F., Risitano, G., Santonocito, D. (2021). Qualitative and Quantitative Evaluation of Different Types of Orthodontic Brackets and Archwires by Optical Microscopy and X-ray Fluorescence Spectroscopy, *Prosthesis*, 3(4), pp. 342–60, Doi: 10.3390/PROSTHESIS3040031.
- [8] Milone, D., Nicita, F., Cervino, G., Santonocito, D., Risitano, G. (2021). Finite element analysis of OT bridge fixed prosthesis system, *Procedia Struct. Integr.*, 33(C), pp. 734–47, Doi: 10.1016/J.PROSTR.2021.10.081.
- [9] Milone, D., Fiorillo, L., Alberti, F., Cervino, G., Filardi, V., Pistone, A., Cicciù, M., Risitano, G. (2022). Stress distribution and failure analysis comparison between Zirconia and Titanium dental implants, *Procedia Struct. Integr.*, 41, pp. 680–91, Doi: 10.1016/J.PROSTR.2022.05.077.
- [10] Milone, D., Risitano, G., Pistone, A., Crisafulli, D., Alberti, F. (2022). A New Approach for the Tribological and Mechanical Characterization of a Hip Prosthesis Through a Numerical Model Based on Artificial Intelligence Algorithms and Humanoid Multibody Model, *Lubricants*, 10(7), pp. 160, Doi: 10.3390/LUBRICANTS10070160.
- [11] Fiorillo, L., Milone, D., D'Andrea, D., Santonocito, D., Risitano, G., Cervino, G., Cicciù, M. (2022). Finite Element Analysis of Zirconia Dental Implant, *Prosthesis*. 2022, Vol. 4, Pages 490-499, 4(3), pp. 490–9, Doi: 10.3390/PROSTHESIS4030040.